UNCLASSIFIED
SECURITY CLASSIFICATION OF THIS PAGE

REPORT DOCUMENTATION PAGE

1a REPORT SECURITY CLASSIFICATION: UNCLASSIFIED	1b RESTRICTIVE MARKINGS: NONE
2a SECURITY CLASSIFICATION AUTHORITY	3 DISTRIBUTION/AVAILABILITY OF REPORT: APPROVED FOR PUBLIC RELEASE: DISTRIBUTION UNLIMITED
2b DECLASSIFICATION/DOWNGRADING SCHEDULE	
4 PERFORMING ORGANIZATION REPORT NUMBER(S): UILU-ENG-87-4002	5. MONITORING ORGANIZATION REPORT NUMBER(S): AFOSR-TR- 87-0823
6a NAME OF PERFORMING ORGANIZATION: UNIVERSITY of ILLINOIS AT URBANA - CHAMPAIGN	6b. OFFICE SYMBOL (If applicable): UIUC
6c. ADDRESS (City, State, and ZIP Code): Dept. of Mechanical & Industrial Engineering 144 MEB; 1206 West Green Street Urbana, Illinois 61801	7a. NAME OF MONITORING ORGANIZATION: AIR FORCE OFFICE OF SCIENTIFIC RESEARCH
	7b ADDRESS (City, State, and ZIP Code): Bldg 410 Bolling AFB, DC 20332
8a. NAME OF FUNDING/SPONSORING ORGANIZATION AIR FORCE OFFICE OF SCIENTIFIC RESEARCH	8b. OFFICE SYMBOL (If applicable): AFOSR /NA
8c. ADDRESS (City, State, and ZIP Code): AFOSR/NA Bldg 410 Bolling AFB, DC 20332	9. PROCUREMENT INSTRUMENT IDENTIFICATION NUMBER: AFOSR GRANT NO. 83-0041
	10 SOURCE OF FUNDING NUMBERS: PROGRAM ELEMENT NO. 61102F; PROJECT NO. 2308; TASK NO. A1; WORK UNIT ACCESSION NO.

11 TITLE (Include Security Classification)
LASER-SUSTAINED PLASMAS FOR APPLICATION TO ROCKET PROPULSION (U)

12 PERSONAL AUTHOR(S)
J. Mazumder, H. Krier, B.K. McMillin, D.K. Zerkle, X. Chen

13a. TYPE OF REPORT	13b. TIME COVERED	14. DATE OF REPORT (Year, Month, Day)	15. PAGE COUNT
Final Technical Report	FROM 2/1/83 TO 3/15/87	01 April 1987	150

16. SUPPLEMENTARY NOTATION

17 COSATI CODES		
FIELD	GROUP	SUB-GROUP

18 SUBJECT TERMS (Continue on reverse if necessary and identify by block number)
BEAMED ENERGY, PROPULSION; LASER, PLASMA, FORMATION

19 Laser propulsion is the production of high specific impulse rocket thrust using a high-energy laser as a remote power source. Specific impulses in excess of 1000 sec are achievable because propellant temperatures are very high and low molecular weight gases can be used. This report highlights the research status of the fourth year of AFOSR sponsored work for converting the laser energy, and reports the results of ongoing experiments using laser-sustained plasmas as the conversion mechanism. Major new findings from our spectroscopic techniques to diagnose the laser-sustained plasmas are also reported. The results indicate that it is possible to absorb almost all of the laser energy in the plasma, but that more effective ways are required to assure that the thermal energy of the gases flowing around and through the plasma(s) can approach efficiencies exceeding 50 percent.

Fundamental research in the area of extremely high temperature gas mixing by forced convection is called for. Techniques by which the gas can reabsorb the radiation energy from the laser-sustained plasma will have to be developed.

Keywords:

20. DISTRIBUTION/AVAILABILITY OF ABSTRACT: ☒ UNCLASSIFIED/UNLIMITED ☐ SAME AS RPT ☐ DTIC USERS	21. ABSTRACT SECURITY CLASSIFICATION: UNCLASSIFIED
22a. NAME OF RESPONSIBLE INDIVIDUAL: Dr. Julian M. Tishkoff	22b. TELEPHONE (Include Area Code): (202) 767-4935 / 22c. OFFICE SYMBOL: AFOSR/NA

DD FORM 1473, 84 MAR — 83 APR edition may be used until exhausted. All other editions are obsolete.

SECURITY CLASSIFICATION OF THIS PAGE
UNCLASSIFIED

AFOSR-TR- 87-0823

ABSTRACT

Laser propulsion is the production of high specific impulse rocket thrust using a high-energy laser as a remote power source. Specific impulses in excess of 1000 sec are achievable because propellant temperatures are very high and low molecular weight gases can be used. This report highlights the research status of the fourth year of AFOSR sponsored work for converting the laser energy, and reports the results of ongoing experiments using laser-sustained plasmas as the conversion mechanism. Major new findings from our spectroscopic techniques to diagnose the laser-sustained plasmas are also reported. The results indicate that it is possible to absorb almost all of the laser energy in the plasma, but that more effective ways are required to assure that the thermal energy of the gases flowing around and through the plasma(s) can approach efficiencies exceeding 50 percent.

Fundamental research in the area of extremely high temperature gas mixing by forced convection is called for. Techniques by which the gas can reabsorb the radiation energy from the laser-sustained plasma will have to be developed.

TABLE OF CONTENTS

SECTION 1: INTRODUCTION

1.1 Research Objectives and Background

Recent advances in the fields of high power lasers and laser optics made possible a completely new form of rocket propulsion--laser-assisted rocket propulsion. Simply stated, laser propulsion is the production of high specific impulse rocket thrust using a remote high-energy laser. The laser heats a propellant gas, which is then expelled through a conventional rocket nozzle to produce thrust. A generalized sketch of such a system is shown in Figure 1. Here, a space-based laser beam is collected and focused inside an absorption chamber, where the laser energy is converted into the thermal energy of a propellant gas. Reference [1] is a useful review article which discusses the overall challenges to achieve beamed energy proprulsion.

Laser propulsion has the potential of filling an important performance gap between existing propulsion systems. In Figure 2, generalized values of thrust versus specific impulse (Isp) are presented for chemical and electric propulsion. Chemical systems are cpable of extremely high thrust but are limited to Isp values under 500 seconds. Electric propulsion systems, by contrast, achieve extremely high specific impulse values, but tend to be limited to very low thrust levels, and are usually heavy due to the onboard power source.

Laser propulsion is potentially capable of producing moderate levels of thrust at relatively high specific impulse. This can best be explained by examining the equation for Isp in a steady-flow rocket nozzle:

$$I_{sp} = (1/g)\left[(2\gamma/\gamma-1)\frac{\bar{R}}{MW} T_c \phi\right]^{1/2} \qquad (1)$$

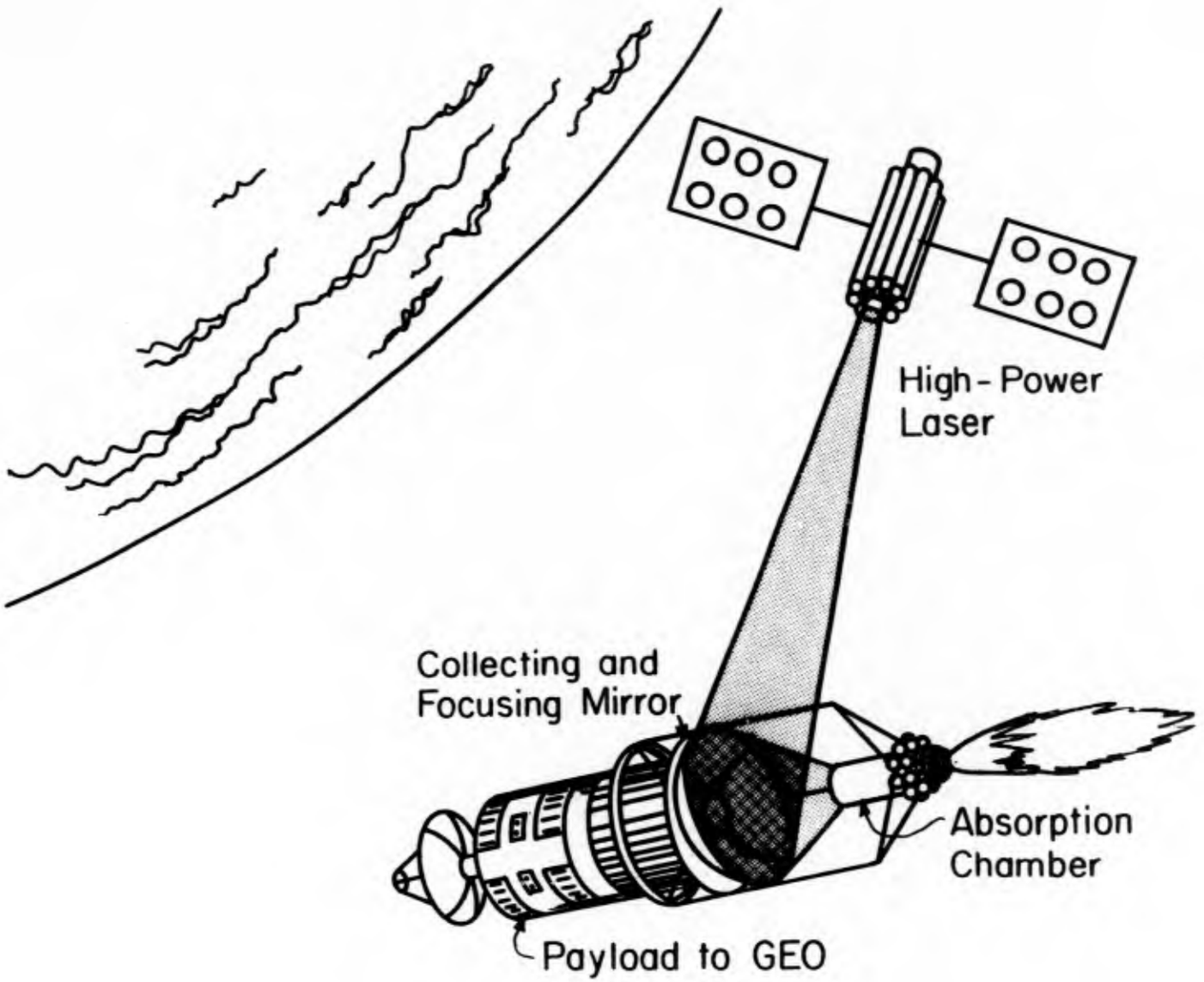

Figure 1: Schematic operation of a laser propulsion system used for orbit-raising. The beam of a high power laser is collected, focused, and converted into thermal propellant energy.

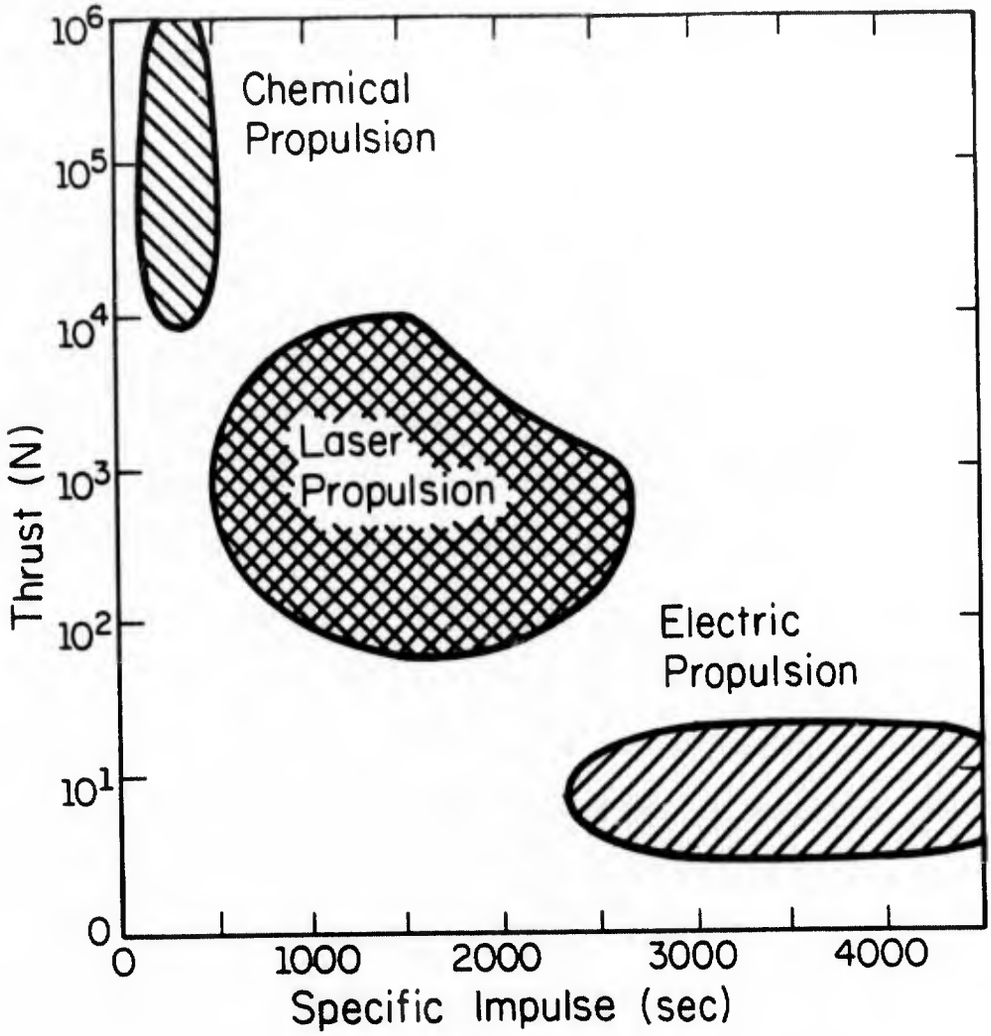

Figure 2: Laser propulsion promises to fill the performance gap between high-thrust low-Isp chemical propulsion and low-thrust high-Isp electric propulsion.

where $\phi \equiv 1 - (P_e/P_c)^{\gamma-1/\gamma}$, P_e is nozzle exit pressure, γ the ratio of specific heats, $\bar{R}$ the universal gas constant, MW the propellant molecular weight, T_c the chamber temperature, and ϕ a pressure ratio term that depends on the deisgn of the nozzle.

In chemical systems, molecular weight is fixed by the choice of reactive propellants, and propellant temperature is limited to the combustion temperature of the reaction, typically below 3500 K. Laser propulsion, by contrast, would use low molecular weight propellants, and the energy added to the propellant is limited only by the available laser power. This makes it possible to produce exhaust gas temperatures above 5000 K. When hydrogen is used as the propellant, such high temperatures permit specific impulse values up to 2000 seconds [2]. Finally, because the power source is remote, a laser propulsion system should be lighter than electric systems.

Of course, the production of significant thrust (> 1000 N) requires a sizable laser power input, typically a minimum of about 10 MW. In addition, as illustrated in Figure 3, there is a direct trade-off between thrust and specific impulse at a given laser power [1]. This is because thrust is directly proportional to the mass flow rate, whereas specific impulse is an inverse function. Thus, as flow rate is increased, the thrust increases; however, the propellant is exposed to the laser energy for a shorter time, reducing bulk exhaust temperatures and therefore specific impulse.

The ultimate goal of ongoing laser propulsion research is the development of a moderate-thrust (1-10 kN) engine capable of specific impulses in excess of 1000 seconds. The engine would be best suited for use as an orbital transfer vehicle in low earth orbit, where high thrust is unnecessary and Isp is at a premium.

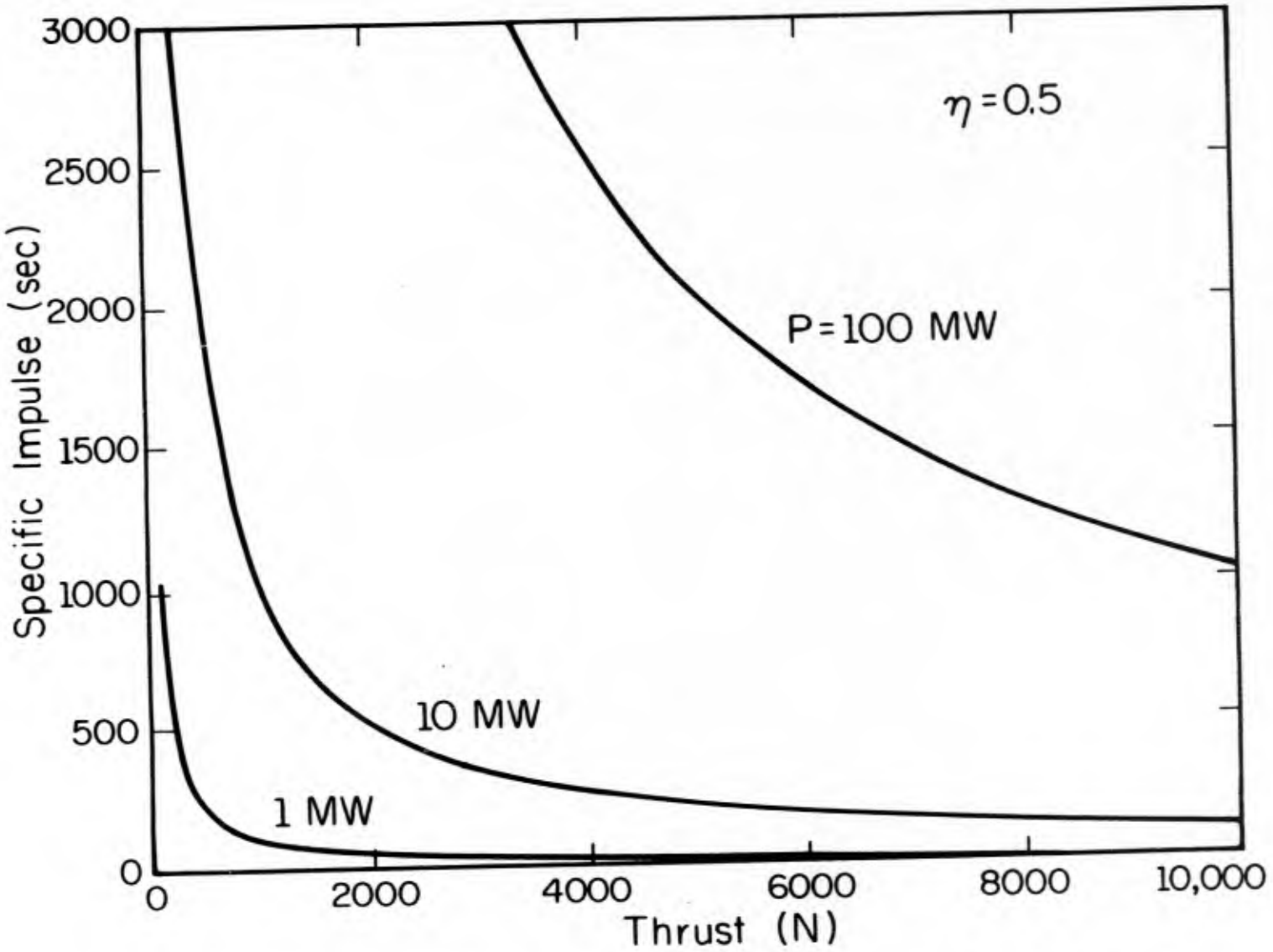

Figure 3: Specific impulse versus thrust for a laser propulsion system at 50% efficiency, based on the relation $F = (2\eta P)/(Isp\ g)$ [2]. Useful thrust levels at 1000 sec will require 10-100 MW of laser power.

The key problem is how to maximize the thermal conversion efficiency, defined as the ratio of the laser energy retained by the exhaust gas to the energy of the incoming laser beam. As was seen in Figure 3, high efficiency is needed to minimize the laser power required. At the listed efficiency of 50%, a thruster of 10 kN at 1000 sec Isp needs a laser input power of 100 MW. It is currently thought that the minimum efficiency needed for laser propulsion to be feasible is about 50%, and that efficiencies of 90% could make the concept practical. The following sections report the results of our AFOSR sponsored studies on laser sustained plasmas and their conversion efficiency.

1.2 Previously Reported Work

Work reported in previous Technical Annual Reports prepared for AFOSR, as well as other publications [3,4,5,] have clearly demonstrated that for our relatively high current laser powers (high, by early 1980 standards) we can expect to absorb 80% to 100% of the input laser energy by means of a stationary laser sustained plasma. Plasma temperatures have been measured to approach 20,000 K. Figure 4 is a tyical result of the fraction of measured absorbed laser power versus laser power for three low f/number optical arrangements. The average flux at the focus ranges from 10^5 to 10^6 Watts/cm^2 [5,6].

References [4] and [5] provide the details of the theoretical model we have developed in order to interpret our experimental findings and to predict new operating conditions which would maximize the thermal efficiency, as a function of laser power, gas velocity, and beam configuration. In this report we do <u>not</u> repeat the description of the model nor the solution procedure.

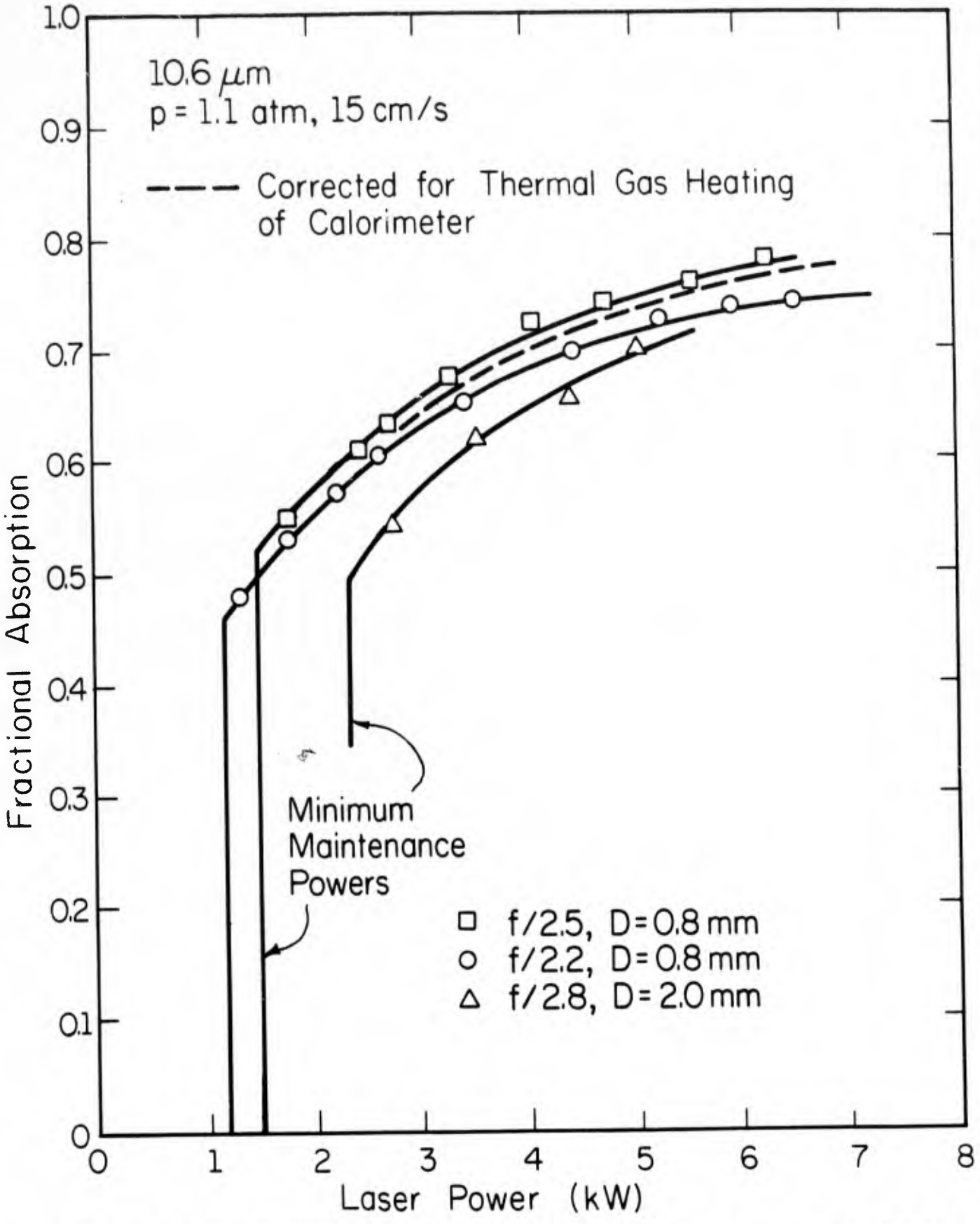

Figure 4: Global absorption variation with f/# and spot size. Higher f/#'s produce higher absorption with steeper slopes; larger spot size reduces absorption at low power and raises the minimum maintenance power. The dashed curve above the f/2.2 data is a correction factor for hot gas that stagnates inside the calorimeter.

The model reasonably describes major features of our experiments [4,5]. Figure 5 compares the predicted global absorption variation with laser power and that measured. The agreement is excellent. More importantly, the model can also describe the fraction of energy finally absorbed in the gases flowing through the laser-sustained plasma. Figures 6 and 7 present those predictions for mass average argon velocities of 15 cm/sec and 51 cm/sec, respectively. Efficiencies ranging from 20% to 32% (in the range of $2 < \text{Power} < 10$ kW) are predicted.

The model has indicated the gas flow velocity must be optimized for a given laser power. For example, Figure 8 shows the predicted variations at $P = 5$ kW and predicts the plasma will blowout at a velocity of 310 cm/sec. To allow greater average velocities, as will be necessary in laser powered thrusters, higher laser powers will be required (see Figure 9).

The model has also indicated the thermal efficiency can be significantly increased with higher f/number optics. For example, results shown in Figure 10 indicate that a 5 kW plasma is stable at f/numbers as high as f/16 and the thermal efficiency approaches 80% for argon at a velocity of 250 cm/s.

Experimental work which has been previously reported has included thermal efficiencies based upon measured downstream radial temperature profiles as well as spectroscopic measurements of the plasma core temperatures and absorption. Most of the experiment work previously reported was preliminary in nature and was subject to errors. That work has been repeated and extended to new operating conditions as discussed in the next section.

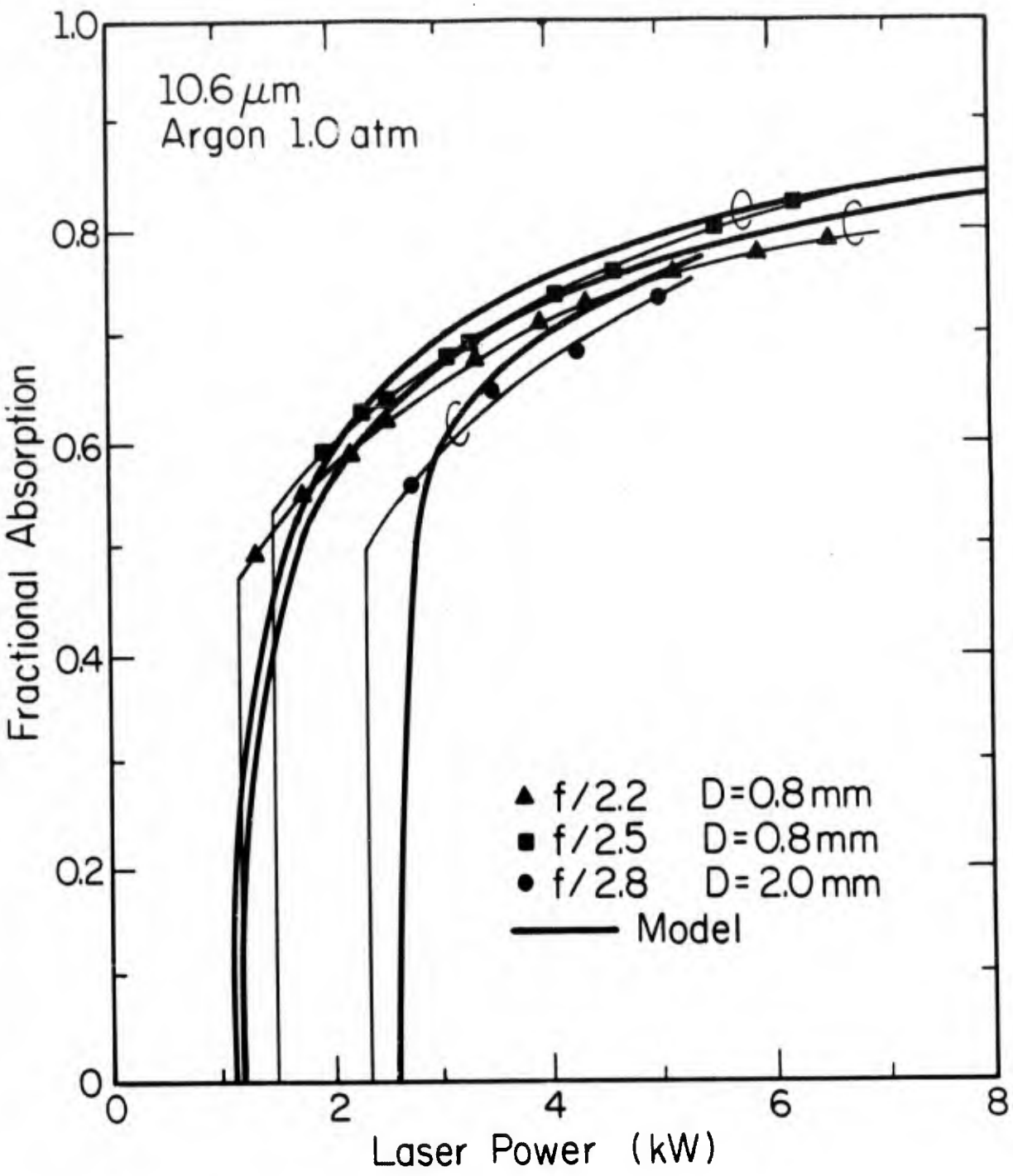

Figure 5: Global absorption predictions for three different optical geometries, compared to the corresponding experimental data.

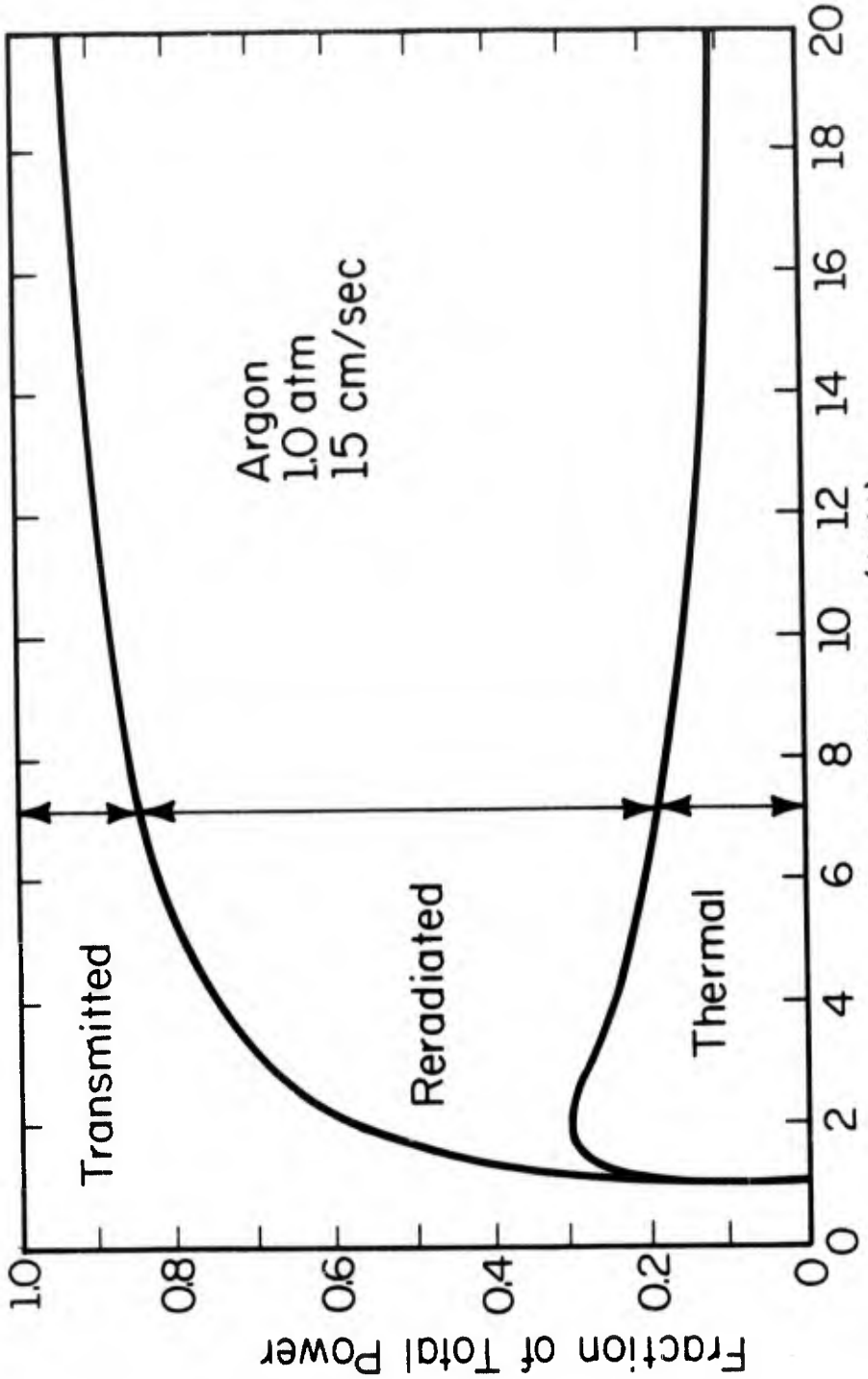

Figure 6: Fractions of the incident laser power that are transmitted through the plasma (upper area), reradiated by the plasma and lost to the chamber walls (middle area), and retained by the gas as thermal energy (lower portion). Radiation loss becomes the dominant process at high laser powers. Flow rate is 15 cm/sec.

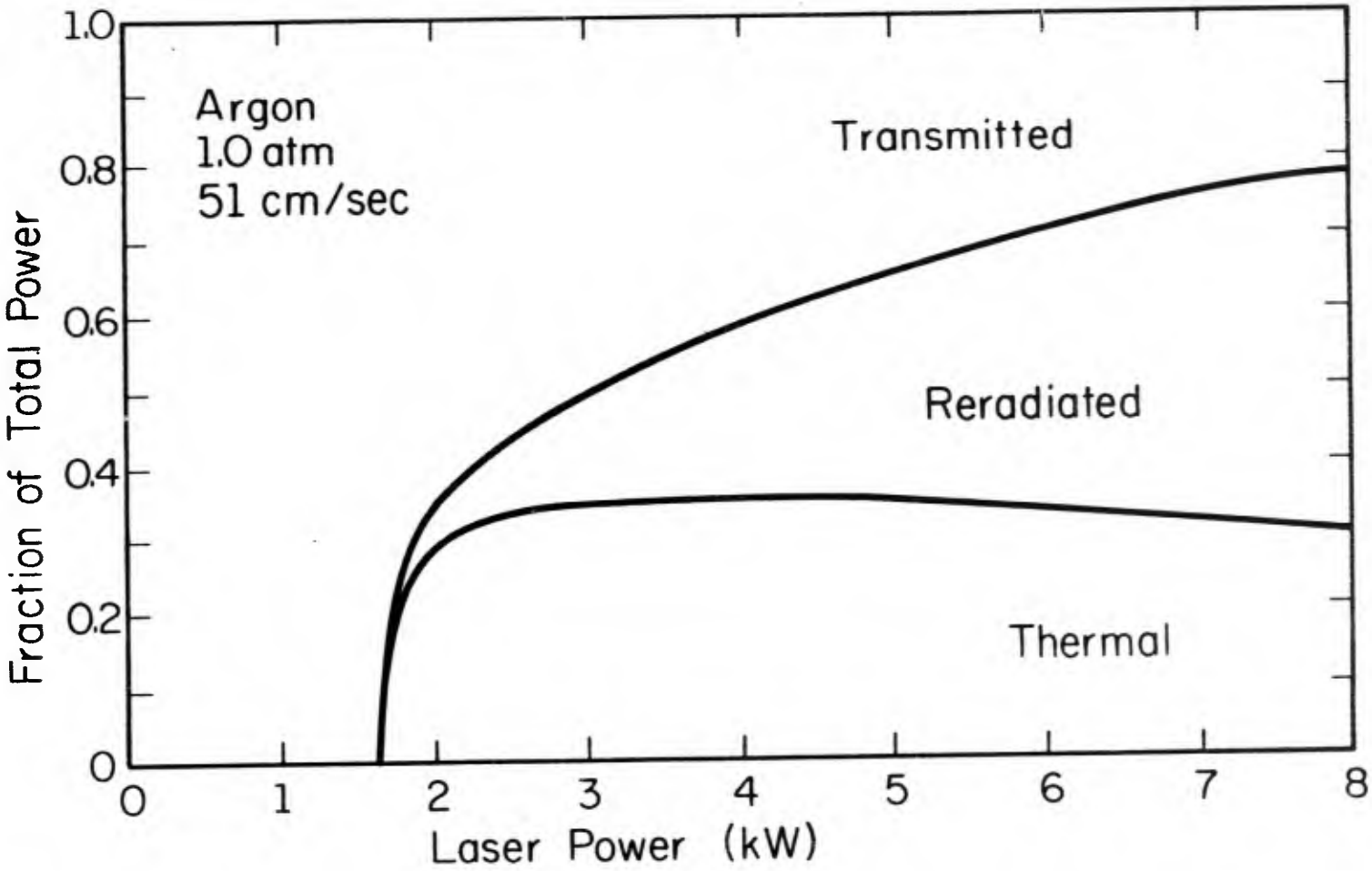

Figure 7: Fractional transmittance, reradiation, and thermal energy as functions of laser power. Flow rate is 51 cm/sec. Note that the predicted efficiency has increased substantially.

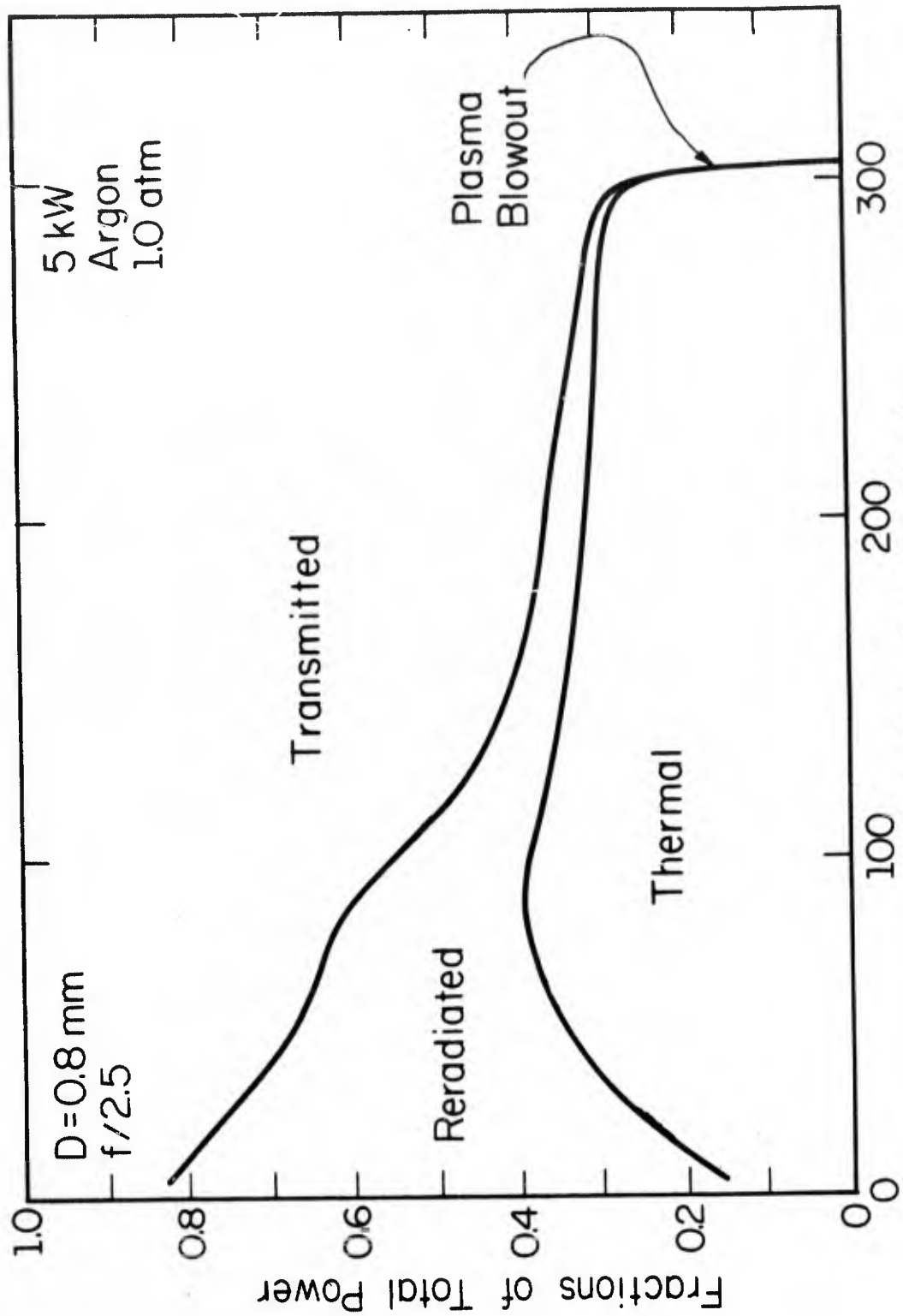

Figure 8: Fractional transmittance, reradiation, and thermal energy as functions of flow rate at 5 kW. The predicted efficiency rises from 22 percent to a peak of 39.4 percent.

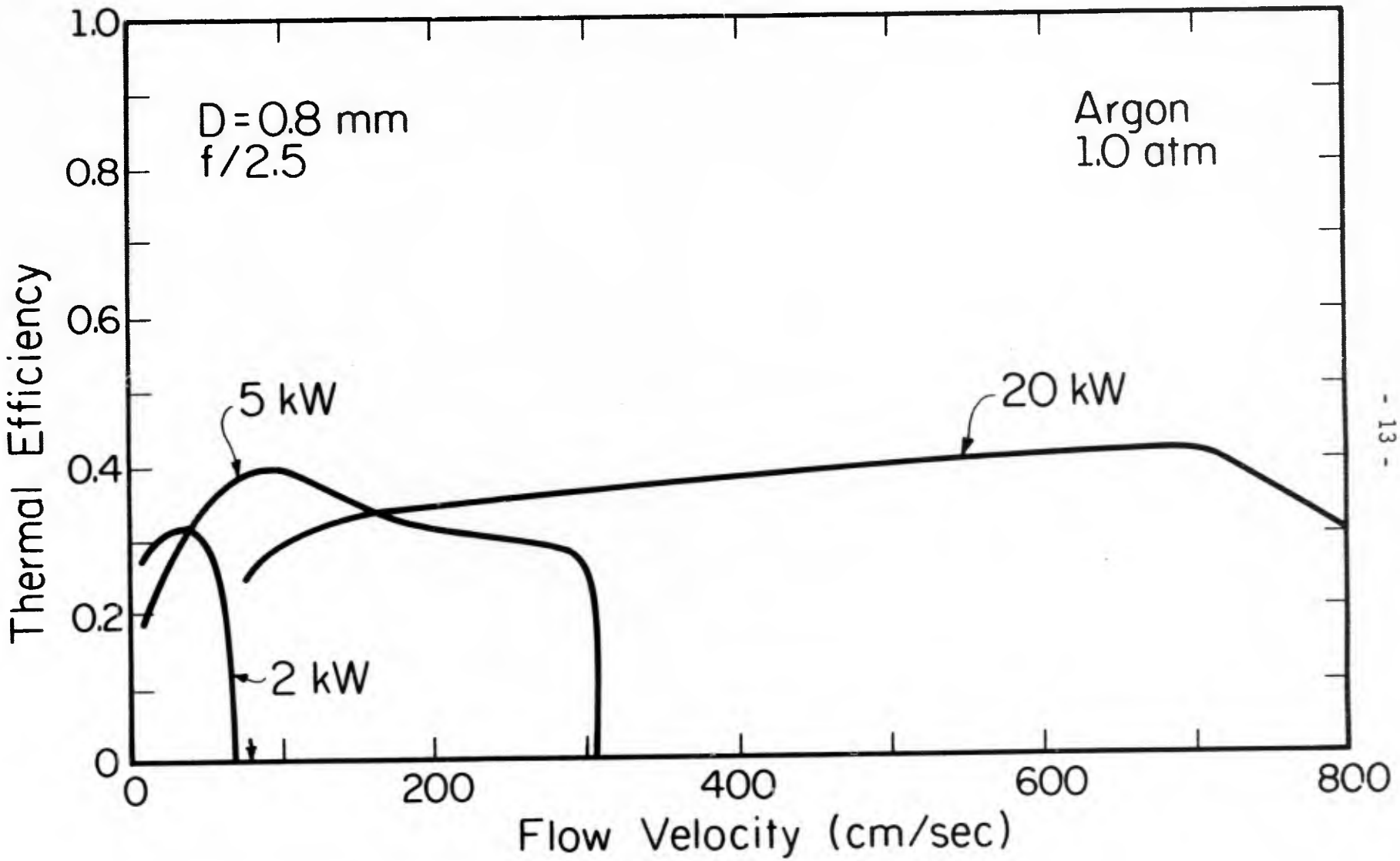

Figure 9: Predicted thermal efficiency versus flow rate at laser powers of 2, 5, and 20 kW. At higher powers, both the blowout velocity and the flow rate for maximum efficiency increases. The peak in the efficiency also rises, from 31.3 to 39.4 to 41.8 percent. The arrow indicates the measured blowout velocity for a 2 kW plasma.

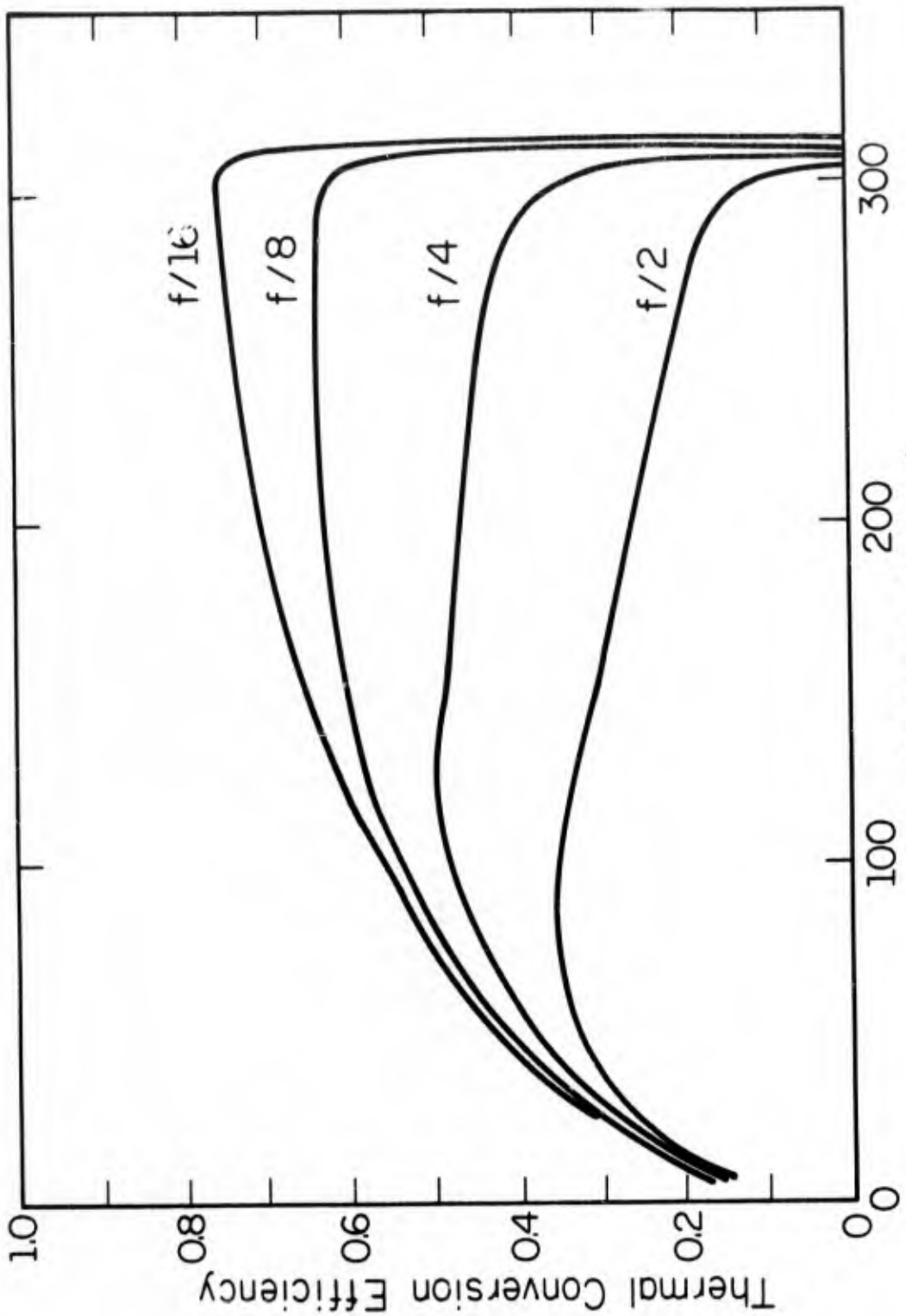

Figure 10: Predicted efficiency versus flow velocity for a range of optical f numbers. Note the dramatic rise from 35 percent at f/2 to nearly 80 percent at f/16. Laser power is 5 kW, and the focus spot diameter is assumed constant at 0.8 mm.

1.3 Work Undertaken in 1986

A large portion of this year's work included an extension of our experimental studies to new operating conditions. To this end, a new gas flow system was installed which allows chamber gas velocities of up to 500 cm/s. In addition, a split flat mirror was installed in the optics system to permit the study of twin plasmas sustained adjacent to one another within the absorption chamber. A further modification of the optics system entails the use of a NaCl lens as the beam focusing device. The lens can be changed easily and permits a wider variation in the f/# of the beam focusing optics.

The new gas flow system will be used to check efficiency variation across a wider range of flow velocities, and to determine the experimental blow-out velocities at input laser powers greater than 5 kW. The original gas flow system was incapable of producing chamber gas velocities above the optimum for laser powers of 5 kW or more. Typically the model [4,5] predicts efficiency increases with velocity up to an optimum value, and then it decreases with further increases in velocity, until the plasma blows out. It is hoped experimental efficiency variation measurements for several laser powers over the whole range of velocities will lead to the development of an empirical correction correlation for the model predictions. This correlation could be used in conjunction with modeling results to predict efficiencies more accurately at laser powers of 100 kW or more.

The impetus for studying multiple plasmas centers around the model's prediction that, for example, a 5 kW plasma is more efficient than a 20 kW plasma at certain flow velocities. This can be seen graphically in Figure 9 at velocities less than ~ 160 cm/s. In addition, Figure 9 shows that a 20 kW plasma matches a 5 kW plasma's efficiency only at a very high gas velocity.

At such high velocities the temperature increase of the gas is reduced considerably, limiting specific impulse. Thus, splitting a 20 kW beam into four 5 kW beams to form four, more efficient plasmas with higher specific impulse may be advantageous. These system characteristics are a result of the variation in efficiency for a given power as velocity increases. This variation is due to the tradeoffs between the respective amounts of energy absorbed and then reradiated by the plasma, at different flow velocities. For example, at certain flow velocities absorption dominates radiation, and at others radiation dominates absorption. A more detailed discussion of the physics involved in these tradeoffs is presented in Section 3.4.

The high f/# optics system will be used to study the effect of varying beam geometry on energy conversion. In general, the plasma becomes longer and more narrow with increasing gas velocity, and as a result, at low f/#'s the geometrical path length for beam absorption is reduced. In this case much of this incident laser energy is needlessly transmitted. The point of using a higher f/# beam is to more closely match the focused beam and plasma shapes, thus increasing the absorption path length, and consequently, the global absorption and the thermal efficiency as well. For example, as shown in Figure 10, the model [4,5] predicts efficiencies of up to ~ 50% for an f/4 beam and up to ~ 65% for an f/8 beam with an input power of 5 kW. With the new lens system, these beam geometries can be employed, and model verification experiments can be conducted.

Another aspect of this year's work was the extension of the spectroscopic studies to the new operating conditions. Mapping of the plasma core temperatures and calculation of absorption are key features of this work. From these data, thermal efficiencies can be calculated and compared to

efficiencies determined independently from thermocouple data and from model predictions. Twin plasma measurements present a problem due to the system's inherent lack of cylindrical symmetry. Consequently, all spectroscopic twin plasma measurements are preliminary in nature.

Also this year we began taking planar laser induced fluorescence (PLIF) diagnostic measurements in a premixed flame. A suitable technique for temperature and velocity diagnostics in the plasma vicinity has been selected, including the appropriate atomic seed. This diagnostic technique will provide temperature mappings of the region downstream of the plasma, and will result in more accurate experimental efficiency measurements.

Meanwhile, extensive efforts to improve the thermocouple measurements and efficiency calculation technique have been made. Developing better radiation shielding of the thermocouples and a more consistent efficiency calculation technique were the focus of this work. With these improvements, efficiency measurements at the new operating conditions have been made with unprecedented accuracy. In addition, an aspirated thermocouple was also designed and built to help reduce error in downstream gas temperature measurements.

SECTION 2: EXPERIMENTAL FACILITY

The facility utilized in this research includes the University's high power CO_2 laser, a beam steering optical system, a plasma initiation and flow chamber (PIFC) equipped with temperature, absorption, pressure and optical diagnostics ports, and a data collection and control system. The facility has been described in a previous report [5] but several improvements have since been incorporated into the facility, including a new gas delivery system, new temperature and pressure diagnostics systems, as well as an improved plasma initiation technique. In addition, the beam steering optics has been revised allowing the beam to be focused at one point or two adjacent points, thus permitting the study of one relatively large or two smaller plasmas with only one laser source. Finally, the data collection computer program has been revised to accomodate the new temperature and pressure diagnostics systems. In the following paragraphs the enhanced experimental facility will be described in detail.

2.1 Laser Facility

The laser facility employed in this research is shown schematically in Figure 11 and includes a laser laboratory, a laser control room, an experiment control room and an outside storage area. The laser and the PIFC are located within the laser laboratory while the gas propellant is stored in pressurized tanks in the outside storage area. No personnel are allowed in the laser laboratory during an experiment due to the danger of stray or reflected laser radiation. As a result, the PIFC diagnostics and controls are operated within the experiment control room, while the laser is operated remotely from within the laser control room.

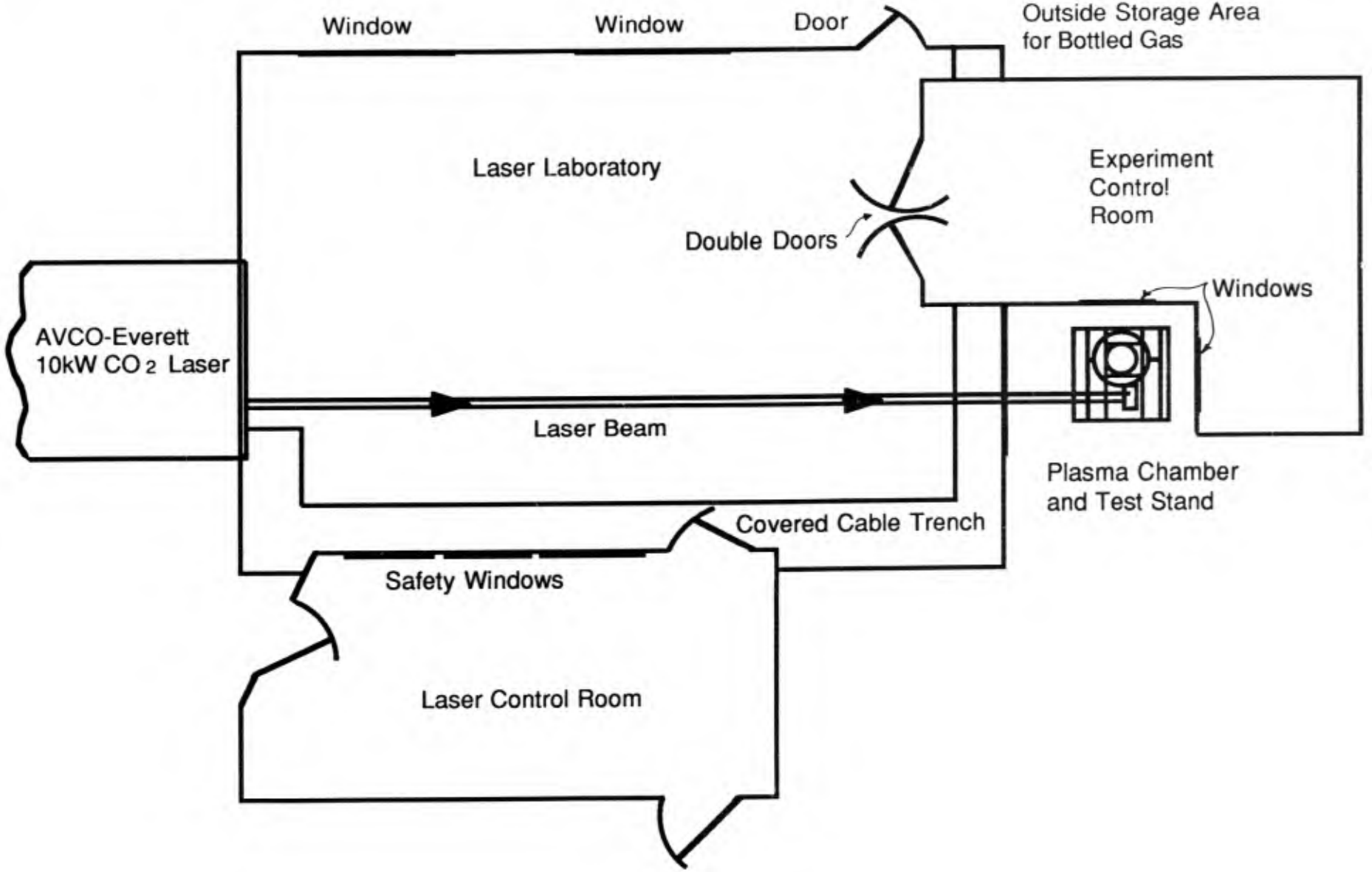

Figure 11: Schematic of the laser facility.

The laser is a continuous wave, variable power, 10 kW AVCO-Everett CO_2 laser. The laser outputs a 2.6 inch outside diameter annular beam with a nearly Gaussian energy distribution across the annulus, at an infrared wavelength of 10.6 μm. The beam is propagated horizontally 1.275 m above the laboratory floor and travels approximately 8 meters before reaching the optics of the PIFC test stand.

2.2 Laser Calibration

To date the laser has been calibrated using a Series 25 Laser Power Probe manufactured by Optical Engineering, Inc. The Probe is essentially a self-contained calorimeter which consists of a specially coated metal absorbing head with an integral temperature measuring device and a calibrated read out dial with 0.1 kW increments.

In operation, after zeroing the dial, the absorbing head is exposed to the laser beam for a specified time interval. This integrated time interval includes an initial ramping from zero to the specified power followed by a steady-power interval and an instantaneous power shut down. After turning off the laser, the average laser power is read directly off the dial. The probe accuracy is specified to be within 5% with repeatability within 2%.

The versatility and convenience of this technique has allowed us to make laser power measurements at various points within the beam path, to access the losses within the system. We have found the test stand optics system (see Section 2.3) results in approximately a 14% loss in power and beam inlet window on the chamber (see Section 2.4.2) results in approximately a 7% loss in power. This 21% loss in input laser power through the optical system limits our experiments to about 8 kW maximum within the PIFC.

2.3 Test Stand and Optics System

The test stand is constructed of unistrut framing and mounted on four pneumatic tires. The stand is aligned and rigidly positioned by two steel rods which screw into the laboratory floor. The stand supports the beam steering optics, the PIFC, and an electronics panel which integrates the chamber diagnostics systems.

The optical system consists of four copper mirrors which may be configured to focus the beam vertically inside the chamber at one point, or two adjacent points. The incoming laser beam first strikes a flat mirror and is reflected 90° downward onto the split, flat mirror shown in the lower left corner of Figure 12. The two semicircular halves of this mirror may be positioned in a flat or inclined manner relative to each other and reflect the beam up onto a 6.0 inch diameter convex mirror as a single annular or two distinct semi-annular beams, respectively. The convex mirror reflects and expands the beam(s) onto a 20 inch diameter concave primary focusing mirror. The concave mirror then reflects and focuses the beam(s) up inside the chamber through a sodium-chloride window. All mirrors are water cooled to prevent thermal damage except the large concave mirror which has sufficient mass to prevent thermal damage. Figure 12 shows the optical system arrangement from a view facing the laser as well as side views which depict the double focus configuration. By positioning the split mirror halves flat with respect to one another, the incoming beam remains intact and is focused at one point along the centerline inside the chamber. Figure 13 shows details of the split mirror.

This complex off-axis optical system provides three key advantages. First, the beam's vertical focus enhances plasma stability in the axial gas

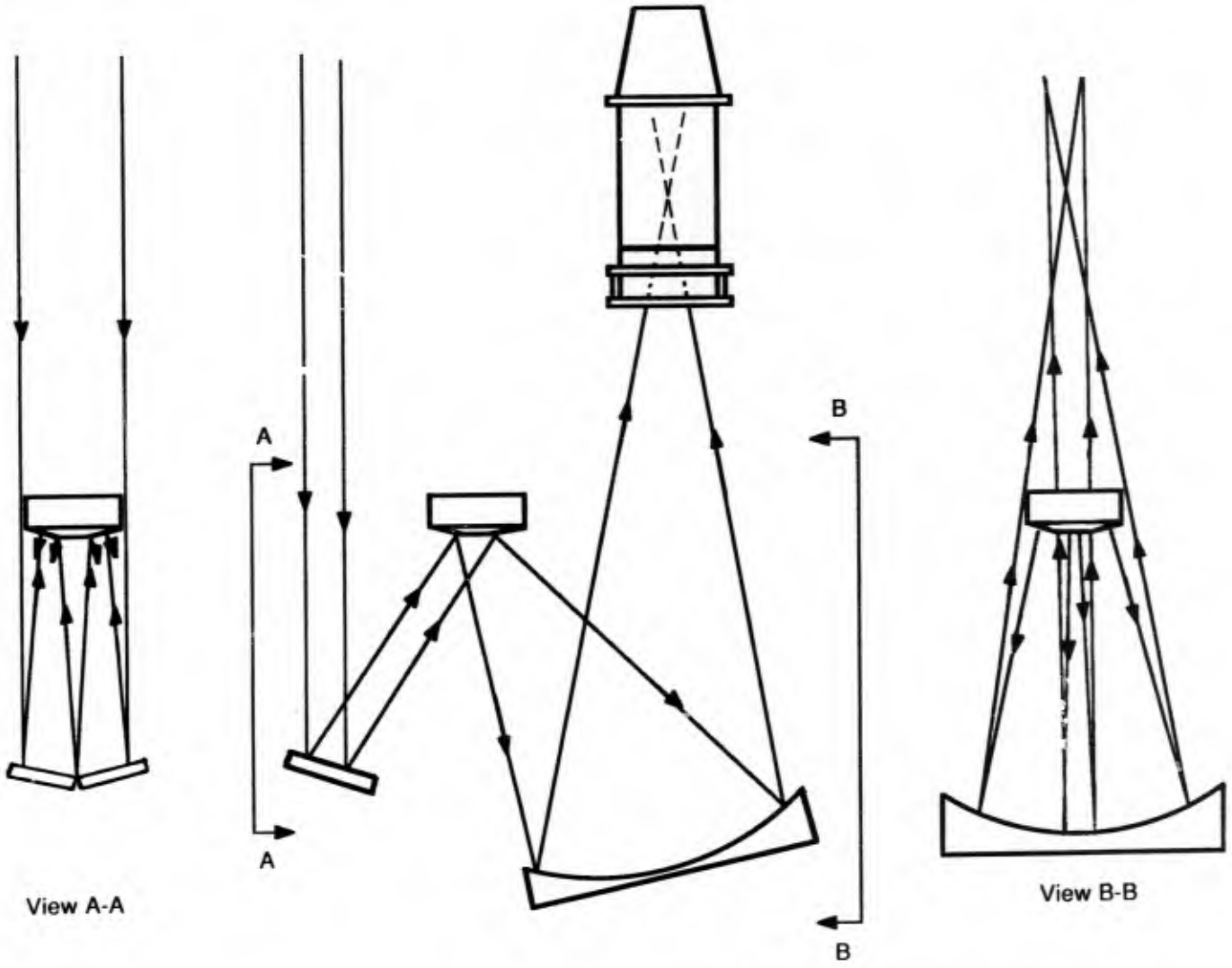

Figure 12: PIFC optical system viewed facing the laser. Views A-A and B-B are side views showing the split beam. The side views are not to scale and the ray traces in these views have been exaggerated for clarity. By positioning the split mirror halves flat with respect to one another, the incoming beam remains intact and focuses at one point along the centerline within the chamber.

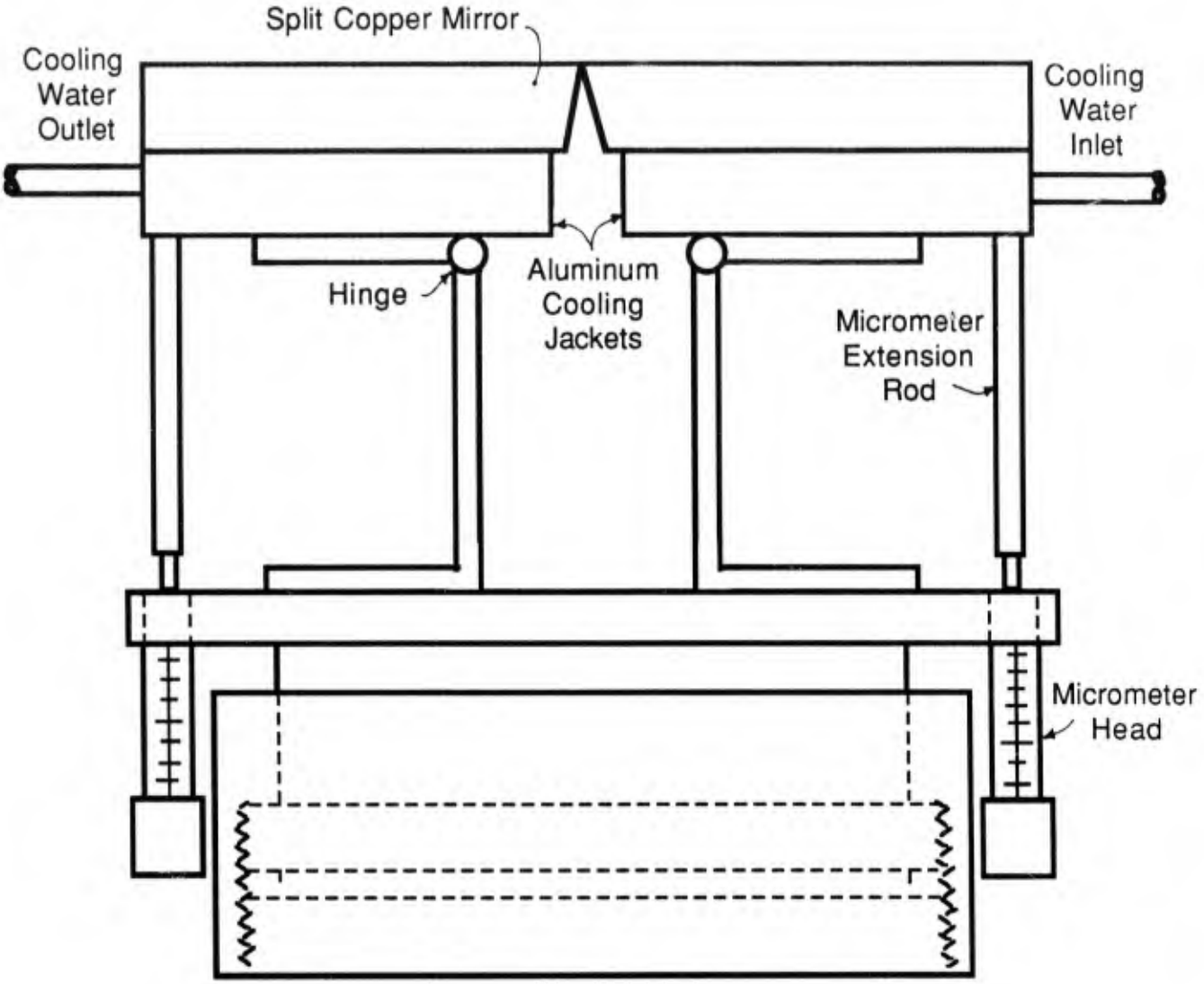

Figure 13: Details of the split mirror.

flow; this flow orientation was chosen to ensure axial symmetry within the chamber in the presence of the highly buoyant plasma. In addition, the system permits a variable f/# (defined from the concave mirror to the focus(es)) of f/2.2 to f/3.4, permitting the study of the effects of beam geometry on plasma stability, shape and absorption characteristics. The f/# is varied by the relative rotation and/or translation of the lower flat, convex and concave mirrors, as shown in Figure 14. Finally the low f/#'s provide a relatively large beam cross-section passing through the salt window, minimizing the radiative intensity and presumably the thermal stresses within the crystalline window.

The main disadvantage of the arrangement is the abberation in the focal volume(s) due to the off-axis nature of the optics system. Qualitative measurements of the focal volume characteristics have been made by visually observing the characteristics of a low power Helium-Neon laser beam which can be propagated through the CO_2 laser optics as well as the test stand optics. In addition, laser burn tests in plexiglass targets have been made using the CO_2 laser and indicate a spot size approximately 1 mm in diameter, at f/2.5, in both focus configurations.

These 'burn' tests indicate the resulting focal volume shape is not a circular but rather an elliptical cone. In addition, in the twin focus configuration, the west focal volume is sharper, resembling a point, whereas the east focal volume is slightly larger and more abberated, resembling a line focus. This characteristic most likely reduces the symmetry of the plasmas because of different spot sizes and thus, focal intensities. Furthermore, the relatively large spot of the east focus sometimes makes plasma ignition difficult at that point because of the reduced beam intensity. One final

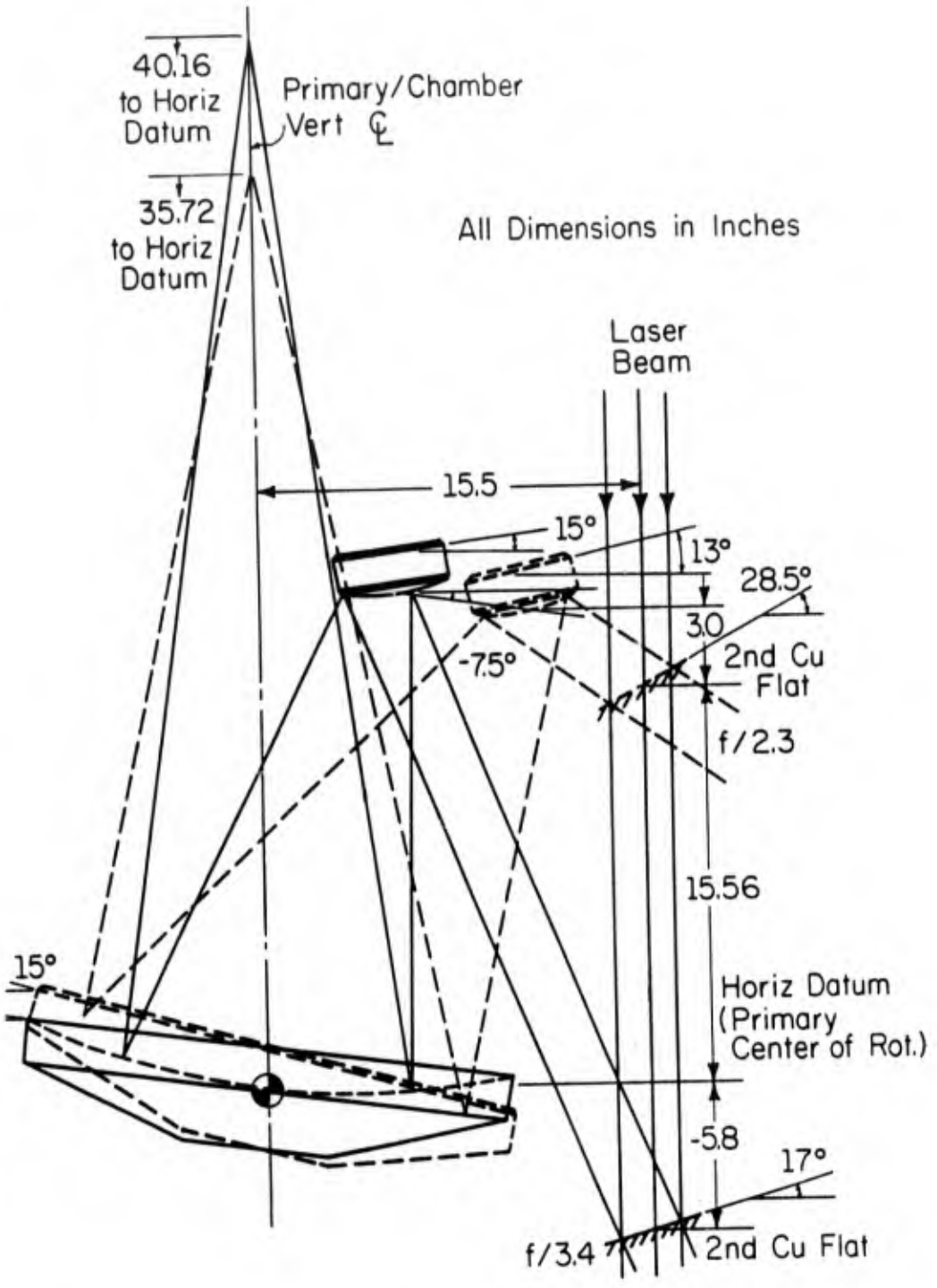

Figure 14: Optical f number is varied from f/2.2 to f/3.4 by changing the separation distance between the two primary mirrors.

disadvantage of this optical system is the limitation on the highest f/# which can be produced. Recent numerical modeling of the laser-sustained plasma indicates substantial increases in thermal efficiencies at higher f/#'s (see Figure 10). In order to verify this experimentally, a high f/# optical system has been designed.

In the revised optical system, the two original flat mirrors are used along with a third flat mirror, which reflects the beam up through a 4.0 inch NaCl lens which in turn focuses the beam. This system, shown in Figure 15, provides the ability to change f/#'s by simply changing lenses. Preliminary tests with window blanks have indicated the need to cool the salt lenses to prevent thermal stresses and cracking. As a result a coolant jacket/lens support assembly has been designed which provides a flow of helium gas over both lens faces. No experiments have been run to date with this new optical system but f/4 and f/8 lenses have been purchased and will be used in high f/# experiments which will be undertaken in the near future.

2.4 Absorption Chamber Assembly

The absorption chamber assembly is shown schematically in Figure 16 with various components labelled. The main body of the assembly is a cylindrical chamber equipped with two rectangular side windows for optical access, pressure and relief valve ports, an axially traversable thermocouple carriage and stepper-motor driver, a port for target insertion, and four radial ports for gas expulsion. At the bottom of the chamber body a hollow-walled cylindrical gas inlet assembly bolts on and provides radial induction of the inlet gas through several 1/8 inch diameter holes. The lower annular face of the gas inlet assembly serves as a receiving flange for the circular salt

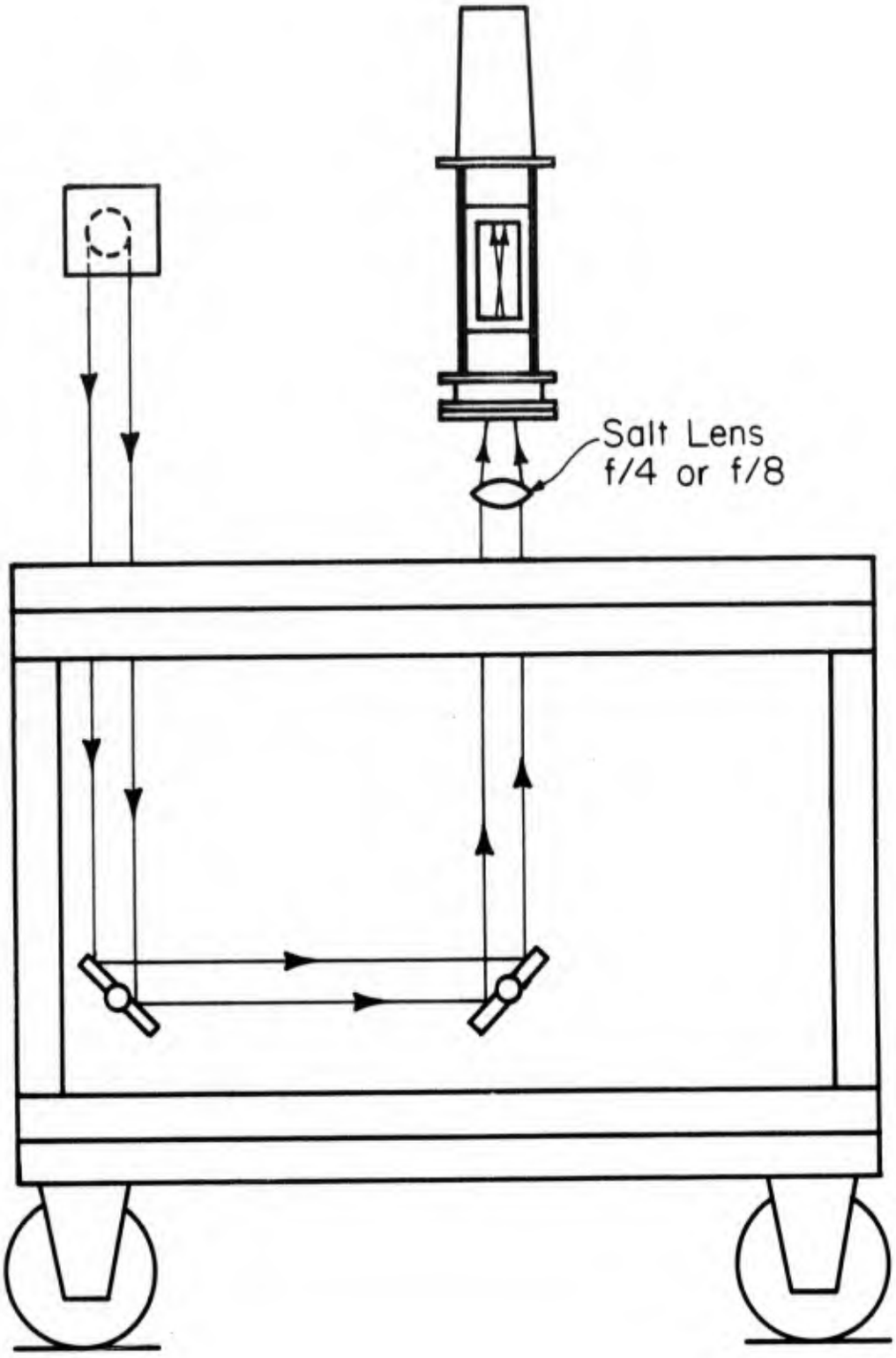

Figure 15: Modified optical system that allows tests at higher f/numbers using NaCl lenses.

(A) Laser Inlet Window Assembly
(B) Gas Inlet Assembly
(C) Three-Eighths Inch Inlet Pipes (2)
(D) Main Chamber Section
(E) Thermocouple Wire Retract Box
(F) Viewing Windows (2)
(G) Target / Solenoid Assembly
(H) Pressure Transducer and Popoff Valve
(I) Three-Eighths Inch Exhaust Pipes (4)
(J) Thermocouple Drive Motor
(K) Calorimeter
(L) Laser Inlet Window

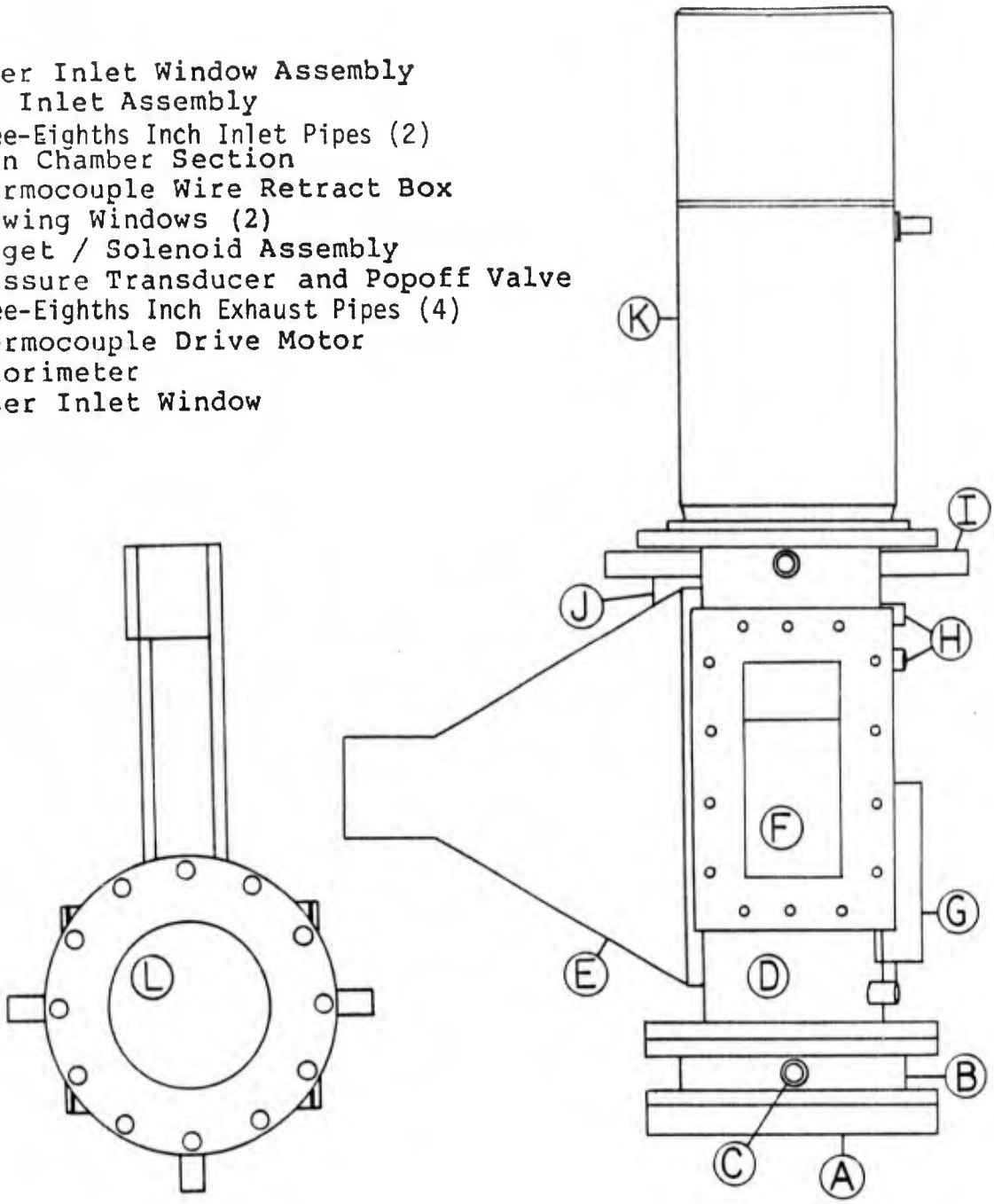

Figure 16: Absorption chamber assembly and components.

window. The window is sandwiched between the receiving flange and an outer annular flange, each of which is equipped with an O-ring to protect and seal the window. In addition, a portion of the inlet gas is directed onto the salt window for cooling purposes.

2.4.1 Chamber Main Section

The stainless steel absorption chamber has a 5.0 inch inside diameter and can be safely operated at pressures up to 5.0 atmospheres gauge. Stainless steel was chosen because of its corrosion resistance, its strength and its relatively high melting point. The large diameter was selected to reduce wall effects associated with the viewing windows and to better withstand the thermal load induced by the highly radiative plasma. The large diameter of this chamber, however, results in relatively low flow velocities for typical gas mass flows. Because the input laser is limited to 10 kW, mass flows must also be limited to insure a significant change in enthalpy flux between the inlet and exhaust flows.

2.4.2 Chamber Windows

The side windows are made of tempered Pyrex and are mounted in a twin-flange assembly similar to the salt window for laser beam inlet. These windows are capable of withstanding gauge pressures of more than 5 atmospheres and transmit ultraviolet (UV) and visible wavelengths relatively well. This characteristic permits spectroscopic diagnostics of the plasma which emits profusely in the UV region. The Pyrex windows strongly absorb 10.6 μm radiation however, and are prone to cracking if stray laser reflections from the initiation target strike them.

Salt windows, typically NaCl, are used for the laser inlet because of their relatively high transmission (~ 90%) at 10.6 μm. The chamber design requires 6 inch diameter windows which reduces the laser flux and tends to prolong window life, but unfortunately, reduces the strength of the window at high pressures due to its large surface area. For pressures near atmospheric, 1/2 inch thick NaCl windows survive reasonably well but are prone to cracking along cleavage planes, presumably due to thermal gradients. In earlier experiments, these windows failed more frequently as a result of molten drops from the zinc foil initiation targets. Recently, a new initiation technique utilizing a tungsten rod target has been implemented and eliminates this cracking problem because the target remains intact.

For higher pressures, the required thickness of NaCl windows becomes impractical and therefore Polytran windows are used. Polytran is a composite crystalline material formed by compressing NaCl at elevated temperatures. These semi-crystalline windows are 1.35 inches thick and are pressure rated to over 5 atmospheres gauge.

2.4.3 Target Insertion System

The peak intensity of the focused laser beam is on the order of 10^6 W/cm^2 and is insufficient to initiate a plasma in the flowing gas without an initial source of electrons. Free electrons are formed by inserting a reusable tungsten rod target into the focal region by means of a solenoid operated air-cylinder. Thermionic emission and target vaporization create a high enough electron density to trigger an electron cascade which results in a plasma. At this point the target is retracted to minimize damage and relieve its intrusive effect on the plasma and gas flow.

The target insertion system is depicted in Figure 17. The tungsten rod is inserted into a coupling which attaches to the air cylinder piston arm. Generally the tungsten target must be replaced regularly to ensure easy initiation. The target is ground flat on its lower side to reduce laser reflections onto the Pyrex windows.

2.4.4 Thermocouple Carriage

The working gas temperature distribution currently can be measured at various locations by an array of high temperature thermocouples positioned transversely within the absorption chamber. The thermocouples are attached to an annular stainless steel carriage by a set of pivotable locating pins as shown in Figure 18. The leads are routed out of the chamber through the thermocouple retract box shown earlier in Figure 16. As many as twelve thermocouples can be supported by the carriage, but typically only six to eight are used to prevent excessive flow disturbances, while maintaining adequate measurement resolution. This scheme allows a variety of radial thermocouple configurations and facilitates simultaneous multi-point temperature measurements at a particular cross-section within the chamber. In addition, volumetric temperature measurements can also be performed because the carriage, by design, may be moved axially within the chamber. Two hollow cylindrical tubes, mounted in the carriage, slide on a pair of stainless steel rods mounted vertically just inside and along the inner chamber wall. The carriage is suspended and conveyed by a chain and sprocket assembly driven by a computer controlled stepper-motor. The sprockets are located along the inner chamber wall, the upper sprocket being the driver and the lower sprocket the driven.

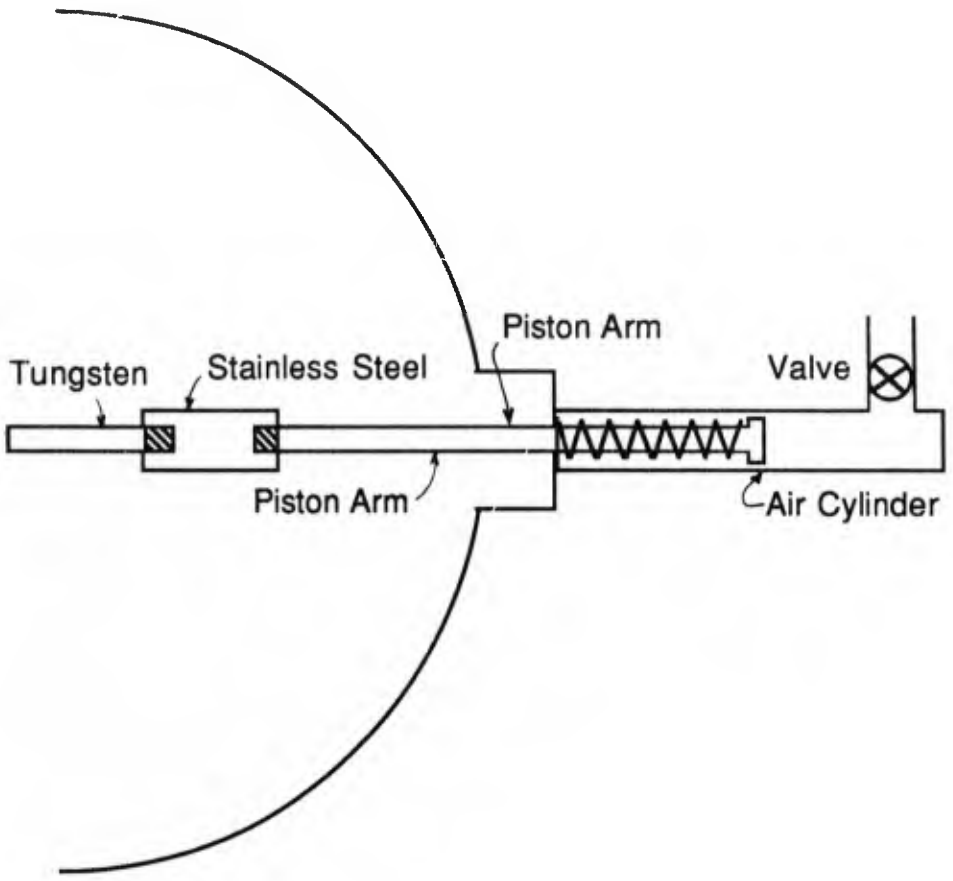

Figure 17: Schematic operation of the target insertion system. A solenoid operated valve allows high-pressure gas to enter the air cylinder, moving the piston arm into the chamber. The target is a tungsten rod ground flat on its lower side to reduce laser reflections onto the Pyrex windows.

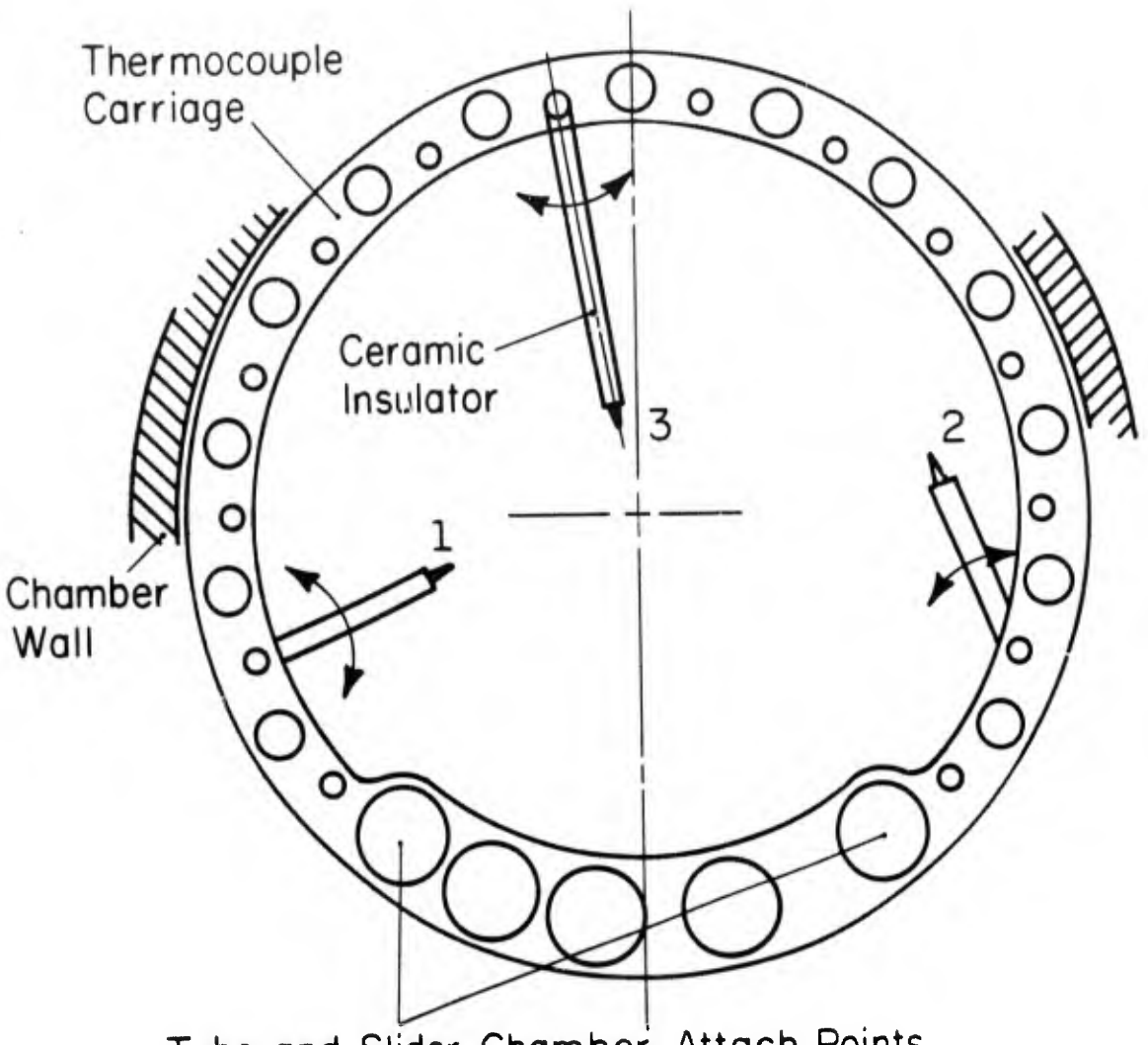

Figure 18: Thermocouple carriage with high-temperature thermocouples attached on pivotable mounts.

The thermocouples currently in use are type D and are made from the high temperature alloys Tungsten with 3% Rhenium and Tungsten with 25% Rhenium. They have 0.005 inch diameter leads and have a maximum service temperature of approximately 3000 K for short term exposure. These high temperature thermocouples were chosen to allow gas temperature measurements as close to the plasma as possible but more common thermocouples may be used in the exit plane since the temperatures there are generally no higher than 900 K. The small diameter leads were chosen to reduce the response time for the thermocuples by reducing the thermal inertia of the bead.

The thermocouples are positioned within the chamber perpendicular to the flow direction and therefore must be supported with a sheath to prevent deflection due to the flowing gas. Currently, two-hole round ceramic insulators are used to insulate and support the leads, with the bead and a very small length of the leads exposed to the flow, for a better response time. The bare wire leads are threaded through the two holes in the ceramic insulator and thus are electrically insulated to prevent accidental shorting. Twin cylindrical copper shields are placed coaxially around the ceramic insulators to minimize temperature measurement errors caused when the transmitted laser beam is incident on the thermocouple sheaths. These shields are described more thoroughly in Section 5.1.1.

2.4.5 Calorimeter

An AVCO-Everett high-flux, copper-cone calorimeter is mounted above the chamber and collects all of the incident laser energy that is either transmitted or forward-scattered through the plasma. The copper cone internally reflects the collected laser energy until all of it is absorbed within the

copper cone. The calorimeter is thus used as a beam dump and may be used to determine the transmitted portion of the input laser beam, neglecting incident plasma radiation. This measurement is used indirectly to indicate how much laser energy is absorbed by the plasma.

The amount of energy collected is measured by monitoring the temperature change in the flow of cooling water through the calorimeter. Water temperatures at the inlet and exit are monitored by two internal arrays of thermocouples, and the flow rate of the cooling water is controlled by a pressure regulator and volumetric flowmeter. An electronics package supplied by the manufacturer interprets the change in water temperature indicating the change in enthalpy flux. The change in enthalpy flux of the water is a measure of the collected laser power. This signal is then displayed and recorded on a strip chart recorder. The original calorimeter design has been modified slightly to withstand high pressure operation.

2.5 Gas Flow System

There are currently two gas flow systems available to deliver the working gas to the PIFC. Both systems are very similar in design, but individual component differences make each system useful for a different flow regime. One system is utilized for relatively low chamber mass flows of argon, while the other system provides higher mass flows of argon. Figure 19 depicts a general schematic of both gas flow systems with the specific components and capabilities summarized in Table 1.

In general, each system uses high pressure regulated tanks outside the laboratory for a gas source to feed a primary trunk line. The primary hose delivers the gas inside the control room and connects to a variable area

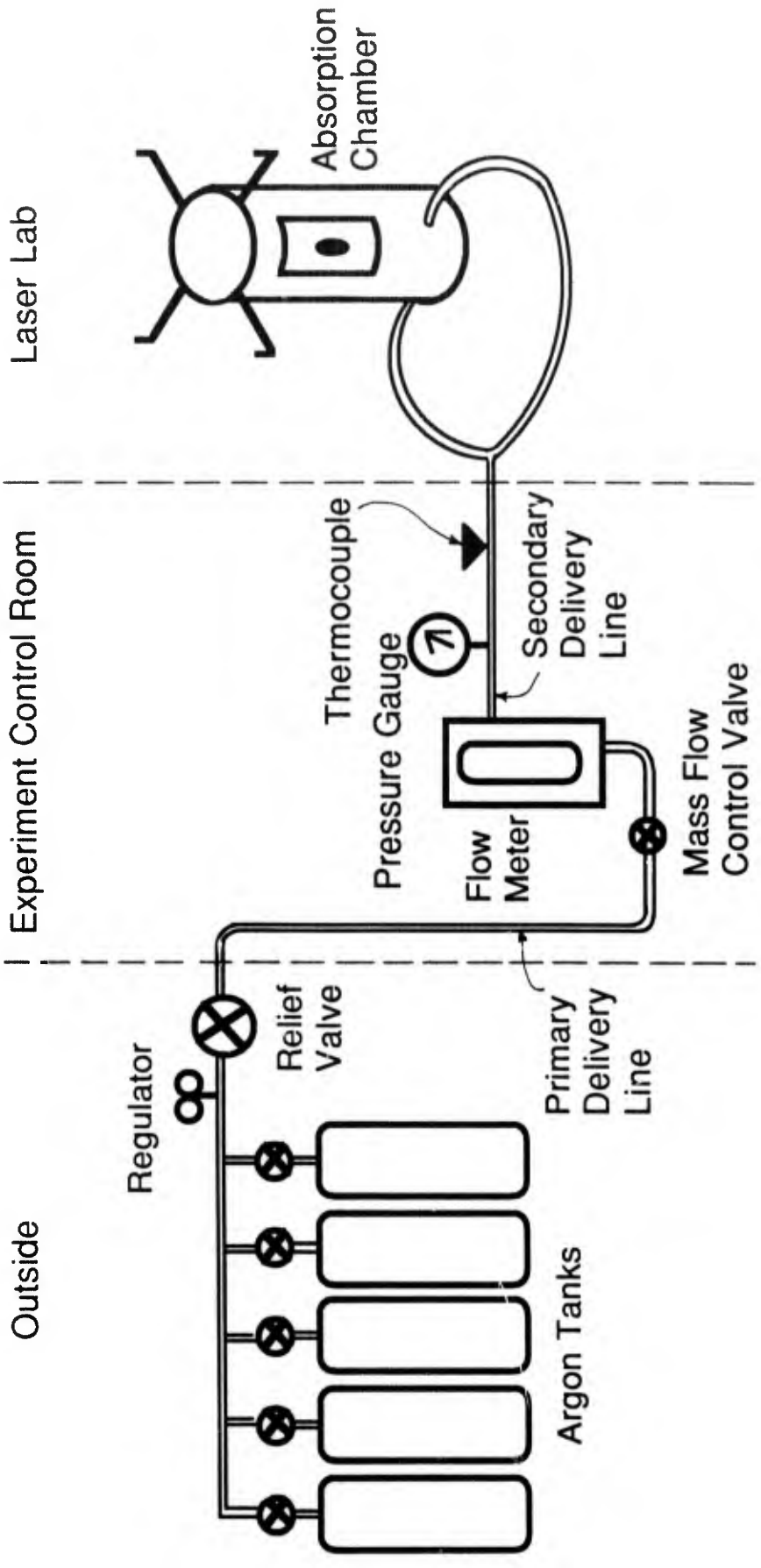

Figure 19: General schematic of the gas flow delivery system.

fullview flowmeter, where the flow is manually regulated by a control valve. The gas pressure and temperature are measured at the flowmeter exit for accurate mass flow determination. A secondary hose delivers the gas to the test stand where the flow is split to feed the twin inlet pipes of the gas inlet assembly. The gas is exhausted from the chamber through four symmetrically positioned radial pipes, each with a 3/8 inch inside diameter.

Currently the chamber gas exhausts to the ambient, thus precluding experiments at pressures higher than atmospheric. Experiments can be undertaken at higher pressures by connecting the chamber exhaust pipes to a manifold exhausting through one port, with a valve controlled back pressure. The earlier chamber design included this option but the exhaust system choked at the higher mass flows. This choking resulted in pressure buildup within the chamber and precluded runs with these mass flows at atmospheric pressure. A new manifold system will be designed in the future which will permit high pressure tests at high mass flowrates.

TABLE 1

FLOW SYSTEM COMPONENTS AND CAPABILITIES

ITEM	LOW FLOW SYSTEM	HIGH FLOW SYSTEM
Gas Source	one 300 scf* tank	five 300 sfc tanks in series
Primary Line	3/8" ID Hytran Hose (9000 psi burst pressure)	3/4" ID Hytran Hose (9000 psi burst pressure)
Flowmeter	Brooks 1110A Variable Area Glass Tube Flowmeter with 300 psig rating	Brooks 3622A Variable Area Metal Tube with 1500 psig rating
Secondary Line	1/4" ID polyflow tube (250 psig burst pressure)	3/4" ID Hytran Hose 9000 psig burst pressure)
Chamber Inlet Line	1/2" ID Hytran Hose connected to 3/8" ID inlet pipe	1/2" ID Hytran Hose connected to 3/8" ID inlet pipe
Argon Mass Flows	0 - 25 g/s	10 - 100 g/s
Chamber Velocities of Argon	0 -125 cm/s	50 - 500 cm/s

*Standard cubic feet of gas

SECTION 3: SPECTROSCOPIC STUDIES OF THE LASER-SUSTAINED PLASMA

3.1 Introduction

The key scientific issue for laser propulsion is gas heating by laser induced plasma. The concept of laser propulsion was first proposed in the early 1960s [7]. The concept is that a ground- or satellite-based laser source be directed and focused into an absorption chamber onboard a payload. Direct laser heating of the propellant occurs upon plasma formation. The heated gas is subsequently expanded converting thermal energy to kinetic energy or thrust. The relatively simple absorption chamber eliminates much of the mass involved in classical chemical propulsion systems. Since combustion is not involved, low molecular weight propellants can be used, further reducing mass. Moderate thrust levels at high specific impulse appear feasible for low-earth to geosynchronus orbital transfer missions.

Although several efforts have studied pulsed and CW laser propulsion concepts, [8,9,10] the two main ongoing CW investigations are at the University of Tennessee [11] and the University of Illinois. The work by Keefer, Welle, and Peters [11] has concentrated on the plasma dynamics as a function of laser beam mode and optical focusing characteristics at sub-kilowatt laser powers and relatively high flow rates (0.4 to 4.5 m/s). To date the results indicated that over 65 percent of the incident laser energy can be absorbed and thermal efficiencies approaching 40 percent are attainable. The effort continues to study the effects of aberration in the focusing system and may soon begin to study the effects of a Gaussian TEM_{oo} profile versus the current unstable oscillator configuration. Higher flow rate systems are being designed and kinetic energy measurement in a vacuum has been proposed.

The Tennessee studies have relied solely on temperature data calculated from the absolute continuum emission of Argon in a 1.0 nm band centered at 626.5 nm. A new spectroscopic system is currently being implemented to measure relative spectral events similar to the technique used in the authors' effort. The Tennessee program has also been involved in analytical and numerical modeling of flowing gas laser heating. Most recently Jeng and Keefer [12] reported a full two-dimensional solution of the incompressible Navier-Stokes equation. The results agree with experimental data but the model has not been reported to have been used to develop scaling laws.

Our effort paralleled the Tennessee effort. The Illinois investigation utilized an AVCO Everett 10 kW CW laser and an off-axis optical system. Plans are underway to study higher flow rates, as in the Tennessee studies, at the higher laser powers. In general, the two efforts have complimented each other. Our effort has also included the development of a theoretical model [4]. The model is quasi-two-dimensional in that axial convection is accounted for in addition to two-dimensional conduction. Real gas properties have been used and the results agree with experiment, including spectroscopically measured spatial extent and temperature fields.

This section includes a summary of the spectroscopic work pursued under this AFOSR sponsored research. The spectroscopic studies are one of the first to examine plasma characteristics over this high a range of laser power and range of flow rates. The spectroscopic results have been used to verify a numerical model which has been used to develop scaling laws at realistic laser powers. The spectroscopic results have been shown to agree with independent measurements techniques and have been utilized in the assessment of laser thrusters.

3.2 Plasma Physics

When a laser of sufficient energy is focused into a gaseous medium (10^9 W/cm^2), a plasma will form. The plasma can be 10 percent to completely ionized. This investigation is concerned with low temperatures plasmas in the 5,000 to 20,000 K range. The plasmas form at or near atmospheric pressures which implies equilibrium number densities on the order of 10^{16} to 10^{17} cm^{-3} for the heavy particles and electrons [13].

The plasma is initiated via multiphoton absorption and avalanche breakdown. The probability of multiphoton absorption is low, requiring 130 photons at 10.6 μm to ionize argon, neglecting loss processes. Multiphoton absorption is, however, important once the plasma has formed since the first excited level of argon is approximately 70 percent of the ionization potential. In avalanche breakdown, a large number of initial free electrons is necessary to overcome loss mechanisms. Photon absorption by an electron in the presence of a heavy particle is termed inverse bremsstrahlung absorption, the primary mechanism for plasma initiation and maintenance. If the laser intensity is sufficient, the local electrons will attain an energy high enough to ionize an atom during collision. The process results in two free electrons which continue the process and hence the avalanche phenomena.

The loss mechanisms include diffusion, recombination, and both elastic and inelastic collisions. Electron diffusion should be a minimal effect due to the relatively large focal volumes and high number densities. Recombination is a highly probable process, especially in the cooler regions of the plasma. Elastics are typically modeled as hard-sphere interactions where the electron gives up the mass ratio of energy per collision. Inelastics become important in the high temperature regions of the plasma, an effect again due to the high first excited level of argon and the inerts.

The result of the above processes is that a threshold exists for plasma initiation. The threshold laser intensity required for a cold gas is on the order of 10^{12} W/cm^2. If the gas is preionized via arc discharge to an electron density of 10^{11} cm^{-3}, the threshold intensity can be reduced to 10^9 W/cm^2. In this investigation and elsewhere, a metallic target was irradiated for preionization purposes. Thermionic emission and vaporization result in local electron densities in excess of 10^{14} cm^{-3} for which the threshold intensity is reduced to attainable levels of 10^5 to 10^6 W/cm^2. Once the plasma is initiated, lower intensities are required for maintenance, on the order of 10^5 to 10^6 W/cm^2. Thus by using the metallic targets for initiation, there is little difference between intensity needed for initiation and maintenance.

Inverse bremsstrahlung absorption is the primary mechanism in laser supported plasma. The absorption coefficient can be derived via classical or quantum theory. For calculation purposes the classical derivation [14] is simpler to use. The classical derivation suffers from a lack of individual terms such as stimulated emission losses. Wheeler and Fielding [15] corrected the classical result for stimulated emission in argon by the derivation of an exponential loss term. Wheeler also accounted for non-hydrogenic behavior by utilizing the free-free Gaunt factor, g_{ff}, and an effective ion charge, $\bar{Z}$. Stallcop [16] corrected the Gaunt factor to account for electron-atom inverse bremsstrahlung. Stallcop also included a term, $h\nu/kT_e$, to account for photoionization. The result is an effective inverse bremsstrahlung absorption coefficient

$$\alpha(m^{-1}) = \frac{4}{3} \frac{2\pi e^6 \bar{Z}}{\sqrt{6\pi k m_e^3}\, hc^4} \frac{N_e^2 \lambda^3}{T_e^{1/2}} [1 - \exp(-h\nu/kT_e)] \cdot (\bar{g}_{ff} + h\nu/kT_e) \qquad (1)$$

where N_e and T_e are the electron number density and temperature, respectively, λ the laser wavelength, ν the laser frequency with the remaining being standard constants. Equation (1) has been used in the calculation of power absorption for a laser beam propagating through the spectroscopically measured temperature fields as well as a numerical model [4]. The absorption coefficient operates on laser intensity as derived from the radiative transport equation

$$I_{\omega out} = I_{\omega in} \exp(-\alpha_\omega Z) \tag{2}$$

where I_ω is the frequency-dependent laser intensity and Z is the distance traveled through the medium.

The radiative transport is comprised of bound-bound, free-bound, and free-free emission. The bound-bound or line radiation can be expressed via quantum theory as

$$I_\lambda = \frac{hcA_{mn}g_m N}{4\pi\lambda Z_e} \exp(-E_m/kT_e) \tag{3}$$

where I is the intensity (W/cm^3-sr) at wavelength λ, A_{mn} is the transition probability, g_m the upper level degeneracy, N the atomic number density, Z_e the electronic partition function, and E_m the upper level energy. This is quantum theory for emission at a pure wavelength, λ. In practice, the measured spectra will be broadened via Doppler and/or Stark effects. However, theory can be applied to the integrated measured profiles with little error.

The free-bound and free-free processes are continuous and can be summed over all internal energy levels. Applying Kramers-Unsold theory [14], the integrated continuum intensity can be expressed as

$$I_{c\lambda} = 5.44 \times 10^{-46} c\bar{g}\, Z_{eff}^2 \frac{N_i N_e}{T_e^{\frac{1}{2}}} \frac{\Delta\lambda}{\lambda^2} \tag{4}$$

where $I_{c\lambda}$ is the intensity (W/cm^3-sr) summed over the wavelength $\Delta\lambda$, $\bar{g}$ is the average Gaunt factor, and Z_{eff} is the effective charge of the local plasma volume. In general the plasmas are treated as optically thin and the optically thick transport is treated as a radiative conductivity term in the energy equation. Equation (5) tends to smooth the continuum but is adequate for integrated calculations. In the VUV the radiation is trapped and is modeled as a blackbody. The IR spectrum is generally opaque due to the strong inverse bremsstrahlung process. A general rule for the visible and UV spectra is that self-absorption is critical when

$$p\ell > 10 \text{ to } 50 \text{ atm-cm} \tag{5}$$

where p is the local pressure and ℓ is a characteristic length of the plasma. In this investigation, $p\ell$ is typically on the order of 1 to 2 atm-cm and self-absorption effects should be minimal.

The plasma upon initiation will propagate into the converging laser beam. For the laser intensities considered herein, the propagation velocity is dependent upon local intensity and is subsonic. The plasma is analogous to combustion wave phenomena and hence is called a laser supported combustion wave (LSC). The plasma front will stabilize at the point where the local plasma expansion velocity matches the impressed flow velocity. The plasma is weakly absorbing with conduction driving the upstream plasma propagation. The weakly absorbing plasma front allows sufficient laser energy, to be transmitted to support the downstream plasma volume.

Pure argon plasmas have been investigated from consideration of safety and well documented thermophysical properties. Figure 20 is a schematic of the physics of a flowing gas laser supported plasma (LSP) system. The plasma is initiated by inserting a tungsten target at the laser focus. The thermionic emission from the target is sufficient to initiate the plasma in the flowing argon whereupon the target is removed. The absorption mechanism is dominated by inverse bremsstrahlung and conduction drives the plasma volume outside the laser geometry.

At this point it should be noted that local thermodynamic equilibrium (LTE) has been assumed throughout this investigation. LTE is the assumption that the various particles have Maxwellian velocity distributions albeit not necessarily at identical characteristic temperatures. LTE also implies that collisional processes dominate the rate equations such that Boltzmann statistics apply. Griem [17] notes that for LTE to apply, the electron and heavy particle temperatures should be similar. This is due to the short heavy particle mean free paths which offset the mass ratio energy transfer during collisions. Utilizing the above assumptions for argon, the Saha equation is used to determine that an electron density of 10^{16} cm^{-3} is sufficient to satisfy LTE.

Farmer and Haddad [18] attempted to experimentally verify that LTE is an argon arc plasma. The measured emission coefficient should be identical for regions of identical temperature within the plasma. The off-axis peak in the emission profile was used as a norm temperature and the two-dimensional field was calibrated about the norm temperature. The authors concluded that an arc plasma at 1.4 atm was incomplete LTE (± 5 percent). At 1.0 atm, the plasma was generally in LTE except for a few millimeters near the cathode. Charge

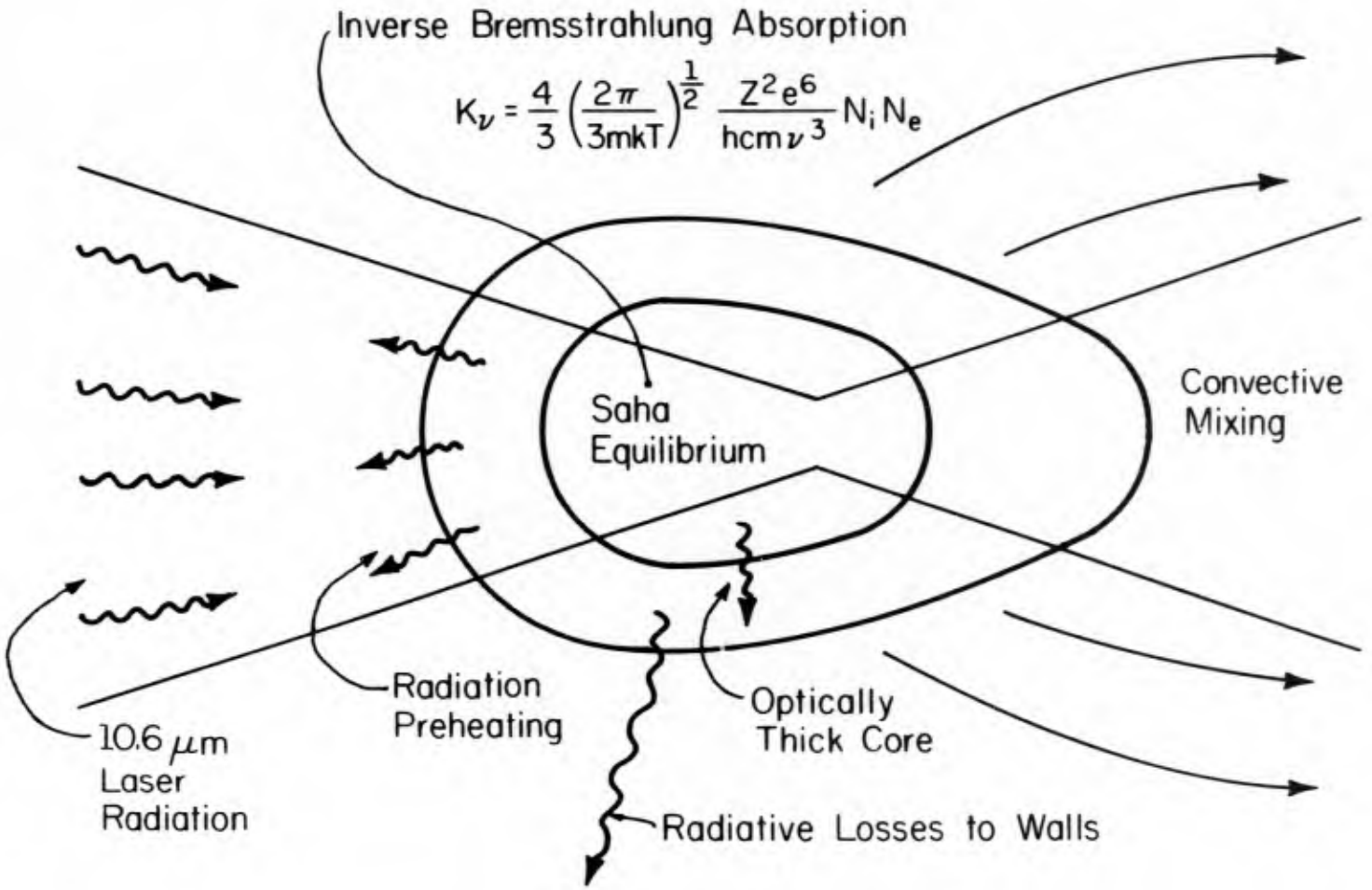

Figure 20: Pure Gas Plasma Physics

repulsion could be an effect near the cathode and it appears that atmospheric pressure laser supported plasmas are reasonably close to LTE. Finally, theory can be combined with experiment to derive a function proportional to the electron velocity distribution. Gas kinetic theory can be used to determine the thermal conductivity of argon as a function of the effective momentum transfer cross-section, $\langle q \rangle$. Applying conductivity data of, e.g. Emmons [19] one can calculate $\langle q(T_e) \rangle$. Using the data of Golden and Bandel [20] for the total momentum transfer cross-section, q(E), it is possible to derive the energy distribution function, f(E), (non-normalized)

$$\langle q(E) \rangle \alpha \int q(E)\ f(E)\ dE. \qquad (6)$$

Differentiating and inverting Eq. (6) results in an expression for f(E). It has been shown for the above data and others that f(E) is a Maxwellian, i.e. straight line on a logarithmic energy plot. The worst case calculated was a two-temperature system with the break occurring at about 9000 K below the resolvable temperatures for the spectral diagnostics used in this effort. Thus satisfied that the atmospheric argon systems are reasonably close to LTE, one may proceed with data analysis which otherwise would be unwieldy.

3.3. Experimental Procedure

The spectroscopic data is acquired by imaging the plasma through the diagnostic windows onto a vidicon detector. The system used was an EG&G PARC Optical Multichannel Analyzer (OMA) III, a schematic of which is shown in Figure 21. A simple lens images the plasma (inverted) onto the horizontal slit of a 0.32 m Czerny-Turner spectrograph. The vidicon is a silicon

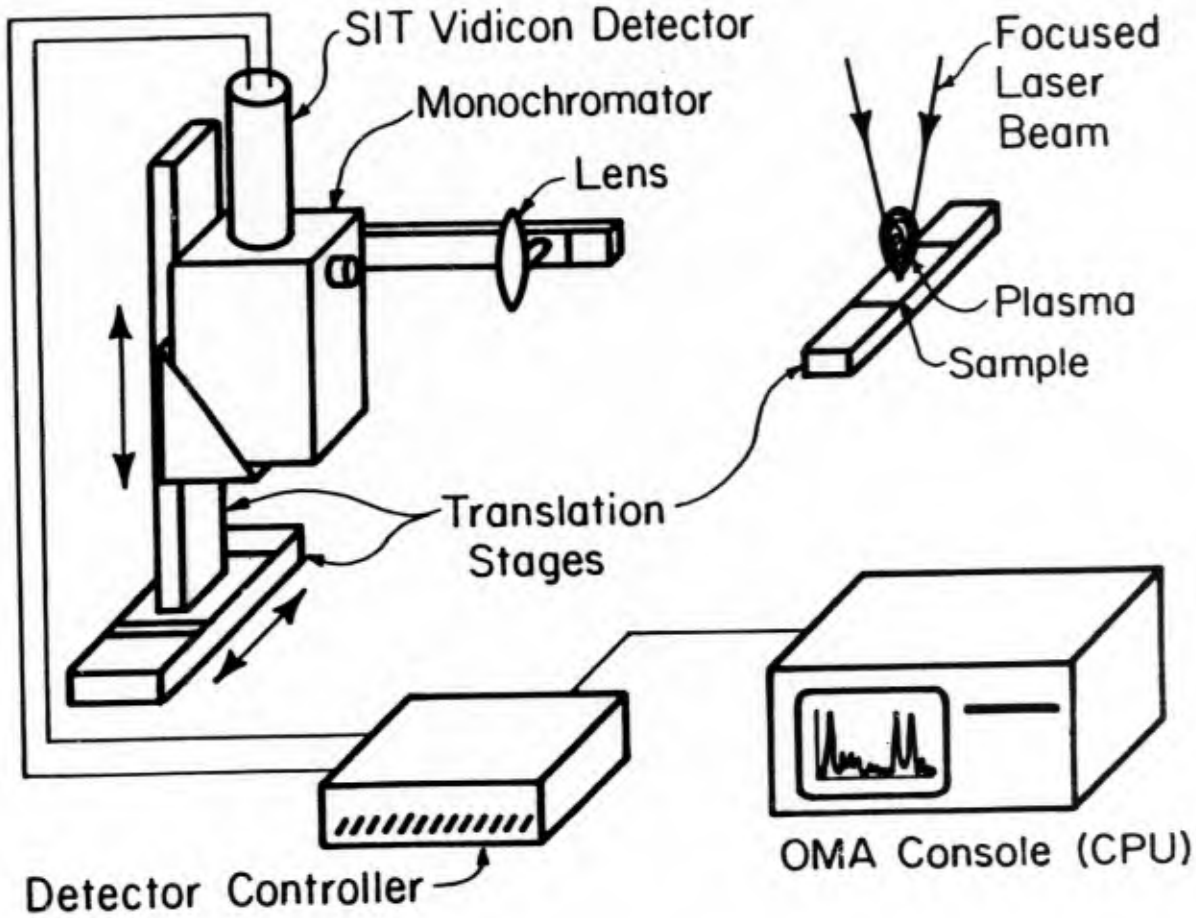

Figure 21: Optical Multichannel Analyzer (OMA) Schematic

intensified target (EG&G model 1254) with a UV scintillator applied for responses down to 200 nm. The OMA console is the CPU which configures the scanning sequence of the two-dimensional detector as well as data formatting, storage, and limited data reduction functions. The monochromator and optics are mounted on an X-Z translation stage. The X-stage (horizontal) is used for fine tuning the plasma position on the entrance slit and the system is initially aligned with an HeNe laser propagating through the target (focus) region to adjust the optical axis of the monochromator system.

Once the plasma has been initialized, the data at the entrance slit is expanded spectrally onto the vidicon. The result is a three-dimensional set of data corresponding to wavelength (x), radial position (y), and line-of-sight intensity (Z) as shown in Figure 22. The monochromator was typically used with a 1200 line/mm grating for which the detector resolution is 0.6 angstroms near the 415.8 nm spectrum. The lens system (f/#) has been matched to the monochromator f/# at the given wavelength, rendering a typical resolution of 0.3 mm radially and axially for a 0.1 mm slit width. Once a given radial data set has been acquired and stored, the monochromator system is translated vertically to the next axial location and the process is repeated. The plasmas required between 5 and 10 minutes for complete spectral mapping of the core region (see Figure 20).

The data is the line-of-sight intensity (W/cm^2-sr) integrated over the various annuli. To utilize the data for comparison with Eqs. (3) or (4), the profiles must be deconvoluted to determine point emissivities (W/cm^3-sr). For the deconvolution the Abel inversion procedure and a numerical scheme following the work of Cremers and Birkebak [21] was used. The particular method is a relatively simple technique which minimizes inversion error. The technique

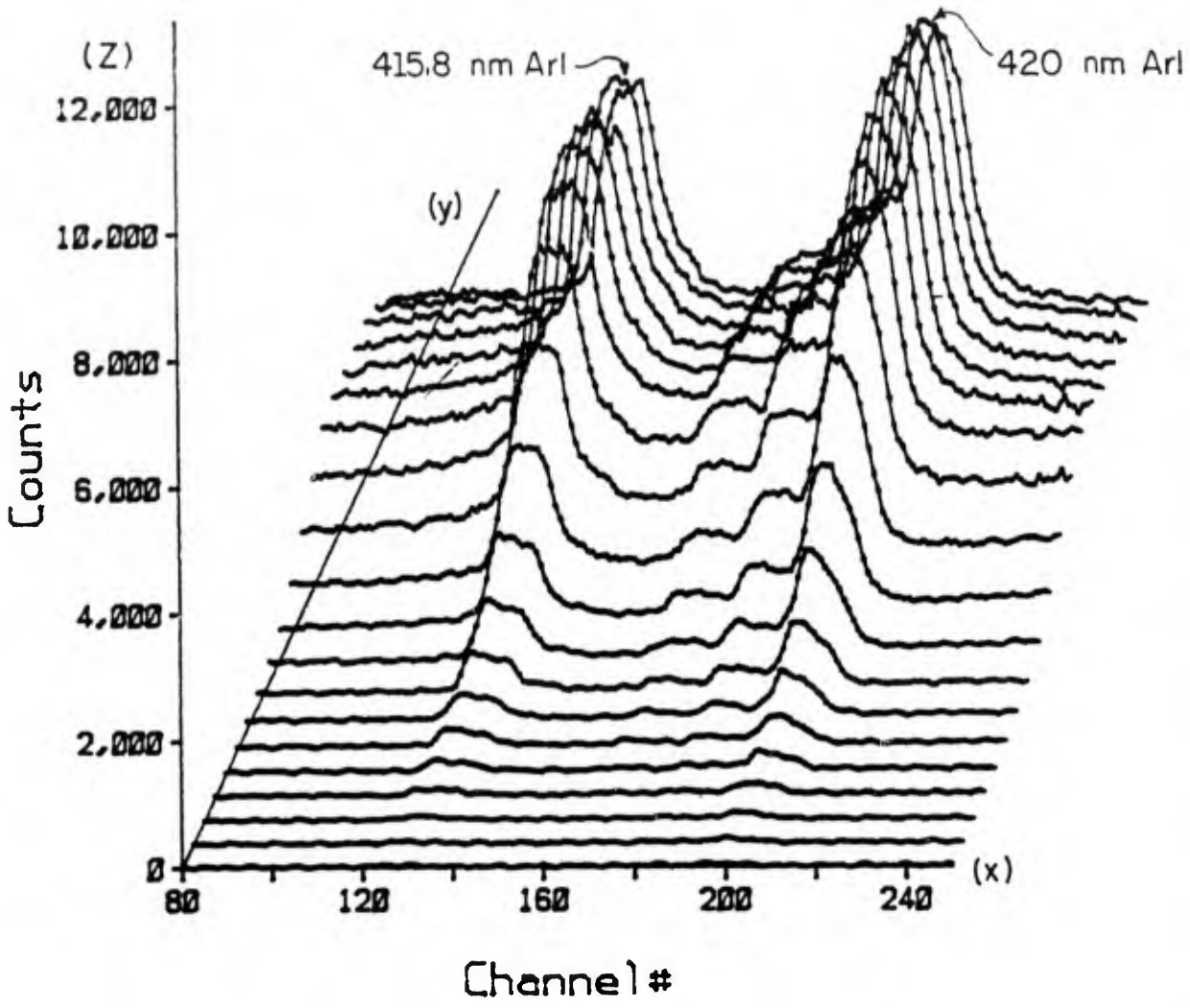

Figure 22: Example of a Multitrack Data Set

can invert flattened centerline intensity profiles, typical of laboratory plasmas, without blowing-up as some of the earlier techniques did. Once the point emissivity of a given line structure (background and continuum subtracted) and adjacent continuum band is determined, it can be ratioed and compared to theory via the ratio of Eq. (3) to Eq. (4) to determine local electron temperatures. In this study the 415.8 nm ArI line and adjacent continuum were utilized in most cases since it is a strong system and reasonably separated from other line structures. Work at 696.5 nm ArI and 457.9/458.9 nm ArII structures was within experimental error of the 415.8 nm data for spatial, temperature, and global property values.

Once the two-dimensional electron temperature field has been calculated, the field is analyzed to determine global absorption, radiative losses, and the effects of beam refraction. A computer code was written for this purpose. The incident laser beam is broken into 20 rays across the annulus, each weighted to a Gaussian. The beam is then propagated into the temperature field, and the intersection of each ray with the radial temperature profile at a given axial location is determined. The local absorption coefficient is calculated (Eq. (1)) and the ray intensity transmitted to the next cell is determined via Eq. (2). Beam refraction is calculated using the adjacent radial temperatures after the work of Cheng and Casperson [22]. In the case of pure argon plasmas, the effect of refraction has been seen to be negligible. However, the effect is considerable when plasmas above metallic targets are analyzed [23]. The radiative losses were calculated on a cell-by-cell basis. Continuum radiation was calculated using Eq. (4). Line radiation losses were calculated as a function of the local temperature and the continuum emission after the work of Kozlov [24].

The power absorbed was calculated by summing the incident and exiting ray weights, ratioing the sums and multiplying them by the measured incident power. Once absorbed power and radiative losses are determined, the net power retained by the gas can be calculated, neglecting any convective losses. The thermal efficiency is then determined by

$$\eta_{th} = (100)\ \frac{P_{retained}}{P_{incident}} \tag{7}$$

where η_{th} is thermal efficiency and P is power.

3.4 Single Plasma Experimental Results and Discussion

The following data corresponds to the 415.8 nm ArI line relative to the adjacent blue wing continuum discussed in the previous section. Figure 23 depicts the spatial dependence of plasma extent as a function of power at f/2.4 and 15 cm/s argon flow velocity. Figure 23a is for 2.4 kW, Figure 23b for 4.1 kW, and Figure 23c for 5.5 kW. The peak temperature, in general, increases with laser power from 17,500 K in Figure 23a to 19,000 K in Figure 23c. The important trend is that the 17,000 K core region has grown significantly with increasing laser power. The plasma core and front have moved further into the converging beam as power is increased.

The global absorption was calculated to be 60.0 percent (1,440 W), 72.9 percent (2,990 W), and 82.9 percent (4,560 W) for 2.4, 4.1, and 5.5 kW, respectively. Figure 24 is a comparison between the spectroscopic data and the theoretical model [4]. The error bars represent a ±4 percent fluctuation in temperature. This value was determined from an error analysis of the Abel inversion algorithm, assuming a ±10 percent error in intensity measurement.

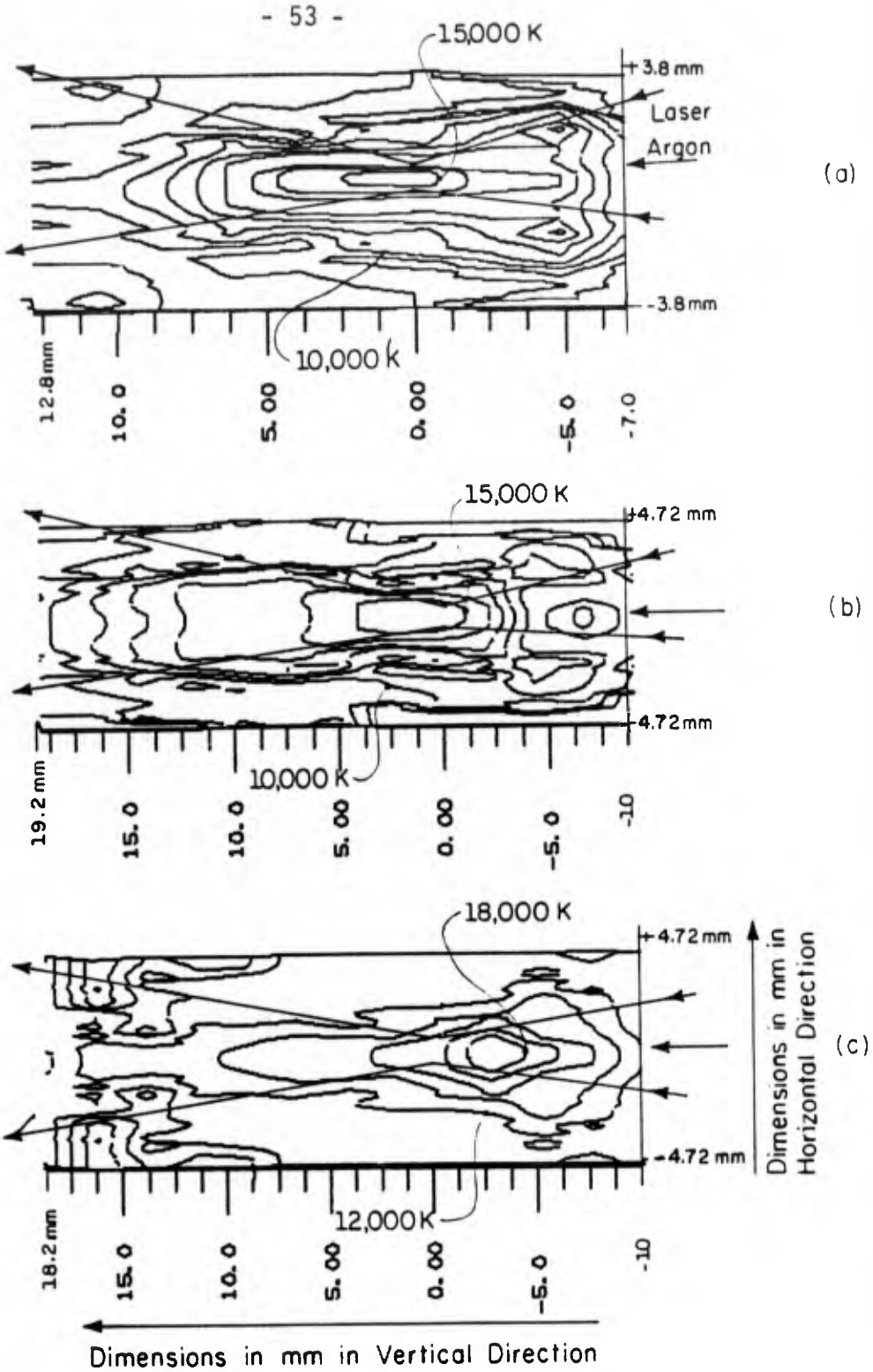

Figure 23: Two-Dimensional Temperature Fields of: (a) 2.4 kW, (b) 4.1 kW, and (c) 5.5 kW Pure Argon Plasma, f/2.4, 15 cm/sec

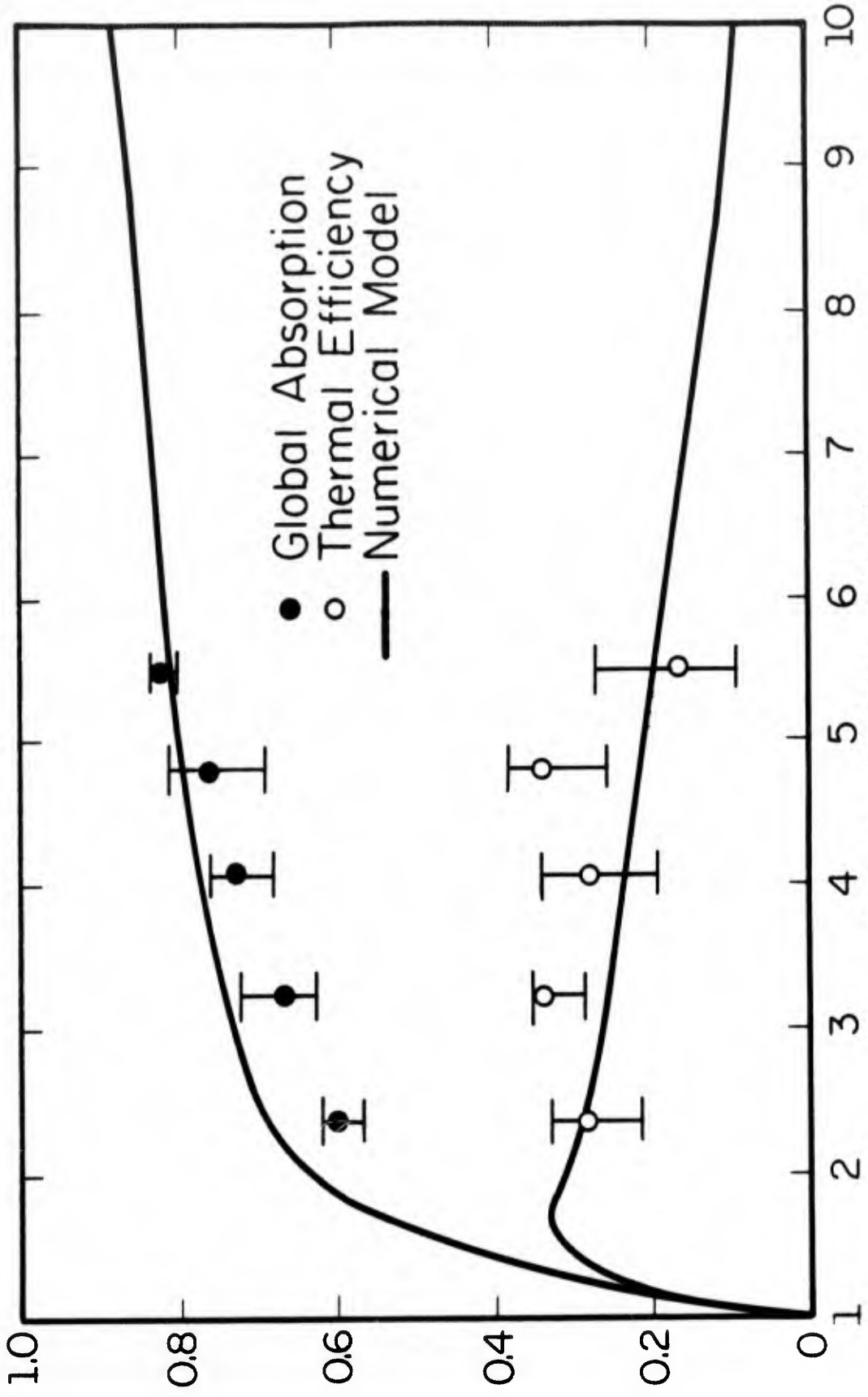

Figure 24: Global Laser Power Absorption as a Function of Laser Power: Pure Argon, f/2.4, 15 cm/sec

The 4 percent error was the worst case and was applied uniformly to the field resulting in conservative error limits. The trend of the data matches that of the model predictions, nearly within experimental error.

The thermal efficiency data is scattered but is of the same order as the model predictions. The calculations of the radiative losses are a volumetric effect and the error of the two measured spatial dimensions is additive. A ±10 percent error in radial and axial dimensions (±0.03 mm) significantly alters the radiative calculations, although it has little effect on global power absorption. Thus the efficiency calculations are used qualitatively in this investigation to check against second-law violations. Future efforts may need to employ resolution targets to more accurately measure plasma spatial extent. It should be noted that agreement between the spectroscopic data and the numerical model was not unexpected. Both algorithms utilize the same thermophysical property data, albeit in different formats.

The true consistency check of the spectroscopic data was made by comparison with independent measurement data. The calorimeter (Figure 16) was used to measure transmitted power from which global absorption could be determined. The thermocouples were used to determine the downstream enthalpy flux from which thermal efficiency could be determined. A comparison of the three techniques is shown in Figure 25. The calorimeter and spectroscopic data agrees marginally which may, in part, be due to radiative loading of the thermocouples and lead wires. However, the results indicate that the spectroscopic data can be reliably used in the calculation of laser power absorption, independently of other diagnostics.

The next set of experiments deals with flow-rate dependence of LSP. As the flow-rate is increased the plasma is elongated into the downstream, and

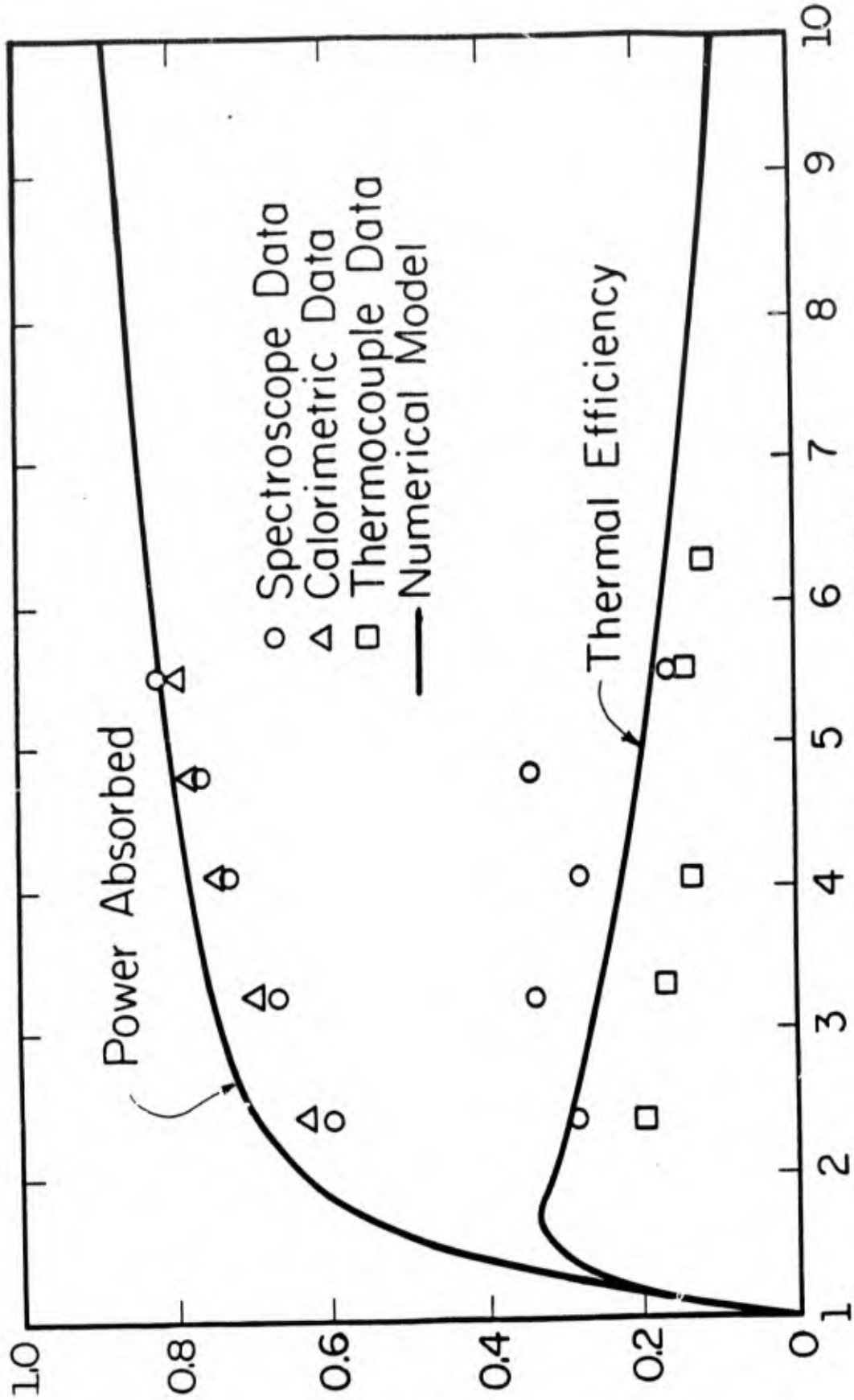

Figure 25: Comparison of Spectroscopically Determined Parameters with Calorimetry and Thermometry Data

the plasma front approaches the focus of the laser. Figure 26 is a comparison of the global absorption and thermal efficiency data at flow rates of 15, 60, and 120 cm/s at 5.5 kW. One sees that the net power absorbed decreases with increasing flow rate. From the spectroscopic data the overall plasma temperature decreases, offsetting any gains in absorption length at higher laser powers. The thermal efficiency data indicates that there may be an optimal flow velocity for a given power and beam geometry. As the flow rate increases, the lowered plasma temperatures result in decreased radiative losses. The effect overwhelms the slower trend of decreasing absorption, resulting in increased efficiency. The trend continues until a low enough plasma temperature is reached such that the reduction in power absorption overwhelms the nominal radiative losses. The above trends were seen to occur at 4.1 and 2.4 kW to a similar extent.

The pure gas plasma studies are some of the first treatments of CW laser-sustained plasma at powers up to 10 kW. At the onset of the program initiation was thought to be a problem due to the high intensities required for breakdown of a room temperature gas. The problem was circumvented by the use of tungsten targets as a source of the initial electrons required for breakdown at laser intensities below 10^7 W/cm^2. The technique was proven to be reliable and is relatively simple with respect to the hardware and controls necessary for arc discharge pre-ionization.

Plasma maintenance and stability have been shown to be independent of typical laser and flowfield fluctuations. The effects will certainly become increasingly critical at higher flow rates but to date have not been shown to be deleterious [4,11,12]. Radiative losses to the chamber walls is a concern, but engineering solutions such as reflective walls or regenerative preheating of the propellant have been proposed as part of the future research program.

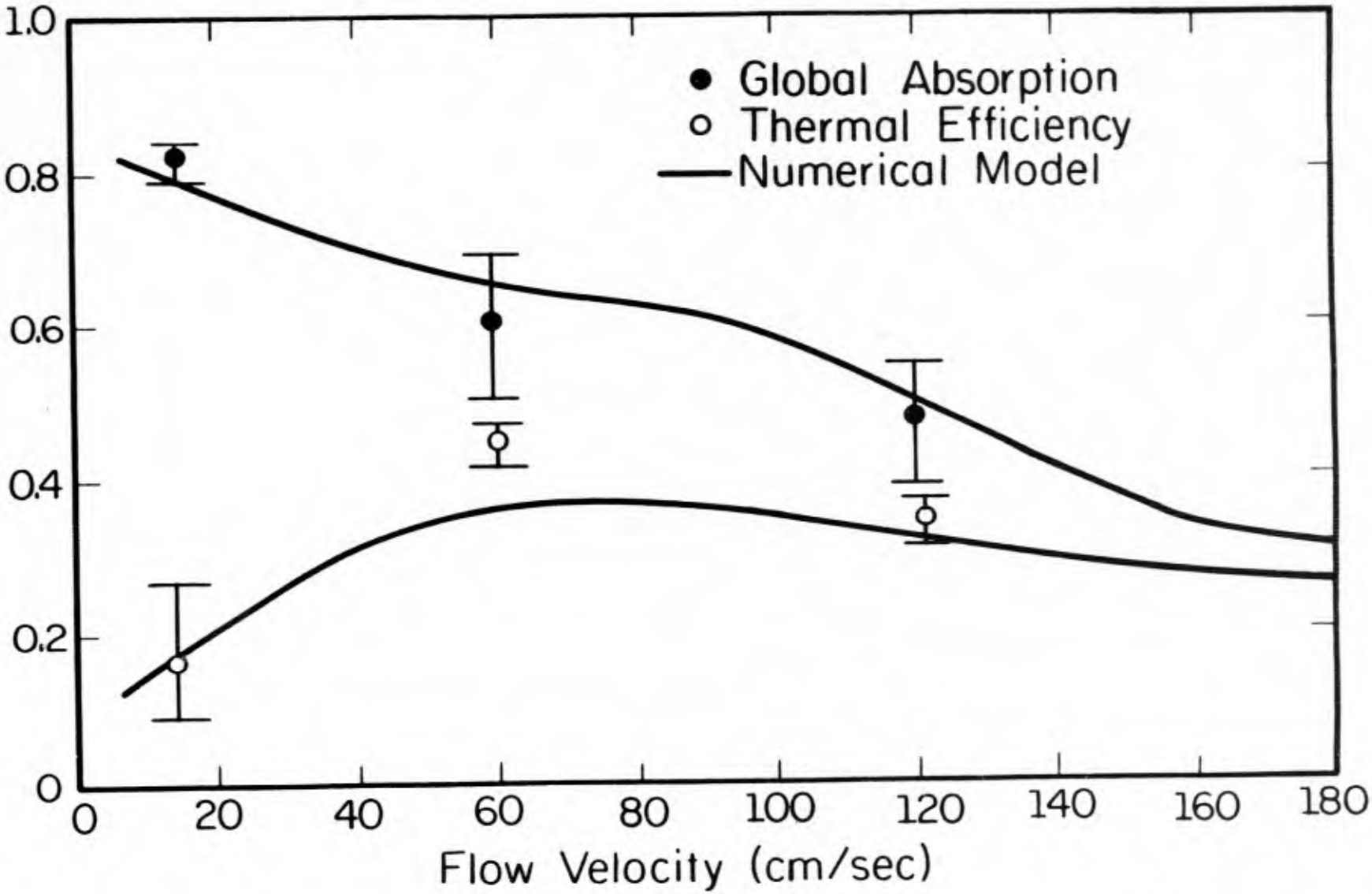

Figure 26: Comparisons of 5.5 kW Spectroscopic Data to a Numerical Model [4,5] at 5 kW as a Function of Flow Velocity: Pure Argon

The argon systems have demonstrated the promise of laser propulsion in that no fatal flaws have been found in the concept to date. The immediate research effort is designed at minimizing radiative losses. High f/# optical systems to reduce the radiating plasma volume have been shown to be theoretically feasible [4]. The apparatus for f/4 to f/8 beam geometries is currently being implemented. The hardware has been fabricated and demonstrated for splitting the laser beam in two equal halves. The goal is that multiple plasma formation will permit two smaller plasmas to operate more efficiently than one single plasma at twice the laser power. The lower power plasmas operate more efficiently due to lower radiative losses. The radiative view factor between plasmas may also reduce plasma radiation losses. Preliminary spectroscopic results for twin plasmas are discussed in the next section.

3.5 Preliminary Twin Plasma Results

Twin plasmas have been initiated and sustained adjacent to one another within the PIFC using the optical system shown in Figure 12. The procedure used for the spectroscopic measurements is basically the same except the plasma imaging optics must use a smaller magnification to scan the larger area of the twin plasmas.

The twin plasmas as an aggregate are not cylindrically symmetric, but are assumed to be as a first approximation, to permit the use of the Abel inversion discussed earlier. In addition, at any given z-location the temperature between the plasmas is assumed constant and equal to the peak plasma core temperature at that z-location. The first assumption tends to lower the calculated plasma temperature while the latter assumption tends to enlarge the

high temperature zone. The latter assumption appears reasonable in the region downstream of the focus due to gas mixing, but is less realistic between the plasmas, near the foci.

Based on these assumptions, a preliminary twin plasma case with a 12 mm focus separation, 6 kW total input power and 100 cm/s mean flow velocity has been analyzed. Temperatures of up to 16000 K have been calculated with a corresponding 80.3% global absorption and 20.5% thermal efficiency. The calculated efficiency is very near the 18% value determined by an independent technique based upon the measured exhaust gas temperature (see Section 5.2). Although this result looks promising, we feel a new inversion technique will be necessary at other operating conditions because of the erors introduced by the original assumptions.

3.6 Concluding Remarks

The two-dimensional spectroscopic data represent one of the first reports in which independent diagnostics were utilized as continuity checks. This also indirectly confirms the validity of the assumption of local thermodynamic equilibrium within the plasma core. LTE was the basis of nearly all data reduction schemes and analysis techniques. Laser propulsion has been shown to be promising with thermal efficiencies approaching 22 percent and up to 75 percent of the laser power absorbed. It is felt that thermal efficiencies of 50 percent will be necessary in realistic propulsion systems. In lieu of full scale laser systems on the order of megawatts, the research effort must require further mapping the laboratory domain of laser beam geometry, flow velocity, and pressure.

SECTION 4: LASER-INDUCED FLUORESCENCE STUDIES

4.1 Purpose

As will be discussed in the next section, overall thermal efficiencies have been measured using temperature mappings produced by a grid of thermocouples as well as by measuring the gas temperature in one of the exhaust ports. These measurements tend to be subject to experimental errors because the temperature mappings are not instantaneous, and because flow velocities are not known. As part of the ongoing laser propulsion research, we are currently attempting to improve the accuracy of the thermal efficiency measurements by using planar laser-induced fluorescence (LIF) techniques. Basically stated, LIF is a diagnostic technique in which a low-power laser is tuned to excite an electronic transition within an atom (either argon or a seed atom). When this excited state decays to ground, the intensity of the fluorescent emission can be used to determine either the concentration or temperature of the atom. By using a planar laser sheet to excite the seed, a two-dimensional mapping of either quantity can be obtained instantaneously.

An LIF diagnostic system has been developed that will eventually be used to make highly accurate measurements of LSP thermal efficiencies. The LIF system will be used to construct instantaneous temperature and velocity mappings in the downstream mixing region, which can then be used to calculate exhaust enthalpies with great accuracy. Unlike thermocouple measurements, LIF techniques are nonintrusive are unaffected by transmitted laser energy and plasma heating, and allow independent measurements of flow velocities for use in the efficiency calculations. In addition, because the measurements are instantaneous, the problems inherent in time-averaged thermocouple

measurements are avoided. LIF temperature measurements have never before been attempted in laser-sustained plasmas.

In addition to being needed for the efficiency calculations, the velocity mappings can be used to better evaluate flow patterns near the plasma, to determine if the flowfield is indeed one-dimensional in nature, and to see if any bouyant flow recirculation is occurring. The measurement of flow velocities in the flowfield near an LSP has never before been attempted.

Because of the complexity of LIF diagnostics and the time required to set up such a system, actual measurements within the plasma chamber have not as yet been made. Instead, the purpose of this chapter is to fully define the LIF techniques which will eventually be used in the plasma chamber for temperature and concentration measurements, and to describe in detail the LIF diagnostic equipment and how it will be used. In addition, there is a full discussion of some of the problems that may be encountered near the laser-sustained plasma, as well as some of the problems that have already been encountered in setting up the system. Finally, an organized program of future LIF studies is proposed and discussed.

For use in measuring efficiencies in the plasma chamber, two different types of LIF techniques will be used, both of which will make use of seed particles injected into the argon flow. The first type of measurement is used to detect the concentration of the seed particles. These concentration mappings can then be used to study flow patterns near the plasma, and to estimate flow velocities in the downstream region where velocity profiles are needed to calculate the thermal efficiency. Specifically, this is done by introducing the seed into the argon flow, and following the progress of the seed as it moves downstream, entrained in the argon flow. This LIF technique

involves measuring the absolute intensity of a single fluorescent line, and is known as a single-line LIF method.

The second type of technique will be used to measure temperatures, and can be used to produce complete and instantaneous temperature mappings of the downstream flowfield. These mappings can then be used for two purposes. Most importantly, the temperatures are needed for accurate efficiency measurements. In addition, as shown in Figure 27, it may be possible to bridge the temperature gap between thermocouple measurements and OMA spectroscopic measurements. This type of LIF technique involves measuring the ratio of two fluorescent emission intensities, and is known as a two-line LIF technique.

Section 4.2 discusses these two techniques in detail, outlining LIF theory and describing past research efforts. Section 4.3 describes the special conditions of our experiments, and explains specifically what seeds and transitions have been selected, as well as the peculiarities and limitations of each. Section 4.4 describes the tunable excimer/dye laser system used to excite the transitions. Section 4.5 covers the fluorescent detection system, which is the same OMA system used in the spectroscopic studies, with a few modifications. Section 4.6 outlines the flow system used to inject the seed particles into the gas flow. Finally, Section 4.7 summarizes the progress made to date, presents a detailed program of proposed LIF studies, and discusses potential problems and possible solutions.

4.2 LIF Theory and Previous Investigators

Laser-induced fluorescence was first developed as an outgrowth of spectroscopic diagnostics in the late 1970's, and was made possible by the new

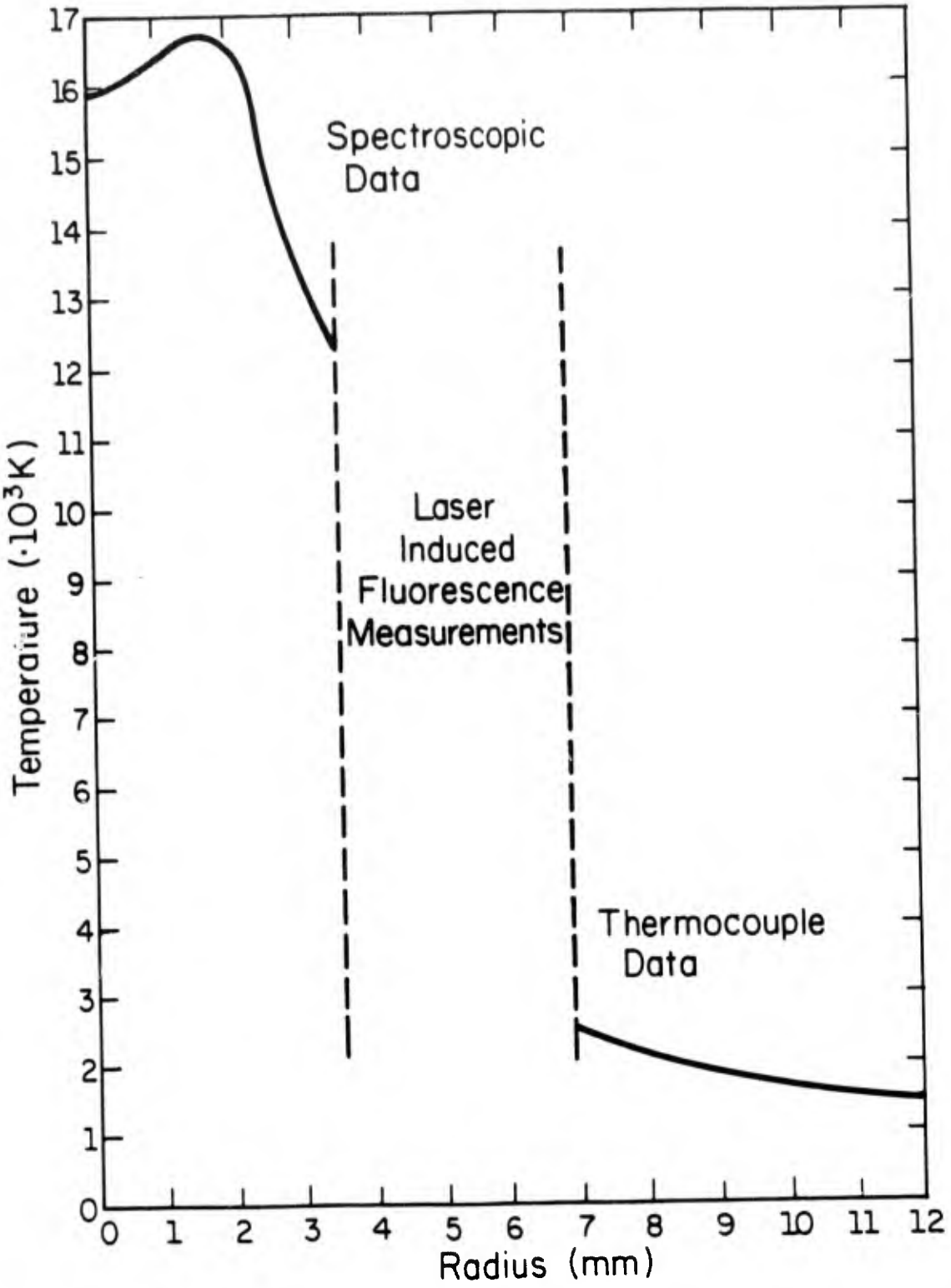

Figure 27: Comparison of thermocouple and spectroscopic temperature measurements. The two measurements are seen to be consistent with each other, but reveal a small gap where temperatures cannot be measured; LIF will be used in this temperature range.

availability of inexpensive tunable laser systems. The primary application for LIF systems has been in the combustion field, where the techniques have been used to accurately map temperatures and species concentrations in flames.

The earliest application for LIF was in the measurement of species concentrations in flames. For this type of work, single-line LIF techniques were used. The theory behind such single-line LIF techniques is illustrated in Figure 28. The molecule (or seed particle) of interest is excited by a tunable laser tuned to the wavelength of a specific electronic energy transition of the molecule ($E_L = E_2 - E_1$). If the intensity of the tuned laser is high enough, state E_2 becomes well-populated.

The excited atoms tend to decay quickly, and the intensity of the resultant single-wavelength fluorescent emission (S_{f1}) is recorded by a sensitive detection system. Then, as indicated in the equation in Figure 28, the concentration is determined through an explicit relation, where Q is the collisional quenching rate, A and B are the emission and absorption coefficients, N_f is the fraction of the seed population that is activated, and η is the collection efficiency of the detection system [25].

Such single-line LIF techniques have been used to measure the species concentrations of numerous molecules. Most of the attention has focused on the OH radical due to its importance in combustion processes. Much of this work has been limited to either single-point measurements in flames (ie., focusing the laser to a point in the flame and measuring concentration at that point only), or to line measurements across the radius of the flame, such as was done by Alden [26]. Single-point measurements have also been successfully conducted in CN, NH, NO, and CH by Morley [27] and by Vanderhoff [28].

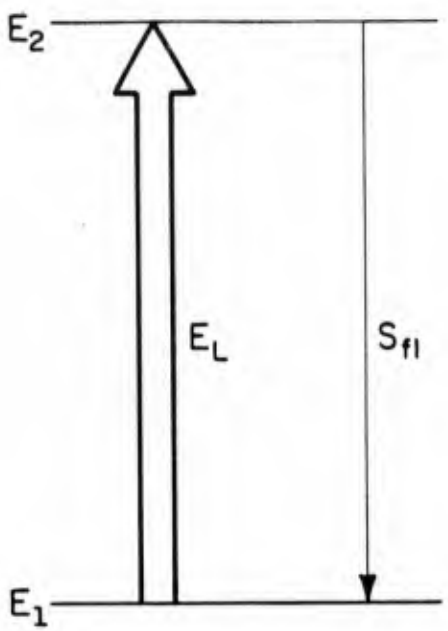

$$n = \frac{Q_{21}}{\eta\, A_{21}\, B_{12}\, N_f}\ \frac{S_{fl}}{E_L}$$

Figure 28: Seed concentrations can be measured using Single-Line LIF, in which the intensity of the fluorescent emission is used to calculate the concentration.

Measurements of concentrations within high temperature plasmas have also been attempted [29].

Most of the more recent LIF work has been of the planar variety, in which a planar laser sheet is passed through the flame, and a detection system oriented perpendicular to the sheet simultaneously records the species concentration at every point in the sheet. Such an approach has been made possible by the availability of lasers with higher pulse energies.

Because planar LIF reveals a great deal about the structure of flames and their flow patterns, other investigators have mapped OH concentrations for the specific purpose of flow visualization. Both Cattolica [25] and Kychakoff [30] have used LIF excitation of OH radicals to study combustion flow patterns. In addition, Dyer [31] has developed a system in which the detection system records two images of the flame on either half of the detector face, each image being recorded a short time apart. This permits the study of transient flow behavior. In addition, as will be discussed shortly, the two images (if recorded simultaneously) can be used to determine species temperature.

Other investigators have expanded on this approach by studying flow patterns using seed atoms artificially injected into the flow. Rapagnani [32] used such a technique for a study of flow patterns inside a chemical laser cavity. Molecules of iodine were used as the seed particle, and were seeded into the flow by passing air through a vessel containing iodine metal; the cold vapor pressure was enough to provide a sufficient seed concentration. More recently, Kychakoff [33] has demonstrated the feasibility of using a gaseous seed, NO. This greatly simplifies seedant introduction and calculations of seed concentrations.

Unfortunately, none of these techniques are adequate for use in examining flow patterns (or in measuring flow velocities) in the plasma chamber. The main reason for this is that we wish to use a technique that is applicable throughout the downstream flowfield, where temperatures can exceed 4000 K. At these temperatures, all of the molecules discussed so far will be dissociated, and therefore useless. Furthermore, even in regions of the chamber where temperatures are lower (such as near the exit plane), a large fraction of the seed particles will have already passed through or near the plasma, and there is no guarantee that these molecules will recombine correctly after leaving the plasma.

For these reasons, we have decided to use techniques that use atomic seedants such as indium and gallium. These materials, being monatomic, have the important advantage of not dissociating at high temperatures, and thus they should be useful at temperatures up to their ionization temperature (typically about 7000 K).

Concentrations of the seed atoms will be determined using a single-line technique, identical to those discussed above for molecular materials. Details of the types of seeds used, and the transitions selected for LIF, are discussed in Section 4.3. The seed concentrations will be mapped over time to study flow patterns inside the plasma chamber, and from these, flowfield velocities will be estimated for use in the efficiency calculations. It should be noted that it is not really necessary to be able to determine the seed concentration in absolute terms; rather, all that is needed is the ability to detect relative concentrations of seed particles embedded in the argon flow. From these, by following the progress of the seed atoms as they

flow downstream, it is possible to estimate flow patterns and velocity distributions.

LIF techniques have also recently been used to measure temperatures in combustion processes. For this type of measurement, new LIF techniques had to be developed, techniques that involve measuring the ratio of two distinct fluorescent emissions. Ratios of fluorescent emissions are used because the temperature can generally be written explicitly as a function of this ratio. These types of techniques are known as two-line LIF methods.

In this approach, two separate transitions of a three-level atomic (or molecular) system are excited using two distinct laser wavelengths, as indicated in Figure 29. The transitions used will normally share a common upper excited energy level, but will have different ground states. Also, to avoid problems with laser scattering, the detection system is usually tuned to record fluorescence from the emission line at the wavelength not being excited by the laser. Thus I_{31} is recorded while pumping L_{23}, and I_{32} is measured while pumping L_{13}. In this case, the two laser pulses must also be separated slightly in time.

Using the ratio of the two fluorescent emissions (I_{31} and I_{32}), the temperature can be determined using the equation shown in Figure 29. Here, L is the intensity of the pumping laser (used to normalize the fluorescent intensities), B is the stimulated reemission coefficient, and g is the degeneracy of the energy level. This two-line approach is more accurate than earlier single-wavelength LIF techniques for measuring temperature, because many extraneous factors cancel out, including seed density, line shapes, spectral distributions, and quenching rates. One important limitation of the approach is that the pumping laser must not be allowed to have an intensity

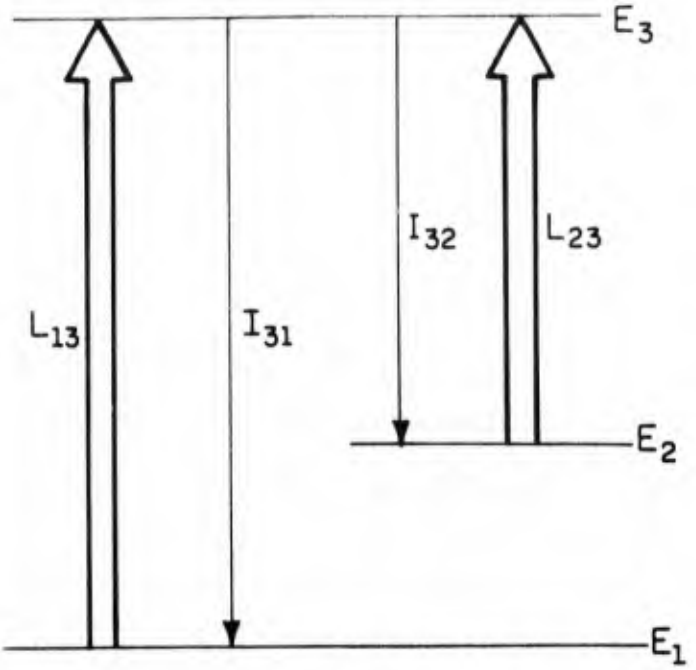

$$kT = \frac{E_2 - E_1}{\ell n\left[\frac{B_{23}\, g_2}{B_{13}\, g_1} \frac{(I_{31}/L_{13})}{(I_{32}/L_{23})}\right]}$$

Figure 29: In Two-Line LIF, two separate laser wavelengths are used to excite two different ground levels to the same excited state. The ratio of the fluorescent intensities can be used to calculate temperature.

high enough to cause saturation in the molecule, meaning that the more powerful laser sources must be attenuated, or must be loosely focused.

The two-line technique was first developed for OH systems by Cattolica [34]. Cattolica tested the new technique by measuring OH temperatures in a methane flame, and found good agreement with standard measurement techniques. A variation of this approach was developed by Gross [35], who used a two-line technique for NO molecules seeded into a turbulent supersonic flowfield.

As mentioned earlier, the two-line approach generally uses two transitions which share a common upper state, but have different ground states. Crosley [36] has shown that such transitions must be used to avoid temperature errors, because OH may not attain rotational equilibrium before it fluoresces. This equilibration is not necessary if two different ground states are used.

It should also be noted that the above methods measure the rotational temperature of the molecule. However, as has been shown by Zizak [37], the true translational temperature is nearly always equal to the measured temperature in atmospheric pressure flames. This may not be the case under other conditions, so this should be carefully considered in plasma chamber measurements.

There are two principal drawbacks to the two-line approaches discussed so far. Most importantly, all of the above techniques are useful only for molecular systems, and as was discussed earlier, these materials will probably be dissociated at the high temperatures found in the plasma chamber.

A second major problem is the requirement for two separate laser wavelengths. Although it is possible to generate two laser wavelengths using

our laser system (possible approaches are discussed at the end of this chapter), we would prefer to use an approach where only a single laser wavelength is needed.

Such a method was used by Alden [38] to measure temperatures in a methane flame. Instead of inducing fluorescence in a molecular seed, he used an atomic seed (indium) seeded into the air flow. Two fluorescent lines were excited in the indium (45.. and 410 nm), but instead of recording the emission from one line while pumping the other, Alven pumped only the 451 line while recording the fluorescence from both transitions. This was possible because scattering from the laser beam was negligible (presumably achieved through careful gating of the detector). It is not known for certain if Alden's approach is fully valid, though the agreement with other measurement techniques is very good.

Bradshaw used a similar two-line atomic fluorescence technique to measure temperatures in a low-temperature plasma [39]. The seed atom was again indium, but two separate lasers were used for pumping. Temperatures in this plasma did not exceed 3500 K, however.

In a review of atomic fluorescence temperature techniques, Bradshaw [40] has shown that the two-line technique for metals such as indium and thallium are valid, but he makes no mention of Alden's approach using only a single laser wavelength.

However, in the same study, Bradshaw also introduced a new type of two-line technique, known as thermally-assisted laser-induced fluorescence (TALIF). In this method, as illustrated in Figure 30, a single laser wavelength is used to excite a seed atom to a higher energy level (E_2). However, because some of the excited atoms will have collisions with nearby

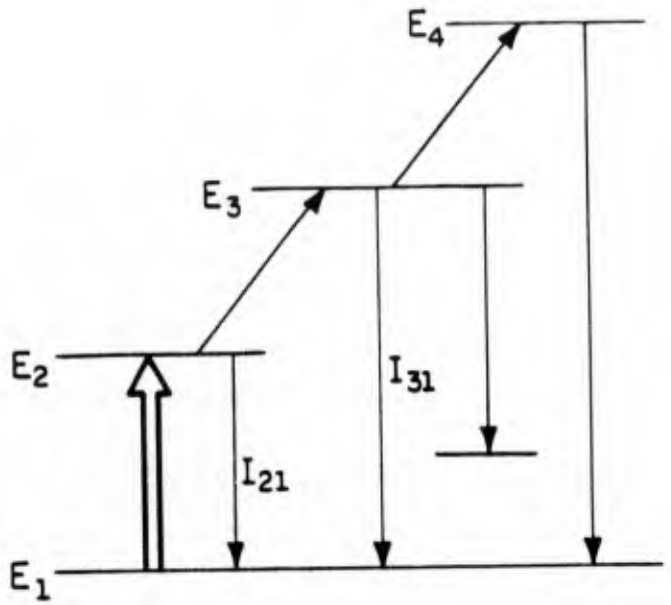

$$kT = \frac{E_2 - E_1}{\ell n\left[\frac{A_{31}\, g_3}{A_{21}\, g_2}\ \frac{\lambda_{21}}{\lambda_{31}}\ \frac{I_{21}}{I_{31}}\right]}$$

Figure 30: In Thermal-Assisted LIF, a single-wavelength laser can be used to determine temperature.

atoms, a finite fraction of the atoms in level E_2 will be further excited to level 3. When this state decays either to the ground state (I_{31}) or to an intermediate state, the ratio of the fluorescent emissions is used to calculate temperature, using the equation shown in Figure 30. Here, A is the spontaneous emission coefficient, and g is the degeneracy. Any combination of I_{21}, I_{31}, or any other fluorecent emission may be used to determine the temperature. It is also possible to use the flourescent emissions from state 4, which can become populated through thermal excitation of state 3. State 4 must be well populated for these latter lines to be used, however.

The TALIF technique has the key advantage of requiring only a single laser wavelength to measure temperature (so we can use our single-wavelength laser system), and the additional advantage of using atomic seedants (that will not dissociate in the plasma chamber). In addition, saturation is not needed but is acceptable, so we have the flexibility of using our laser for either point measurements or for planar measurements without being overly concerned about laser intensities. The main requirement is the selection of an atomic seed that has an energy level close enough to E_2 to be thermally populated during the laser pulse. Bradshaw also expresses concern that the laser pulse must be long enough to allow the higher energy levels time to become populated.

Zizak has used TALIF techniques to calculate temperatures in flames using indium and thallium [37]. His results not only demonstrate the feasibility of the technique, but have shown good agreement with other independent measurements. In addition, by calculating temperatures using more than one set of TALIF lines, he has been able to demonstrate consistency within the technique. Finally, Zizak has shown that the TALIF emission tends to reach

maximum fluorescent intensity about 1 ns after the laser pulse, suggesting that the concern of Bradshaw [40] is not relevant to laser systems having pulse widths greater than a few nanoseconds.

4.3 Current Activities

As discussed above, we plan to use two different types of LIF techniques in the plasma chamber. The first type is to be used for measurements of relative seed concentrations, so that we may study flowfield patterns and estimate flow velocities. The second technique is to be used for actual temperature measurements in the downstream flowfield, which will be used for more accurate measurements of LSP thermal efficiencies.

The special circumstances of the plasma chamber place unusual restrictions on the type of seed materials that may be used. Most importantly, the seed should be atomic, so that dissociation is not a problem. (Note that if the seed could be introduced downstream from the plasma, this requirement is unnecessary, as will be discussed in Section 4.7). The second restriction is that the seed material should not affect the laser-sustained plasma significantly. This means that the seeds should not be so easily ionized that significant numbers of additional free electrons would be released, artificially boosting the absorption and emission coefficients. This is one reason why sodium was never seriously considered as a seed candidate. Indium and gallium are not much better, but they do have somewhat higher ionization potentials.

For these reasons, we have tentatively selected indium as the seed candidate for LIF concentration and temperature measurements in the plasma

chamber. The feasibility of substituting gallium or thallium has simultaneously been explored, in the event indium proves unworkable.

For the concentration measurements, we will follow the approach of Rapagnani [32], who used iodine to study flow patterns in complex flowfields. The indium will be injected into the argon flow lines, and its progress through the chamber will be followed temporally. The indium will be excited at 410 nm, and the single LIF emission will be used to determine relative concentrations. As discussed earlier, it is not critical to precisely measure the concentrations; for this type of work, relative values are adequate.

For measurements of temperatures, indium will be used in the TALIF technique outlined in Figure 31a. Here, the indium is excited by laser pumping at 410 nm (the same as in the concentration measurements), and the fluorescent reemission at 410 nm will be used together with emission at either 326 nm or 304 nm (whichever is stronger) to determine temperature. It is also possible that the ratio of the 326 to 304 nm emissions can be used to calculate temperature without using the 410 nm reemission. Note that it is conceivable to measure both the concentration and temperature simultaneously (using the absolute magnitude of the 410 emission for concentration, and a ratio to determine temperature), but in practice this may prove difficult because faster frame rates are needed for the concentration measurements (so that velocities may be determined). Energy level diagrams for gallium and thallium are shown in Figures 31b and 31c.

Both of the LIF techniques will use planar laser excitation to produce complete two-dimensional mappings inside the plasma chamber. The laser will be introduced into the chamber by removing the thermocouple wire retract box,

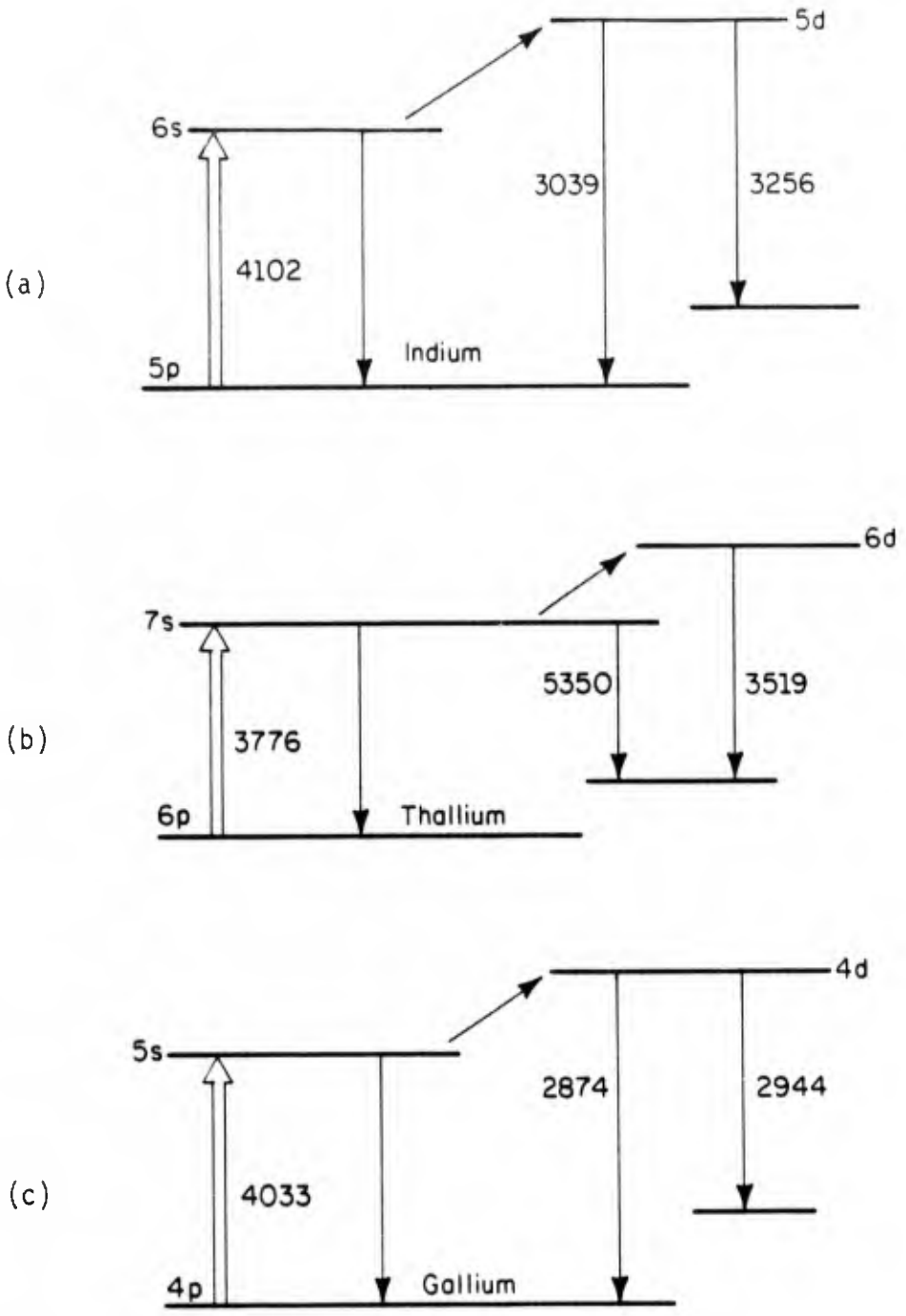

Figure 31: Thermal-Assisted LIF energy level diagrams for indium, thallium, and gallium. The large arrow indicates the transition we plan to pump, and other arrows represent the observable fluorescent emission wavelengths.

and installing an optical window over the thermocouple slot. A beam dump will also be needed inside the chamber to prevent reflections.

As will be discussed shortly, the OMA spectroscopic system will be used to record the fluorescent emissions, and to convert these into concentration and temperature mappings. Because the OMA system is not designed for such sophisticated data manipulation, the raw OMA data will be transferred to the HP 9000 system for data analysis. The entire LIF diagnostic system is presented graphically in Figure 32.

Having defined the techniques we ultimately wish to use in the plasma chamber, we are left with the problem of verifying the operation of both the experimental equipment and the LIF techniques. Obviously, it is necessary to start out by verifying the more basic techniques first, and progressing on to the more sophisticated techniques. Such a program of study is outlined in Section 4.7.

4.4 Seed Introduction Equipment

There are several possible techniques for introducing the seed particles into the gas flow. As discussed above, the two seeds that are of primary interest to us are indium and gallium, both of which are soft metals with low melting points. There are two widely used techniques for injecting these seeds (in atomic form) into a gas flow. These are: 1) aerosol injection of a soluble solution of the seed, and 2) passing the air flow through a heated liquid-metal pool, allowing the vapor pressure of the liquid metal to provide the needed atomic concentration.

This second approach has tentatively been selected for use in the LIF studies because of its simplicity. The complete seedant introduction system

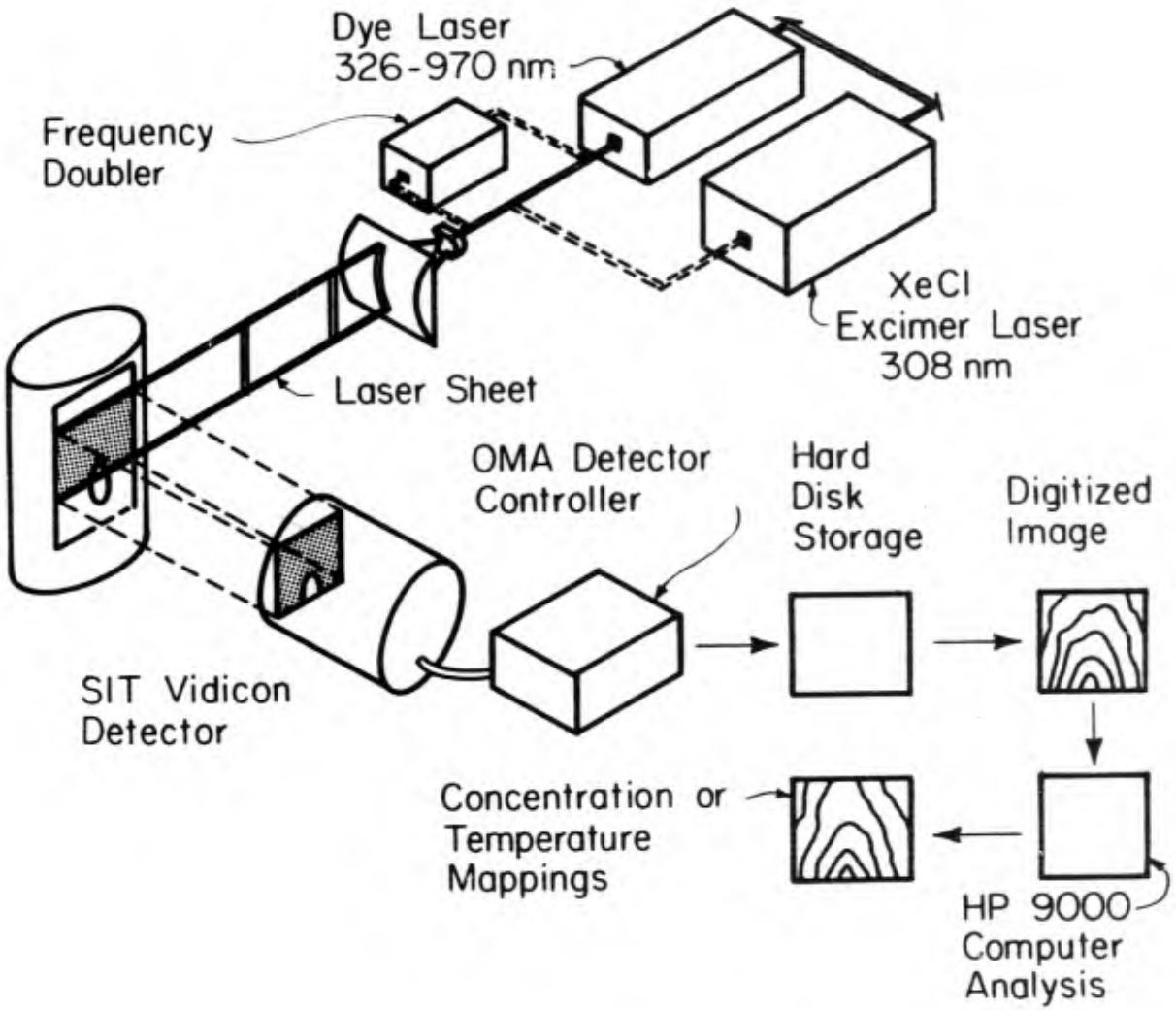

Figure 32: Components of the laser-induced fluorescence diagnostic system.

is diagrammed in Figure 33. As is seen, the metallic seed (either indium or gallium) is placed in the seed container and heated to a temperature just above its melting point (30 C for gallium, 157 C for indium). At this temperature, the vapor pressure should be high enough to provide an adequate concentration of seed atoms when the air is bubbled through it. At this time, there is no provision for measuring the seed concentration in the airflow.

The burner used in the experiments is a methane/air torch designed for hand welding applications. There are separate inlet lines for the two gases, and each has an individual regulator. Flow rates are typically 5 CFM air and 1 CFM (indicated) methane. The methane flowmeter is calibrated for air, so the true methane flow rate is not known. The flame is typically cone-shaped, about one centimeter across and four centimeters in height.

After the seeded air and methane are mixed in the burner, and combustion occurs, the exhaust gases are vented to the outside through dual 4.0-inch exhaust tubing, each of which is positively vented by a 100 CFM Muffin fan. The burner, seed container, flow lines, and OMA detector are all enclosed within a steel fume hood. This prevents toxic seed vapors from escaping into the lab, and keeps ambient light from interfering with fluorescence detection. Figure 34 is a photograph showing the hood, the methane burner, the seed introduction system, the focusing optics for the laser, and the gated OMA detection system.

Initial tests of the seed system have suggested that the indium concentrations produced by the liquid metal pool may be inadequate. This conclusion is based on our inability to resolve the emission spectrum of the metallic atoms in the flame. It is not yet known if this necessarily means that the concentrations are too low for LIF to be successful, but attention is now

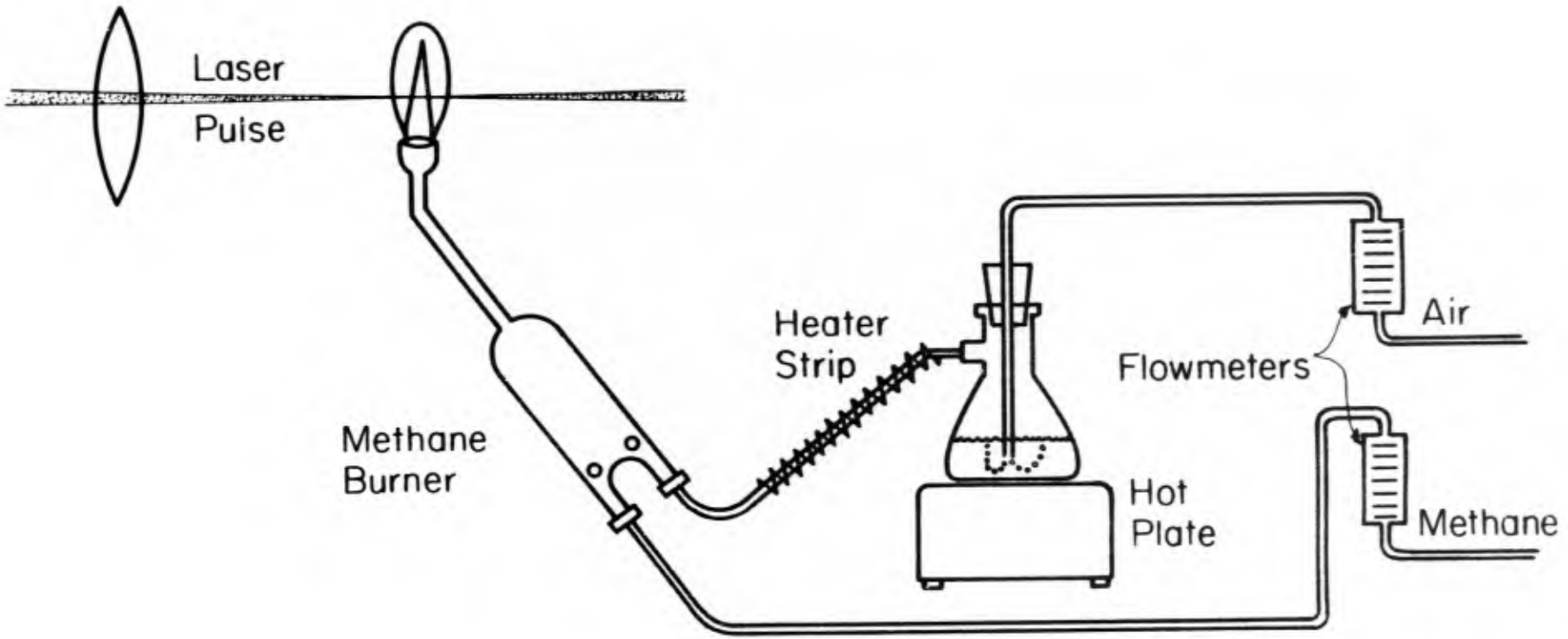

Figure 33: System used to introduce indium and gallium seed atoms into the burner air flow. The optics used for the line data acquisition mode are also shown.

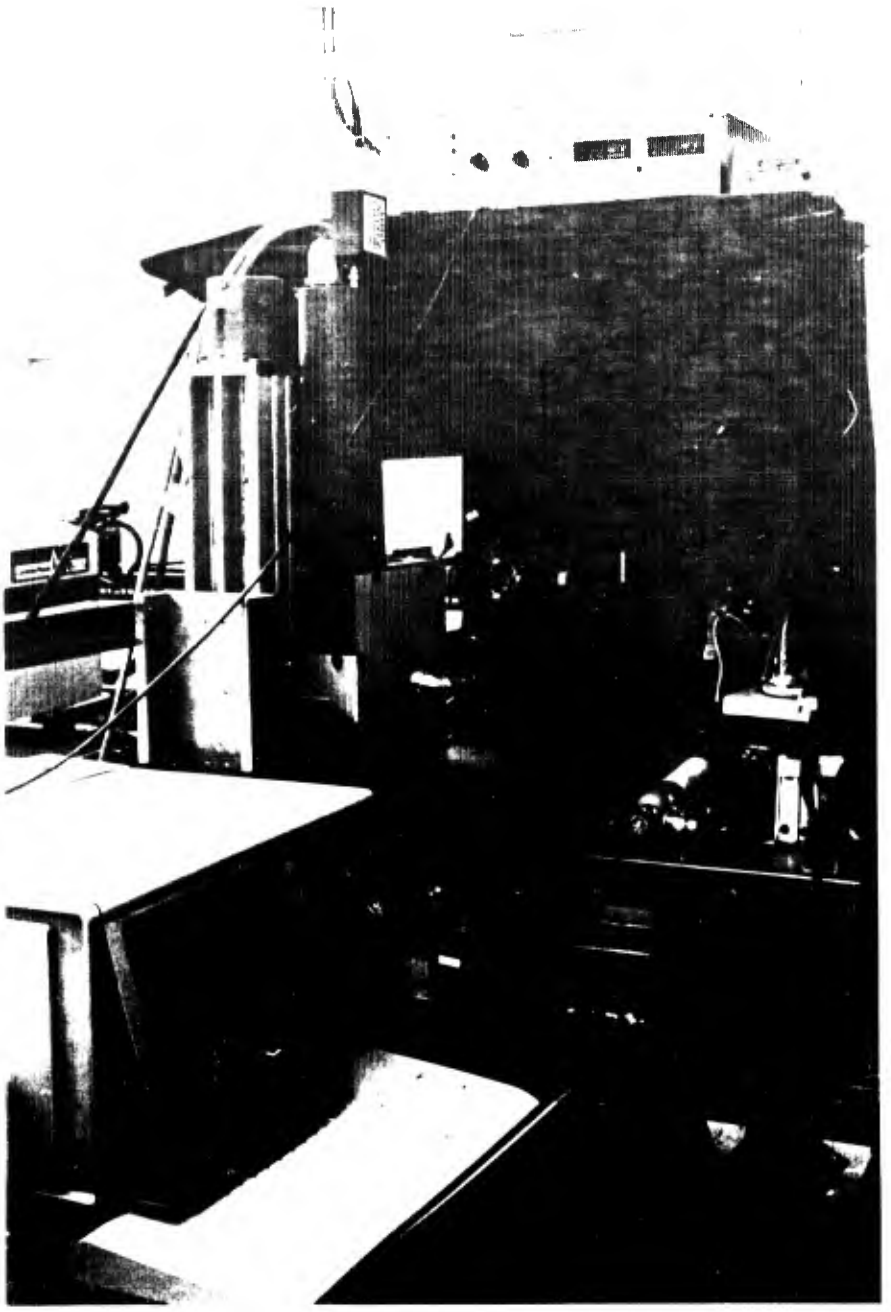

Figure 34: Photograph of the fume hood, seed system, laser optics, and gated OMA spectroscopic system.

being given to the use of an aerosol nebulizer in place of the liquid metal pool. Such a nebulizer would be used to inject fine droplets of a solution of seed atoms into the airflow. These nebulizers have been successfully used in several previous LIF studies.

4.5 Excimer/Dye Laser System

The laser system used to excite the transitions in the seed atoms is an excimer/dye tunable laser system. The system consists of a 100 W pulsed excimer laser used as a XeCl pumping source (308 nm) and a tunable dye laser capable of pulsed output in the complete range of 970 to 326 nm (down to 163 nm when the output is frequency doubled).

Both lasers, as well as most of the optics, are mounted on a 4.0 x 8.0 foot Oriel optical table. The beam output from the excimer laser (Lambda Physik Model 203 MSC) is rectangular in shape, 10 x 23 mm. Each pulse has an energy of 400 mJ with a pulse length of 25 ns. As discussed earlier, this pulse width should be adequate for TALIF applications. The maximum repetition rate of the laser is 250 Hz.

The UV output from the excimer laser is fed into the dye laser using two mirrors with high reflectance coatings. Careful alignment of this pump beam is crucial to obtain high efficiencies in the dye laser. The excimer beam is used as the pump source to induce fluorescence in a dye chemical inside the dye laser. This fluorescence is amplified and collimated inside the dye laser, and the output from the dye laser has a rectangularly-shaped profile roughly 0.5 by 1.0 mm.

The dye laser (Lambda Physik Model FL 2002) operates at an efficiency that depends on the selection of the dye, but in general is between 5 and 15

percent. This means that the dye laser output is roughly 56 mJ (for Rhodamin 6G, with an efficiency of 14%). Both the energy output from the dye laser, and the quality of the resultant beam profile can be optimized through adjustments of internal optics. This has proven to be a time-consuming process, complicated by the need to carefully align the two turning mirrors from the excimer pump beam.

The dye laser can be tuned over a limited range by varying the length of the resonator cavity within the laser, which is done using an externally-controlled stepper motor. Using this motor, the wavelength can usually only be varied a few hundred angstroms for a given dye. To cover the entire range of interest, a separate dye must be used for each portion of the spectrum. Changing the dye solution usually requires about a half day of effort, especially when dyes with different solvents are exchanged.

Originally, we had intended to use the dye known as Stilben 3, with a nominal emission range of 4120 to 4430 Å. The plan was to test two-line LIF in indium by exciting the transitions at 4510 and 4102 Å, as was done by Alden using the same dye [54]. Unfortunately, we discovered that the Stilben 3 emission virtually disappears at about 4150 Å, making this test impossible. Instead, we have recently switched to the dye DPS, which emits in the range 3990-4150 Å . This allows TALIF studies of both indium (at 4102 Å) and gallium (at 4033 Å). DPS has an efficiency of 11%, and the solvent for this dye (dioxane) is toxic and corrosive.

The output from the dye laser must be converted to a planar sheet for the planar LIF work being conducted. This is accomplished using the optics shown earlier in Figure 32. First, the laser passes through two cylindrical lenses, with focal lengths of 12.7 and 150 mm respectively. The purpose is to spread

one axis of the beam into a planar sheet. In addition, the lenses were designed so that the beam leaving the second lens is not quite parallel, but rather is still diverging slightly. This allows the planar sheet to expand to a width of 15 cm (the desired measurement width at the plasma chamber) after a distance of 3.7 m (the distance from the laser to the plasma chamber). This approach allows us to use smaller lenses and turning mirrors.

After the beam has been expanded into a sheet, a second set of optics (not shown) is used to reduce the thickness of the sheet from 0.5 mm to roughly 0.1 mm. Again, two cylindrical lenses are used for this purpose, with focal lengths of 25 and 150 mm. These lenses have not as yet been installed, because at this point beam intensity is not critical.

Figure 34 also shows one of the two turning mirrors which will be needed for work in Talbot Lab, when LIF is conducted in the plasma chamber. The optical table will be placed next to the plasma chamber, but is oriented so that the output from the dye laser must be reflected back across the top of the laser (using the two turning mirrors) to the access slot in the chamber. This is done to ensure a sufficient optical length for the diverging planar beam to fully expand to its 15 cm width. Also, the slow beam divergence helps retain planar beam uniformity inside the chamber.

The above optics are designed for use in the plasma chamber, but for the flame studies, a simpler optical system is adequate. Because most of the LIF scans to date have used the line data acquisition mode (discussed below), the emission from the dye laser is reflected into the fume hood using one of the turning mirrors. Here, the beam is focused to a point within the flame using a 21.1 cm focal length spherical lens. This lens was shown earlier in Figure 33. Because of the long focal length, the diameter of the focused beam is

relatively constant across the flame, providing a nearly uniform intensity distribution.

4.6 Fluorescent Emission Detection System

For both single and two-line LIF techniques, the LIF fluorescent signal is recorded using the same OMA spectroscopic system used in the spectroscopic plasma studies. For use in the LIF flame experiments, two different OMA data acquisition modes have been developed. A third mode, for use in temperature measurements in the plasma chamber, has been developed but not yet tested.

The first mode is the simplest, with the OMA operating in an identical manner as in the plasma spectroscopic mesurements. That is, the detector records a spectrum at each of twenty points along a horizontal line through the flame. At each point, the absolute intensity of a given line can be used to determine the seed concentration, and the ratio of two fluorescent lines can be used to determine temperature. To obtain a full 2-D mapping of both quantities, the detector is translated vertically, and numerous line scans combined into a single mapping. When using this mode, it is possible to use the long focal length spherical lens discussed in the previous section.

This approach works well in a steady-state flame, but in the complicated flow found in the plasma chamber, instantaneous mappings are preferred. For this reason, two other data acquisition modes have been developed; one for temperature mappings, and one for concentration mappings.

The concentration mappings will be produced by imaging the flame directly onto the face of the SIT detector, bypassing the monochromator. The optics used for this purpose is a single 15 cm focal length spherical lens. In

addition, a bandpass filter is needed to restrict the incoming light to the small portion of the spectrum centered at the fluorescent line to be recorded.

The result is a two-dimensional map of fluorescent emission from the flame. Once the intensities are adjusted to account for non-uniform detector response, the resultant map of intensities is directly proportional to seed concentration. If such maps are taken a short time apart, flow velocities can be estimated. The concentration mappings will eventually be transferred to the HP 9000 computer system for analysis and false-color plotting.

The final data acquisition mode is used to record a two-dimensional mapping of temperature. The approach used is similar to the one just discussed for concentration mappings, but because the ratio of intensities from two different fluorescent lines is needed, the flame image must be split into two. After being split by image-splitting optics, each image is positioned onto one half of the detector face, and the appropriate narrow-band filter is selected for the two fluorescent wavelengths that need to be recorded. This approach is similar to that used by Dyer to record time-resolved LIF emissions [31].

The result is a pair of images recorded at two different wavelengths, the intensities of which can be ratioed to determine temperature. Unfortunately, the OMA controller is not designed for such sophisticated data manipulation. This means that the data must be transmitted to an external computer system for analysis. In addition, the detector face must be calibrated to ensure uniform response. This final data acquisition mode has been designed, but has not as yet been installed or tested.

Detector Gating: The OMA spectroscopic system has the capability of being gated; that is, to record only the emission that strikes the detector

during a brief specified time interval, typically on the order of nanoseconds. Gating serves two important functions in LIF work. First, because the fluorescent emission is weak relative to the emission of the flame, gating allows the detector to be activated only during the brief time interval during which the fluorescent emission is strong (typically a fraction of a microsecond after the laser pulse has ended). This greatly improves the ratio of the fluorescent signal to the background flame signal. Secondly, because the gating can be programmed for variable delay times, it is possible to wait (with high temporal accuracy) until the laser pulse has ended before turning on the detector. This prevents any of the light from the laser from being inadvertently scattered or reflected into the detector. This is especially important when recording fluorescent emission at the same wavelength being pumped by the dye laser.

The gating function in the OMA system operates using a high-voltage pulsed power supply connected to the intensifier stage of the SIT detector. The high voltage pulse causes the intensifier to be active for only a brief time interval. The voltage of this pulse can be varied to achieve maximum detector response. The power supply is capable of gating the detector in a continuous range from 10 nanoseconds to 100 microseconds, with delay times of 0-100 ms. The power supply is fully compatible with the OMA microprocessor controller, and is programmed directly from the OMA console.

The control of the gated OMA is relatively straightforward. Once the gate width and delay time are specified, the OMA controller is activated and it performs a user-controlled number of detector prep scans to reduce dark background noise when the detector is activated. Following these, the OMA sends a 5 V TTL signal to the power supply of the excimer laser. The laser,

having been placed in the External Trigger mode, interprets the voltage as a signal to fire a single laser pulse, which is directed to the flame through the optics discussed earlier.

At the flame, a fiber-optic cable monitors the beam path, and responds when it sees that the pulse has been fired. The fiber-optic sensor then sends a TTL signal to the high-voltage pulse generator, which activates the detector. The OMA controller monitors this process, and can terminate the detector scan after a single frame has been recorded.

Although this gating system was used at first, it was later decided to remove the fiber optic detector because of an inherent 30-40 ns built-in delay time. This meant that the SIT vidicon was usually not turned on until 20-30 ns after the laser pulse ended, an unacceptably long interval. Instead, we are now using the synchronous output line from the laser power supply, routed to the OMA gated power supply. This output line sends a 12 V signal to the OMA when the laser pulse is fired, activating the detector immediately, with no delay other than that programmed by the OMA controller. The experiment is still initiated using the trigger on the OMA console.

The discussion so far has covered only the data acquisition mode for single laser pulses. In reality, the OMA system works best by operating in a data accumulation mode, in which the LIF emission from numerous laser pulses is summed. This tends to improve the signal-to-noise ratio significantly. The data accumulation is performed automatically by the OMA system. The operator simply allows the laser to continue pulsing, and the OMA sums the data automatically.

One question that is still being studied is how large the gating widths and delay times should be. It is currently believed that a gating width of

10-20 ns should provide the best signal-to-noise ratio, but the exact value can only be found by trial and error. Similarly, the delay time depends on the inherent delay in the laser trigger, and on the optical length from the laser to the flame. When recording fluorescence from an emission line different from the one being pumped by the laser, the delay time is not critical. However, when recording at the same wavelength as the laser, the delay time must be set to ensure that the OMA does not record data until after the laser pulse has ended, so that scattering can be eliminated.

A final useful feature of the OMA system is an option for dry-ice cooling of the 1254 SIT detector to reduce dark background noise. This would probably prove very useful in LIF experiments, where the signal-to-noise ratio is often marginal.

4.7 Research in Current Year Activities

The primary goal of the LIF work to date has been the setup of a workable system for the detection of LIF emissions, and the definition of LIF techniques that are usable in the high temperature regime of the plasma chamber. These goals have been accomplished. The next step is to prove that the equipment does in fact work, and that the LIF techniques are feasible.

The first major area of work is the alignment of the OMA detection system. This has already been accomplished, and has been used to map CH and OH radical emissions from the methane flame. The relative intensities of these emissions across the diameter of the flame are plotted in Figure 35, indicating that the CH emission is considerably stronger than that of OH, and suggesting that there may be some assymmetry in the flame. This question is still being explored, but it is likely that the assymetry occurs because

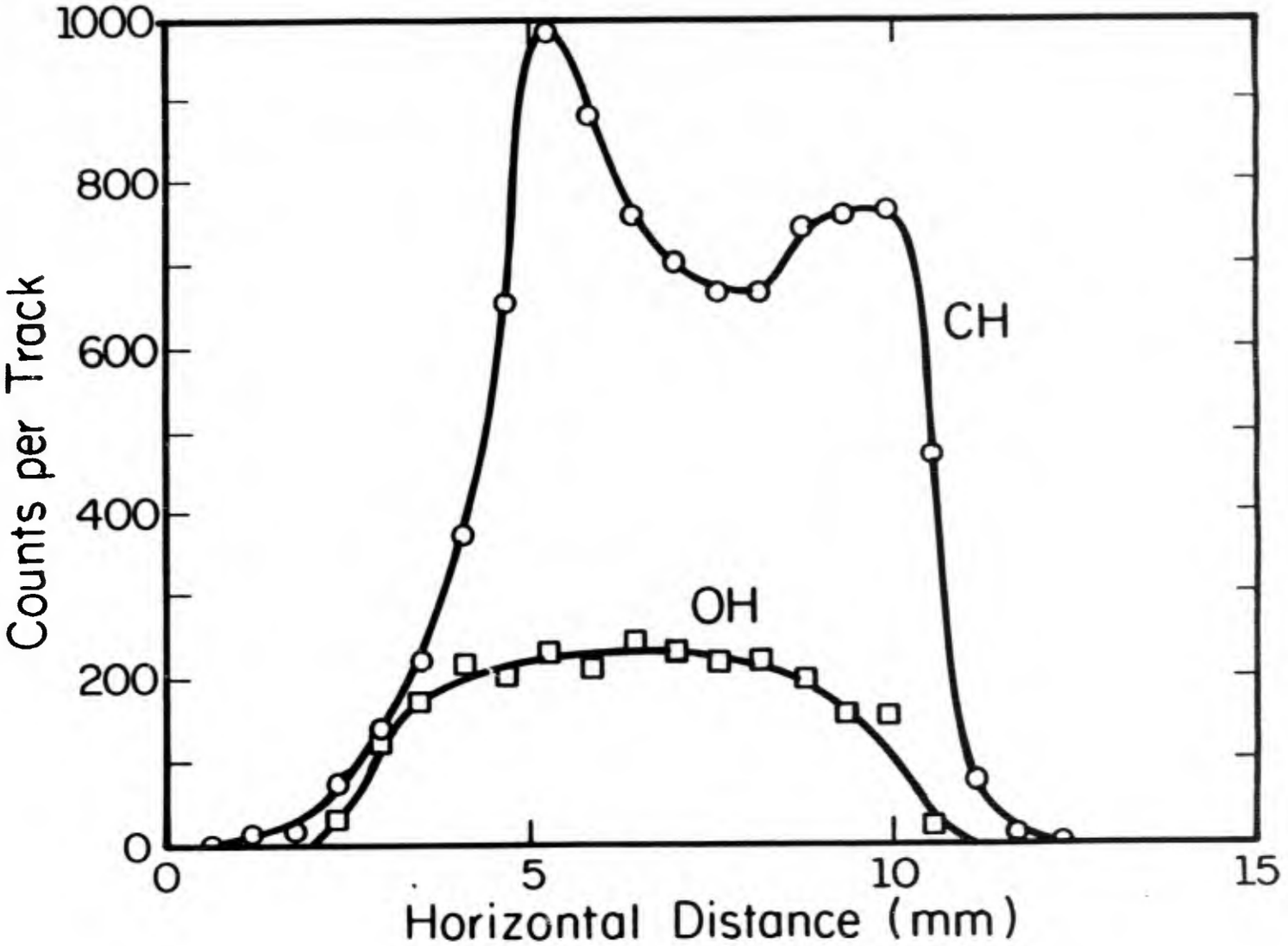

Figure 35: Relative intensity distributions of CH and OH emission from a methane flame, obtained using the OMA system in the line data acquisition mode. The data confirms the central dip in intensity seen visually, but may also indicate asymmetry across the flame diameter.

Figure 35 plots the peak value of the emission line, rather than the integrated area under the emission line. Our ability to resolve the OH emission also confirms that the OMA detector scintillator coating, which was damaged then repaired, is now functioning properly.

Using the OMA system, we are now in the process of conducting LIF concentration and temperature measurements in the methane flame through excitation of the OH radical. This is a logical first step for two reasons. First, LIF in OH is a very well documented technique, and there is a wealth of reported results against which our findings can be compared. Secondly, since seed introduction is unnecessary, it is possible to eliminate a major source of potential error.

The choice of the OH radical does present one complication. The excitation wavelength of OH is 306 nm, considerably below the minimum wavelength of the dye laser. To reach this transition, it is necessary to frequency-double the output of the dye laser. The frequency doubler has recently been installed.

Once the operation of the fluorescence and detection systems have been verified for OH, it will be possible to move on to metallic seeds, specifically indium and gallium. Before attempting TALIF, we would like to repeat the two-line temperature measurements of Alden [54] using indium seeds. At one point, we attempted to perform this test, but persistent problems with the gated power supply forced us at that time to operate in the CW mode, which reduced sensitivity considerably. Nevertheless, it was possible to detect very weak fluorescence at 4102 Å while pumping at 4510 Å , but the intensity was too small to be useful in calculations. And, as mentioned earlier, the laser dye proved to have too narrow a range to

reverse the excitation wavelength. Similar two-line measurements were attempted using gallium, but no detectable fluorescence was seen.

The final stage of the flame experiments will be the verification of the TALIF techniques in indium and gallium. At the same time, the complex data acquisition method for recording two-dimensional temperature distributions will be tested. At the conclusion of the flame studies, there will be a choice between moving the system to Talbot Lab for use in the plasma chamber, and conducting LIF measurements in argon plasmas formed above metal surfaces, using the 2 kW laser in the MEB lab.

The techniques discussed above will be used to map temperatures and flow velocities in the downstream portions of the plasma chamber. However, another type of LIF technique may be needed in regions closer to the plasma, where radiative emission by the plasma begins to interfere with the diagnostics. This interference can take two forms. First, as the LIF scans get closer to the plasma, the continuum emission from the plasma can overwhelm the relatively weak LIF emission. Line emissions from the plasma at 4044 Å could also a problem for the gallium seed (4033 Å). Secondly, a portion of the continuum emission from the plasma will be at the same wavelength as the tunable laser, meaning that the plasma will be inducing LIF in nearby seed atoms. Both of these problems are unavoidable when working near the plasma.

A related problem inherent to metallic seeds is that they are easily ionizable, and will therefore release additional free electrons as they are heated to high temperatures near the plasma. Unless the seed concentration is kept extremely small, the presence of the seed can cause changes in plasma behavior, absorption, and reradiation. Thus we will have changed the plasma we are attempting to study. It is not yet known what the maximum safe seed

concentration is, nor what minimum concentration will produce resolvable LIF fluorescence.

All of these problems could be avoided if LIF could be induced in a noble gas, particularly helium or even argon. Argon would be the ideal choice, since this would eliminate the need for any seed at all. Helium would also work well, because its ionization potential is higher than that of argon, so its presence would not cause the release of additional free electrons, and it should resist ionization in regions close to the plasma.

To test if LIF in argon or helium is possible, it will be necessary to tune the laser across the various possible transitions of the two gases to see if any fluorescence is visible. Of course, the gas would have to be heated, which may be accomplished by seeding the argon and helium into the methane flame. However, if higher temperatures are needed, verification must await testing in the plasma chamber.

The two most promising argon transitions appear to be the 6965 and 7067 Å Argon I lines. As was shown earlier in the LSP emission spectra, these lines are well separated from other argon lines. Also, the background continuum is fairly weak in this spectral range. To our knowledge, LIF excitation in noble gases has not been attempted before, and no literature exists to guide our studies.

Another possible LIF technique that could be explored is the use of NO to measure temperatures and study flow patterns in the plasma chamber. NO has the advantage of being easily seeded into the argon, and its concentration could be easily determined. And, as mentioned earlier, previous investigators have already proven its utility in flames. However, there is still the problem of seed dissociation near the high temperature plasma. This could

possibly be avoided by injecting the seed into the argon at some point downstream from the plasma, so that it does not pass through the high temperature region. Of course, there is no guarantee that the NO will not dissociate strictly from the high downstream gas temperatures, and this also raises the question of whether thermal equilibrium will exist between the NO and the argon.

As a final point, it should be noted that if true two-line LIF temperature measurements (using two separate laser excitation wavelengths) are ever needed, it may be possible to use the current laser system. Several approaches are possible. The excimer could be used as one source and the dye laser as a second, but seed atoms must be found which have one transition at 308 nm. Alternately, the dye output can be split into two beams, and one of these can be put through the frequency doubler to give two separate laser wavelengths. Again, it would be necessary to find a seed with appropriate transitions. Finally, it may be possible to rapidly modulate the output of the dye laser between two wavelengths, as suggested by Bradshaw [40].

SECTION 5: EFFICIENCIES BASED UPON THERMOCOUPLE DATA

The spectroscopic and theoretical studies discussed earlier indicate that for laser powers of 2-8 kW more than 80% of the laser energy can be absorbed by the plasma, and because such a large portion of the incident laser energy can be absorbed, laser propulsion appears promising. The key to the success of laser propulsion, however, is not only how much laser energy is absorbed, but how much energy is retained by the gas. The simple energy balance shown in Figure 36 indicates that the absorbed laser energy at steady-state is not all retained by the gas and that some is lost by both convective and radiative mechanisms. These losses can indeed be significant. Figures 6 and 7, shown earlier, indicate theoretical predictions of large radiative losses at constant, but different velocities as a function of laser power. It should be noted the model does not include any convective losses and therefore, in effect, assumes an adiabatic chamber wall. In our facility, however, we cannot assume an adiabatic wall and, indeed, data shown later in this section indicates that convective losses are measureable to a relative extent, although no absolute measurements are yet available.

These radiative and convective losses can be significantly reduced by incorporating regenerative techniques, but our facility currently lacks this capability. As a result, the measured thermal efficiencies discussed later in this section are somewhat lower than would be expected in an insulated or regenerative absorption chamber, because of both radiative and convective losses. We are planning to design an absorption chamber which either uses regeneration to regain this lost energy or uses insulated refractory walls to better maintain an adiabatic boundary.

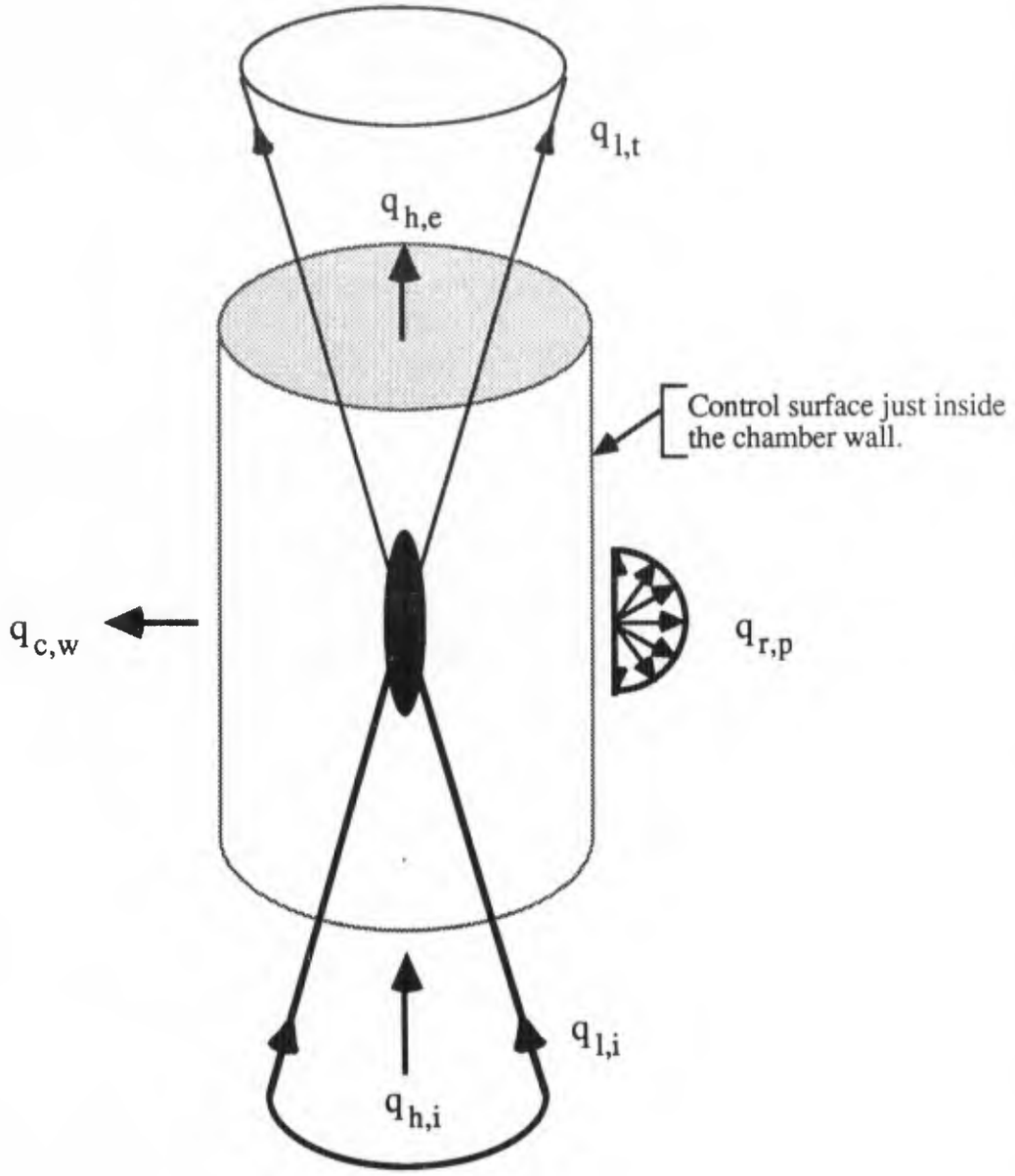

$$q_{h,i} + q_{l,i} - q_{c,w} - q_{h,e} - q_{l,t} - q_{r,p} = 0$$

where:

$q_{h,i}$ = inlet enthalpy flux, $q_{h,e}$ = exit enthalpy flux,

$q_{l,i}$ = input laser flux, $q_{l,t}$ = transmitted laser flux,

$q_{c,w}$ = wall convective flux, $q_{r,p}$ = plasma radiation loss.

Figure 36 Steady-state energy balance within the absorption chamber.

The thermal efficiencies discussed later in this section were measured entirely independently of the spectroscopic and calorimeter measurements discussed earlier. The thermal efficiency, η_{th}, as defined by Eq. 7 in Section 3.3, represents the percentage of input laser power retained by the gas, and is determined here by the ratio of the measured change in the working gas enthalpy flux to the measured laser power focused within the chamber, that is,

$$\eta_{th} = (100) \frac{\dot{\Delta H}}{P_{input}} \tag{8}$$

The change in enthalpy flux, $\dot{\Delta H}$, is given by

$$\dot{\Delta H} = \dot{m} C_p (\bar{T}_{exit} - \bar{T}_{inlet}) \tag{9}$$

where $\dot{m}$ is the mass flowrate, C_p is the specific heat of the working gas at constant pressure and $\bar{T}$ the mass averaged gas temperature. The greatest challenge in measuring the efficiency lies in determining the mass averaged exit gas temperature, because the input laser power is measured in a straightforward manner as outlined in Section 2.2, and the inlet gas temperature is uniform and known.

We have in the past used two separate methods of determining the mass averaged exit gas temperature. In the first method, the radial temperature distribution, measured downstream of the plasma, is integrated in a mixing cup analysis. This method, discussed in Section 5.1, is only approximate because of thermocouple errors associated with the adverse conditions within the absorption chamber as well as the use of a uniform mass flow assumption in the

mixing cup analysis. In the second method, discussed in Section 5.2, the exit gas temperature is measured by a thermocouple in one of the exhaust ports. This measurement assumes a well mixed gas which seems reasonable considering the flow geometry, but suffers from additional convective losses within the recirculation region of the calorimeter.

The first method was originally thought to be superior because it yielded thermal efficiencies comparable to the model; however, recent work has shown these early data indicated artificially high efficiencies because of thermocouple errors. In fact, after significantly reducing the thermocouple errors, the mixing cup analysis now results in calculated efficiencies substantially lower than those obtained using the measured exhaust port temperature. As a result, we now believe the assumption of uniform mass flow in the mixing cup analysis is inadequate and that the measurement of the exhaust port gas temperature is a better indication of the true mass averaged exit gas temperature, even though it suffers from the additional convective losses in the calorimeter.

5.1 Radial Temperature Profile Integration

The radial temperature distribution of the working gas downstream of the plasma is measured by an array of thermocouples mounted on an annular carriage and positioned perpendicular to the gas flow, as discussed in Section 2.4.4. The thermocouple array is monitored by a Fluke 2452 Computer System and, in theory, provides a means of measuring the initial transient, the time required to reach steady-state, the actual steady-state radial temperature distribution and any small-scale temperature fluctuations due to flowfield phenomena. The steady-state temperature profile is the most useful because knowing it permits

an approximate calculation of the mass averaged exit temperature by a mixing cup analysis. This calculation is only approximate because the true calculation requires knowledge of the axial velocity profile as well, for which we have no means of measuring at present. To complete the mixing cup analysis, we assume negligible radial and circumferential velocity components which simplifies the steady-state mass conservation equation to

$$\rho u = \text{constant} \tag{10}$$

where ρ is density and u is the axial velocity. This assumption simplifies the expression for the mass averaged exit temperature to

$$\bar{T}_{exit} = \frac{2}{R^2} \int_0^R T(r)\, r dr \tag{11}$$

where T(r) is the measured radial temperature profile and R is the chamber radius. The thermal efficiency can then be determined using the calculated $\bar{T}_{exit}$ with Eqs. (8) and (9).

Early results from this analysis seemed promising because the efficiencies matched the modeling results reasonably well, but there was still concern because of excessive scatter and lack of repeatability. These concerns led to a thorough examination of these temperature measurements and revealed significant errors as a result of the intense plasma radiation, the partially transmitted laser beam and the relatively low flow velocity. These errors will be discussed in the next section.

5.1.1 Carriage Thermocouple Errors

A thermocouple will only indicate its own temperature and it is the user's responsibility to ensure its temperature is acceptably close to that of the medium being measured [40,41]. In general, the steady-state temperature of a thermocouple is the result of equilibrium among the three modes of heat transfer between the probe and its surroundings. In this particular application, the temperature is dictated by the balancing of convective heat transfer between the gas and the thermocouple bead, the net radiative heat transfer between the bead and the plasma as well as the bead and the chamber wall, and the conductive heat transfer along the thermocouple leads. The problem of thermocouple errors is even more acute in this application because the low velocity gas flow results in a relatively low convective heat transfer rate contrasted by the highly radiative plasma. In addition, the radially oriented thermocouples are subjected to an appreciable energy flux over a small area as a result of the incident partially transmitted laser beam. Figure 37 shows the beam incident on the carriage thermocouples in a sectioned view of the chamber and Figure 38 shows the beam incident on several the thermocouples in a cross-section view, from just above the carriage.

In early measurements, including those reported in last year's report, temperatures measured by this technique were artificially high for at least two reasons. First, in some cases, thermocouple beads were inadvertently positioned directly in the profile of the laser beam and the laser irradiation heated the beads well above the gas temperature. The second reason was due to the partially transmitted beam striking several ceramic thermocouple sheaths. In these early runs, these ceramic sheaths were not shielded from the beam and this resulted in large conductive thermocouple errors. The

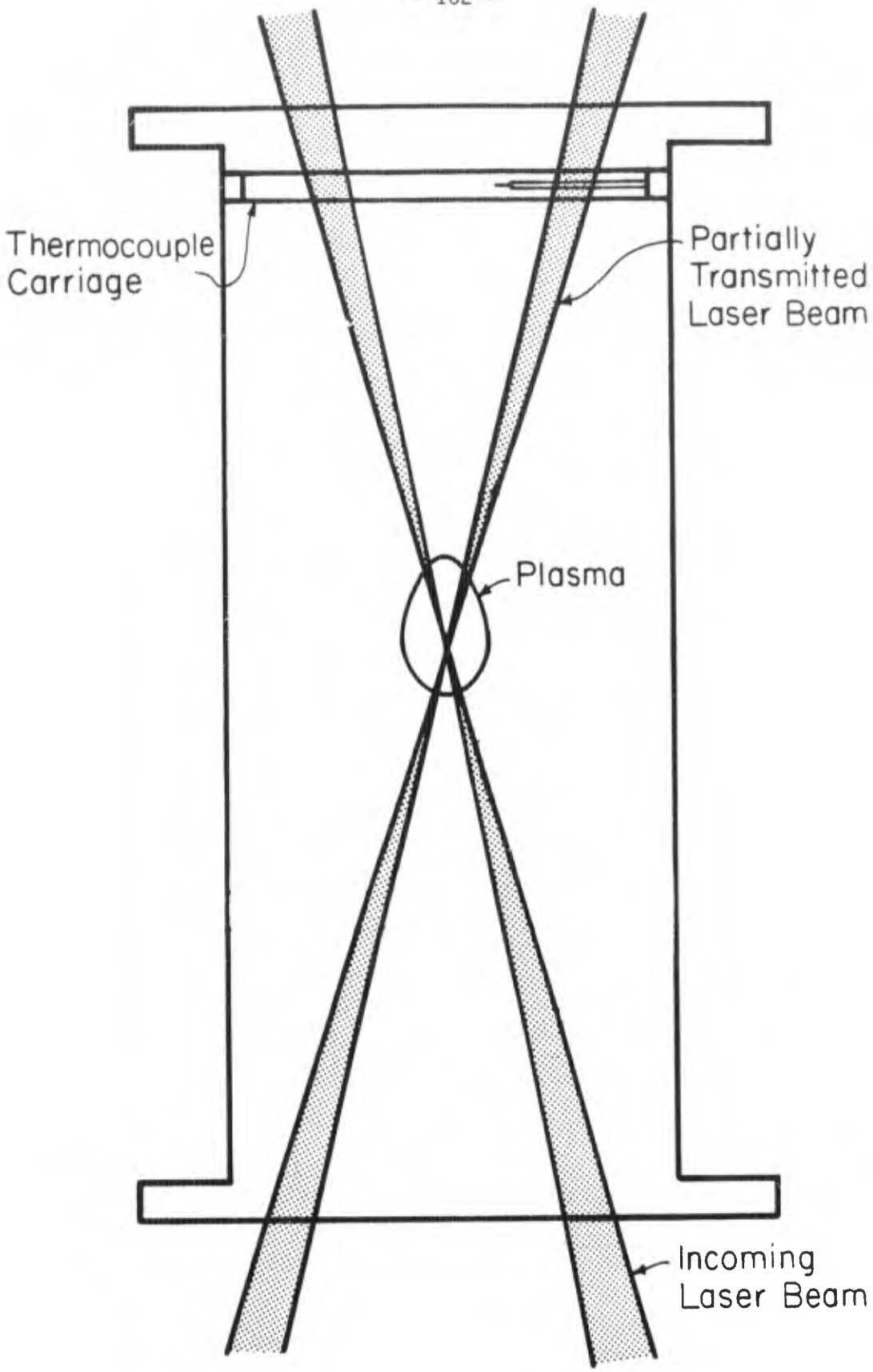

Figure 37: Sectioned view of the chamber showing the partially transmitted laser beam incident on a carriage thermocouple.

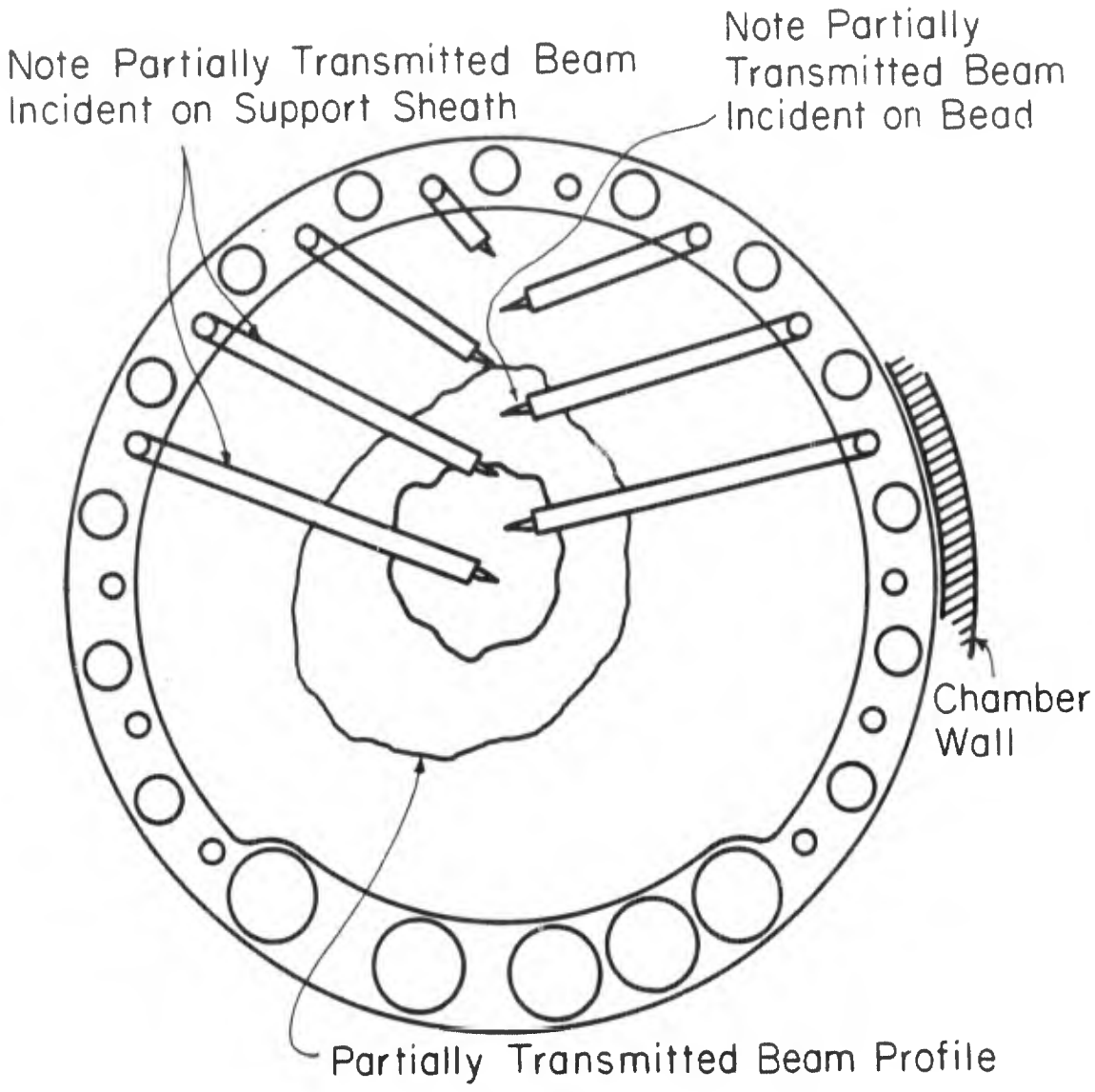

Figure 38: Axial view of the chamber showing partially transmitted laser beam incident on carriage thermocouples.

ceramic sheaths actually became much hotter than the gas because they absorbed a significant portion of the incident 10.6 μm irradiation, and subsequently, conductively heated the thermocouple leads. These two errors were only associated with the thermocouples in the path of the transmitted laser beam and were easily identified. A third reason for artificially high temperatures is still suspected but is not as easily verified or corrected. This suspected error is due to radiative heating of the thermocouple beads by the plasma and presumably affects all of the thermocouples to approximately the same extent.

5.1.2 Carriage Thermocouple Shields

The artificial thermocouple heating by the incident transmitted beam has been significantly reduced by placing two cylindrical copper shields over the ceramic sheaths. Copper was chosen because it can typically reflect as much as 98% of the incident 10.6 μm radiation and has proven to be a most effective shield material. The two shields act as radiation shields by design; a schematic of a shielded carriage thermocouple is shown in Figure 39. Each ceramic sheath is wrapped with a 0.010 inch thick copper sheet which is thermally insulated from the sheath by two thin ceramic washers. A second outer shield encloses the wrapped, ceramic sheath but is independently mounted on the carriage to thermally insulate it from the inner shield.

This shielding technique has proven quite effective and consistency as well as repeatability are excellent for relative short runs (less than 90 seconds). Longer run times give questionable results, because we have found the shield temperature approaches and can exceed the thermocouple temperature for some conditions. But at this point we feel the profile shapes are correct, even though the absolute temperatures are still uncertain, because

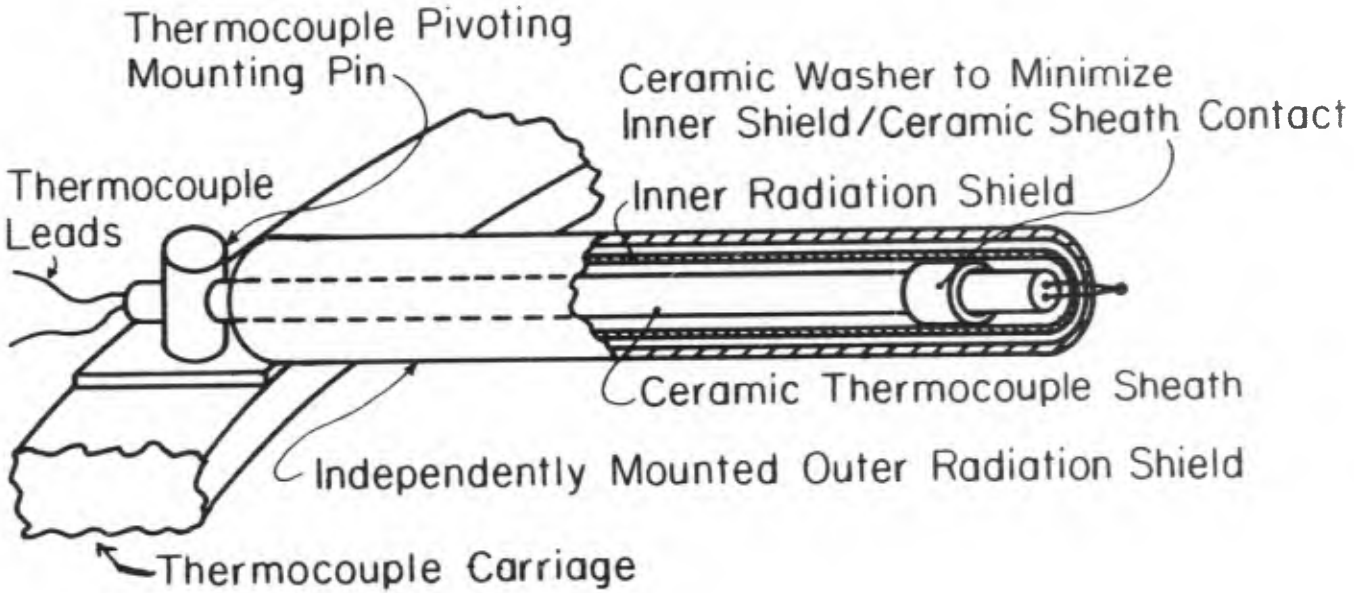

Figure 39: Cutaway view of a shielded carriage thermocouple. Note the double radiation shield over the ceramic sheath.

of the shield temperature variation as well as the question of plasma radiation errors. We are currently examining independent techniques for verifying these radial temperature profiles, including the use of an aspirated thermocouple probe (see Section 5.3) and a recently purchased thermocouple which features radiation shielding and a millisecond response time.

It should be noted here that we do not have any accurate single plasma downstream temperature profiles at this point, because of the errors discussed above; however, we do have some recent twin plasma temperature profiles which will be presented in the next section. In addition, we have found the mixing cup analysis results in calculated thermal efficiencies as much as 7.5% below efficiencies calculated using the measured exhaust port temperature. Because we feel these measured radial temperature profiles are in error on the high side, we have concluded the uniform mass flow assumption we used in the mixing cup analysis is inadequate.

5.1.3 Twin Plasma Downstream Temperature Profiles

Time averaged radial temperature profiles downstream of the plasma are presented in this section. The temperatures were measured every 1.5 seconds for a total of 90 seconds at six, fixed radial locations, 14.5 cm downstream of the two foci. The thermocouples were positioned along the line which connects the foci, as shown in Figure 40. In each profile in the figures that follow, there are seven points shown; the outer most point at a radius of 52.5 mm was extrapolated from the two nearest measured points, for use in the mixing cup analysis. Each profile represents a time average of the data for the final 45 seconds of the run. We used the final 45 seconds because the carriage thermocouples have a response time of approximately 45 seconds at

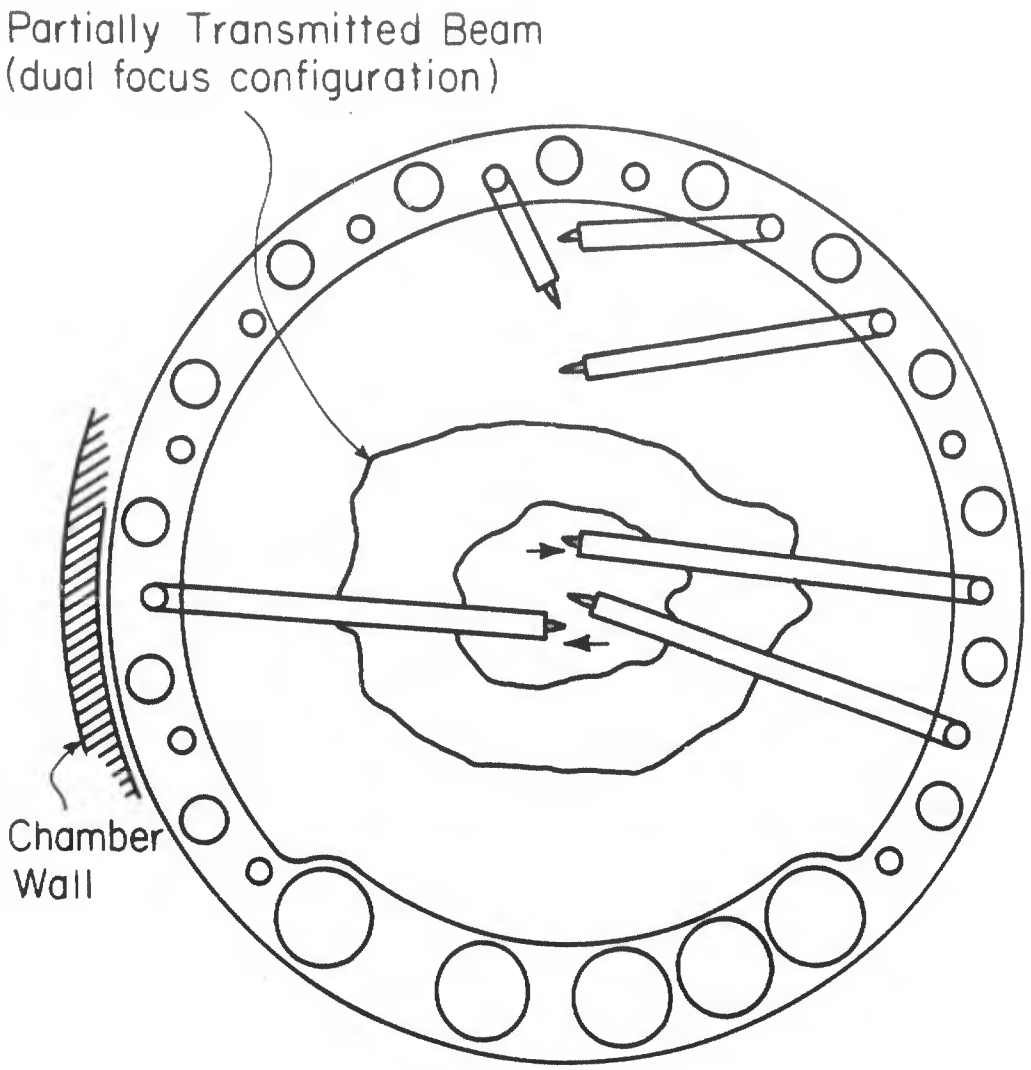

Figure 40: Current carriage thermocouple positions for downstream temperature profile measurements of twin plasmas. The arrows indicate the radial locations of the split beam focii. Note that no thermocouple beads are positioned within the transmitted beam profile. The thermocouple shields have been omitted for clarity.

these low flow velocities. The two foci were symmetrically positioned 12 mm apart within the chamber, each 6 mm from the centerline.

Figures 41 and 42 show the temperature profiles as a function of power at constant velocities of 15 and 54 cm/s, respectively. Figure 43 shows the temperature profile as a function of velocity at a constant total power of 5.0 kW. All of the profiles look qualitatively similar, and as one expects, temperature increases with decreasing velocity at constant power, and temperature inreases with increasing power at constant velocity.

One interesting point however, is the maximum temperature occurs at the center of the chamber and not directly above one of the plasmas. We believe this is due to the innermost gas being heated by both plasmas. One may also notice the apparent asymmetry in the temperatures directly above the plasmas. For the profiles in Figure 43, the temperature above the plasma at r = 6.0 mm is higher than that above the other plasma at r = - 6.0 mm (by extrapolation). In Figure 42, the reverse is true. This phenomenon is not yet understood.

5.2 Exhaust Port Gas Temperature Measurement

The exit gas temperature is measured within one of the four chamber exhaust ports by means of a miniature, type K thermocouple inserted radially into the duct. Assuming the gas is well mixed before reaching the thermocouple, the temperature measured here is, ideally, the mass averaged exit temperature and may be used directly in Eqs. (8) and (9) to calculate the thermal efficiency. This assumption seems reasonable because of the enormous area decrease and resulting velocity increase as the incompressible gas is forced into the small diameter exhaust ducts, from the comparatively large

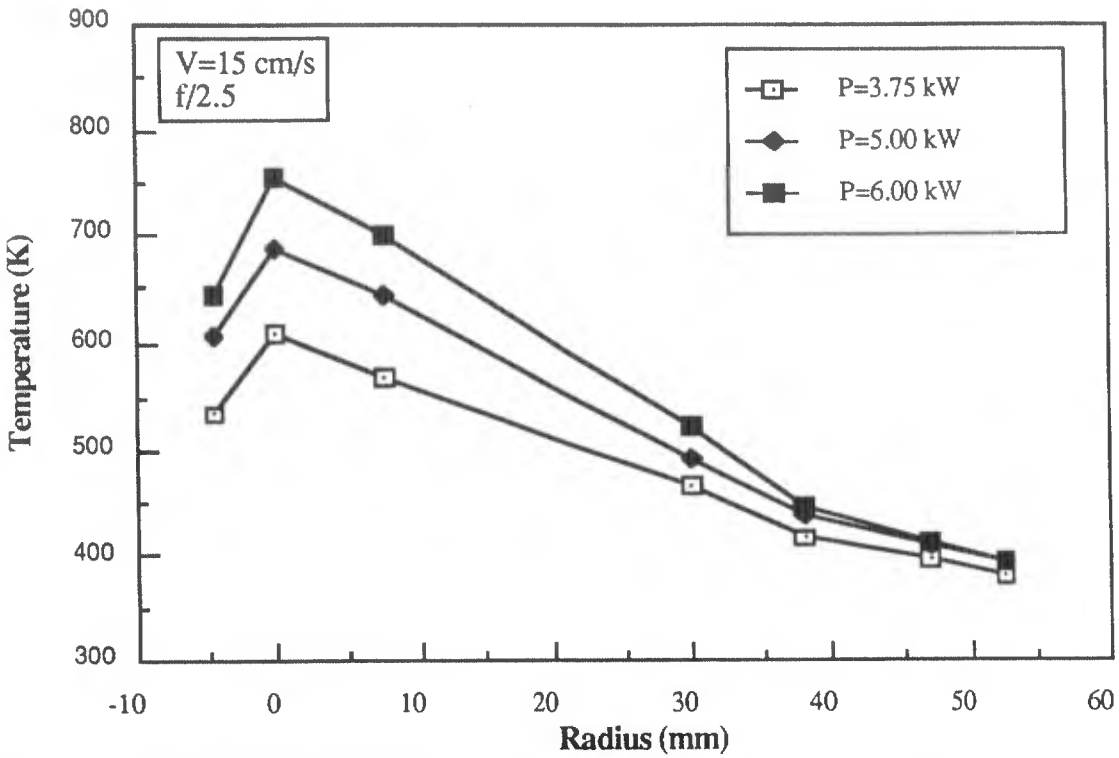

Figure 41 Temperature profiles 14.5 cm downstream of twin plasmas located at radii of -6.0 and +6.0 mm in a 15 cm/s argon flow.

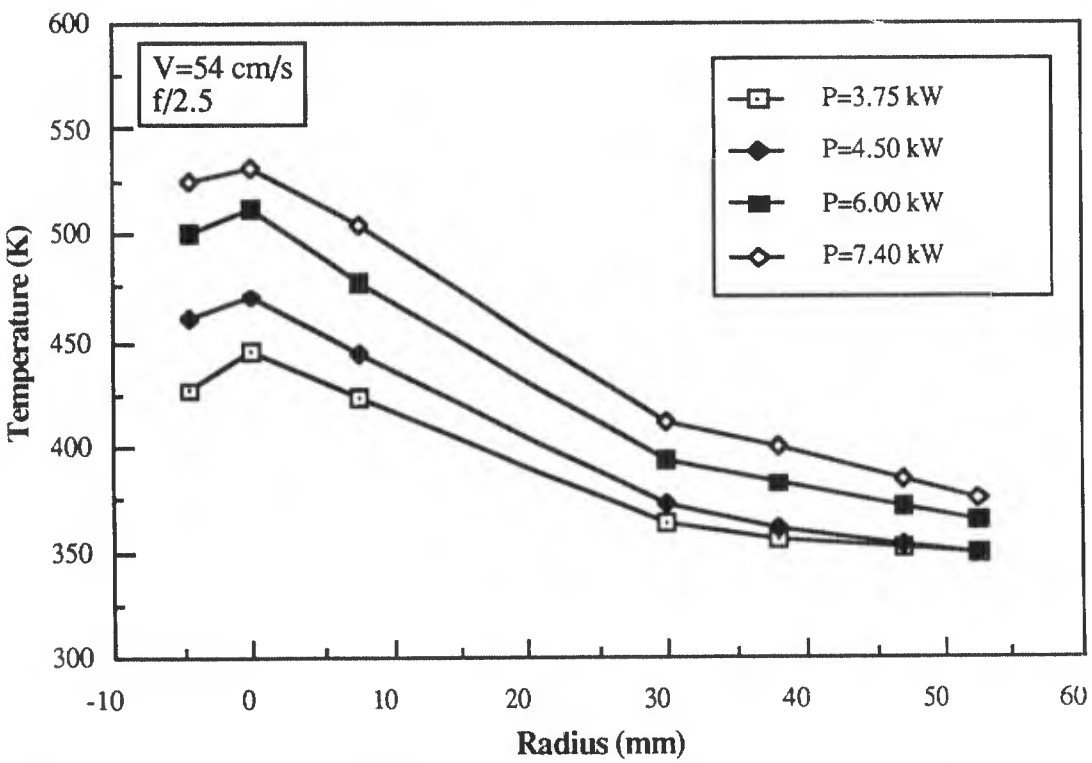

Figure 42 Temperature profiles 14.5 cm downstream of twin plasmas located at radii of -6.0 and +6.0 mm in a 54 cm/s argon gas flow (note temperature scale change.)

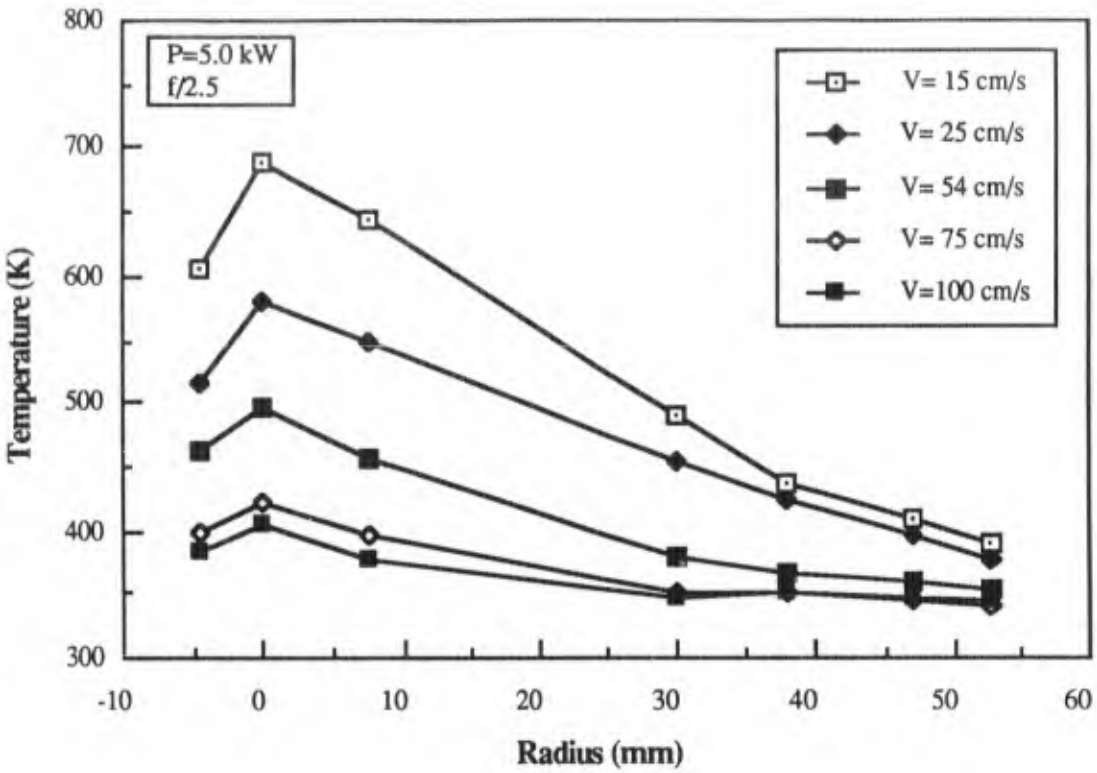

Figure 43 Temperature profiles 14.5 cm downstream of twin plasmas sustained at 5.0 kW total input power and located at radii of -6.0 and +6.0 mm within an argon gas flow.

diameter chamber. Even if the gas is well mixed however, this calculation does not yield the true thermal efficiency because of thermocouple errors and convective effects between the gas and the walls of the chamber and calorimeter. In general, we believe the efficiencies determined with this technique are somewhat lower than the true thermal efficiencies, for reasons discussed in the following sections.

5.2.1 Exhaust Port Thermocouple Errors

The thermocouple errors in the exhaust port gas temperature measurement are not as severe and are better estimated than those errors associated with the carriage thermocouple measurements. This is because the exhaust port thermocouple is not exposed to any laser or plasma irradiation and the gas velocity is at least an order of magnitude higher in the exhaust duct, resulting in improved convective heat transfer to the probe. In addition, conductive errors are negligible here because the probe is immersed in a relatively isothermal flow. There still remains a slight radiative error, however, because the exhaust gas is, in general, hotter than the duct wall and the probe therefore radiates to the wall.

Table 2 indicates the estimated difference between the gas and thermocouple temperatures as well as the associated efficiency errors for three different velocities during an experiment where the input power to the plasma was 6.2 kW. At low velocity, the temperature measurement error is comparatively higher than for the higher velocity cases, because of the reduced convective heat transfer to the probe; note, however, the errors in efficiency are comparable in all three cases, because even though the temperature errors are less at higher velocities, the efficiency at a given

power is more sensitive to exit gas temperature errors at higher mass flows. Although this error in efficiency is relatively small for these flow conditions, it does exist and may become more significant under different operating conditions. In an effort to verify the magnitude of this error and to minimize it, we have installed a millisecond response, multi-shielded thermocouple in a different exhaust port. No data is available yet, but, by monitoring both exhaust port thermocouples, an experimental verification of the radiation error associated with the original thermocouple will soon be available.

5.2.2 Convective Losses to the Walls

The convective losses from the heated gas to the relatively cool chamber and calorimeter walls have also been found to reduce the experimental efficiencies to some extent. Although results are still preliminary, we have found losses in efficiency of about 1% for flow velocities below 75 cm/s and as much as 3.5% for flow velocities in the 75-120 cm/s range. The increased convective losses at higher velocities is as expected, not only because of the enhanced heat transfer at the wall, but because of better mixing between the stratified gas downstream of the plasma.

Predicting these convective losses is complicated because of several combined effects. For example, the chamber has a nonuniform thermal mass because of the presence of the low conductivity pyrex windows and the heat sink effect of the thermocouple retract box, leading to a very complicated wall temperature distribution. In addition, the inlet gas is slightly preheated by convection because the upstream chamber wall is radiatively heated by the plasma, whereas the hotter downstream gas tends to lose heat to

TABLE 2

Estimated Exhaust Port Thermocouple Errors at P = 6.2 kW

V (cm/s)	h_c (W/m^{2}K)	T_{bead} (K) (measured)	T_{wall} (K) (approximate)	ΔT_{exit} (K) (calculated error)	$\Delta\eta_{th}$ (%) (error)
15.2	342.2	570	350	-15.0	-0.4
49.9	528.7	435	325	- 2.6	-0.21
98.6	720.3	395	300	- 1.3	-0.22

NOTES:

(1) The thermocouple bead was modeled as a small sphere within a much larger isothermal blackbody cavity.

(2) The thermally oxidized bead was assumed to have an emissivity of unity.

(3) The wall temperature of the exhaust port duct was assumed because it was unavailable at the time of the calculations.

(4) Real gas properties were used and the convective heat transfer coefficient h_c, was calculated from the correlation cited in [43].

the cooler chamber wall. Although these effects tend to cancel each other, the latter effect is believed more predominant, because of the larger gas/wall temperature difference along the downstream wall.

For extended runs at some operating conditions, the chamber wall may become hotter than the nearby gas due to plasma irradiation. However, for all cases to date, this has not occurred based upon the comparision of the outermost downstream carriage thermocouple measurements with chamber wall temperature measurements near the plasma. Furthermore, losses within the calorimeter are very difficult to estimate because calorimeter wall temperature data is not available. We believe that the calorimeter wall is cooler than the gas because of the relatively large flow rate of cooling water circulating through it. Finally, all of these effects are a function of time because the chamber wall temperature distribution varies in time. This time variation warrants the need for normalizing the data with respect to time to insure a more accurate analysis.

5.2.3 Normalization of Data

The time variation of the convective effects discussed above leads to a time variation in measured efficiencies also. This time dependence has been found to be reasonably consistent for given conditions, provided the initial chamber temperature is the same. (Obvious as it seems now, this was not evident earlier, and as a result, the initial chamber temperature varies somewhat between successive runs as well as between day-to-day runs at the same operating conditions.)

In an effort to normalize the exhaust port temperatures measured as a function of time, an initial chamber temperature was chosen arbitrarily and

the remaining data was adjusted in time for comparison purposes. The experimental data reported here was normalized to an arbitrary reference run which had an initial chamber temperature of 344 K and 115 seconds of data. Therefore, by definition, the adjusted time, t_a, of any run is zero at the point in time of the raw data where the chamber temperature is 344 K. In addition, a dimensionless time, t*, has been defined which represents the ratio of the adjusted time corresponding to the exit gas temperature used in the efficiency calculation, to the maximum adjusted run time. Thus,

$$t^* = \frac{t_a\ (\bar{T}_e)}{115} \ .$$

The value of t* in the reduced data varies from 0 to 1. A value near zero indicates data near the beginning of a run, and a value near unity indicates data near the end of a run. These definitions allow us to compare efficiencies with respect to time, referenced to the same initial chamber temperature. By comparing data at the same t* we are attempting to compare data with equal convective losses. Ideally, this normalization with respect to time ensures the convective losses are nearly equal for different sets of data at the same operating conditions. However, this is at best, only approximately true for comparisons between data at different operating conditions. This is because the convective losses are presumably a function of the operating conditions as well as time. This normalization was especially useful when comparing single and twin plasma data because the twin plasma runs were significantly shorter than earlier single plasma runs.

5.2.4 Single Plasma Data

As discussed earlier, the thermal efficiency is a measure of the amount of input laser energy retained by the working gas, downstream of the plasma. Modeling results [4,5] have indicated the thermal efficiency is influenced by the plasma size and shape as well as the temperature distribution within the plasma, and have predicted that these plasma characteristics are influenced by the input laser power and beam geometry as well as the flow velocity. To verify these model predictions we have undertaken experiments at constant power while varying flow velocity, and at constant flow velocity while varying laser power. To date all of these measurements have been made at an optical configuration of f/2.5, but experiments at f/4 and f/8 will be undertaken later this year (1987).

In general, the experimental measurements have shown the trends predicted by the model but measured efficiencies have been significantly lower in all cases. This was expected to some extent beause the model does not include any convective losses to the chamber wall, whereas the experimental absorption chamber used in these experiments was not insulated. Significant increases in efficiency may be achieved by using a regenerative absorption chamber to recover plasma radiation losses as well as wall convective losses.

Convective losses from the gas to the chamber wall can be significant as shown in Figure 44, which illustrates experimental efficiencies as a function of flow velocity for an input power of 5.5 kW, at two values of t*. For each velocity, one data set was used to calculate the efficiency at the normalized times of t* = 1/3 and t* = 1. The results indicate convective losses are apparently reduced as the chamber wall temperature distribution increases, because the measured efficiency is higher at later times during any given

run. In addition, and as expected, these convective effects appear more significant at the higher flow velocities. We plan to make runs for longer durations in an effort to determine the asymptotic value for these thermal efficiencies with the current facility.

It should be noted at this point that because the measured efficiencies are a function of time, comparisons between different operating conditions must be made at the same relative time, that is at the same t*. As a result, in all of the figures which follow the respective value of t* for that data is listed. When comparing data between two respective figures, one must compare the same value of t* to avoid discrepancies.

Figure 45 shows a comparison between experimental efficiencies at 5.5 kW and model predictions at 5.0 kW as a function of velocity. Note the trend in efficiency variation is very similar in both sets of data, each displaying a maximum efficiency at a flow velocity near 100 cm/s. We plan to extend these experimental results to verify the predicted blowout velocity as well as the predicted efficiency variation at higher flow velocities, shown previously in Figure 8. These experimental data represent the highest efficiencies measured thus far at these conditions as indicated by t* = 1.

The predicted efficiency variation as a function of velocity at constant power is a result of several contributing factors. For the case of 5 kW input power, the model [4,5] indicates that as the velocity initially increases, the plasma moves closer to the focal volume where the laser intensity is higher, thereby increasing absorption. In addition, photographs shown in Figure 46 indicate that as the velocity increases, the plasma assumes a thinner shape, which reduces the radiative volume. As the velocity is further increased however, the model predicts the peak temperature of the plasma is reduced

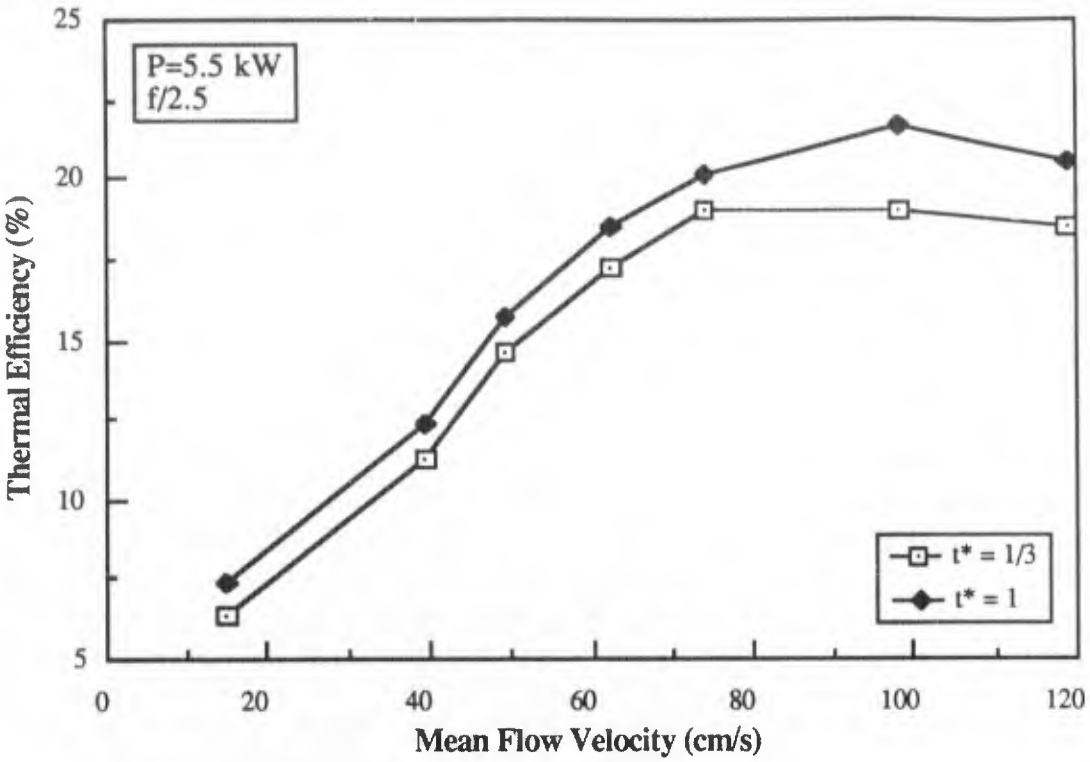

Figure 44 Single plasma efficiency vs velocity at constant power normalized with respect to time.

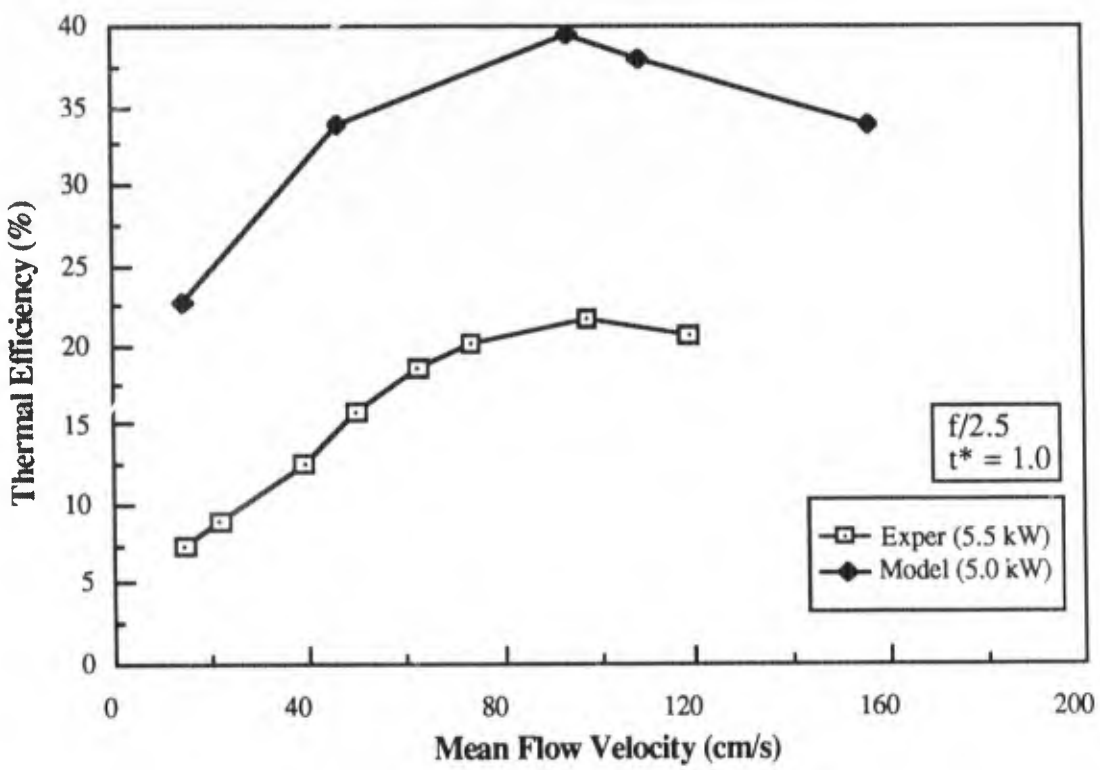

Figure 45 Normalized single plasma experimental efficiencies vs model predictions [4,5] as a function of velocity (note scale changes).

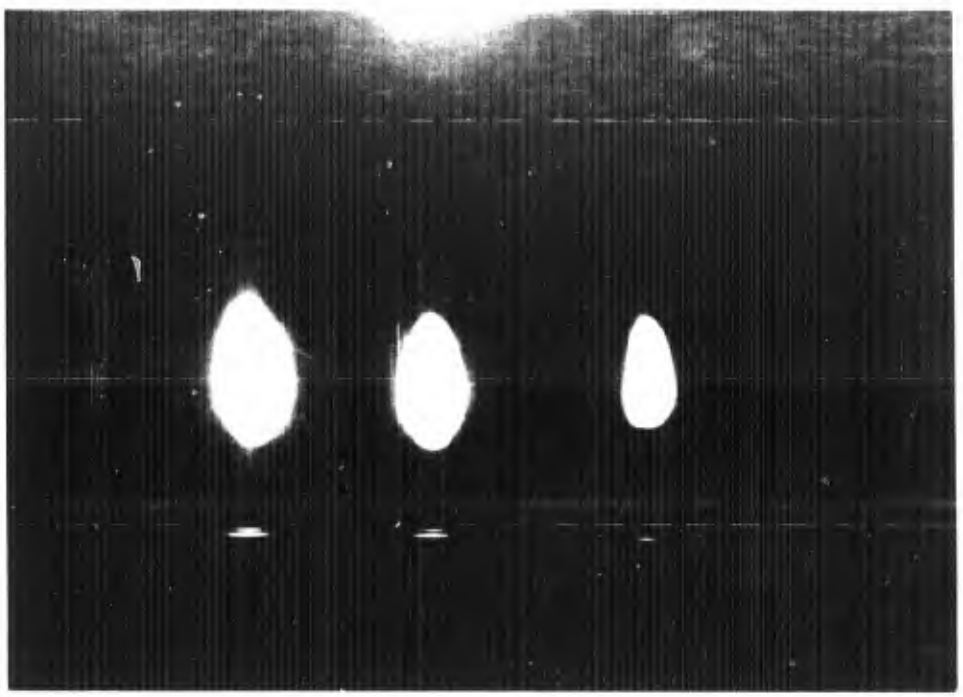

Figure 46: Photographs of argon laser-sustained plasmas with a 5 kW input power, for chamber velocities of 23, 64 and 123 cm/s. Note the plasma becomes thinner as the velocity is increased.

because of the increased mass flow. Although this reduces the radiative losses further, it also tends to reduce plasma absorption. Eventually, the losses in absorption dominate the reduction in plasma radiative losses, and this results in decreasing efficiency for velocities greater than 100 cm/s.

Figure 47 shows a comparison of experimental efficiencies with model predictions, as a function of laser power at 50 cm/s. Note $t^* = 3/4$ for these data because these runs were shorter than those reported earlier. Here again the experimental efficiencies are significantly lower than predicted, but they do tend to verify the trend. The decline in efficiency with increasing laser power is explained physically by an increase in plasma size and peak temperature as power increases. Although these effects tend to increase absorption, radiative losses are also increased and overwhelm the increase in absorption. Photographs shown in Figure 48 show the plasma volume increases with increasing power which leads to increased radiative losses.

Figure 49 shows experimental results for efficiency as a function of laser power at three different velocities. The trend of decreasing efficiency with increased power, at constant velocity, is seen again for the reasons noted above. In addition, one notes the efficiency at a given power is increased with increasing velocity for the velocities shown. This is as expected based upon the previous discussion of Figure 8, which indicated increasing efficiencies at 5 kW as velocity increased to 100 cm/s. We plan to make measurements at even higher velocities, to determine if this trend reverses, as predicted by the model.

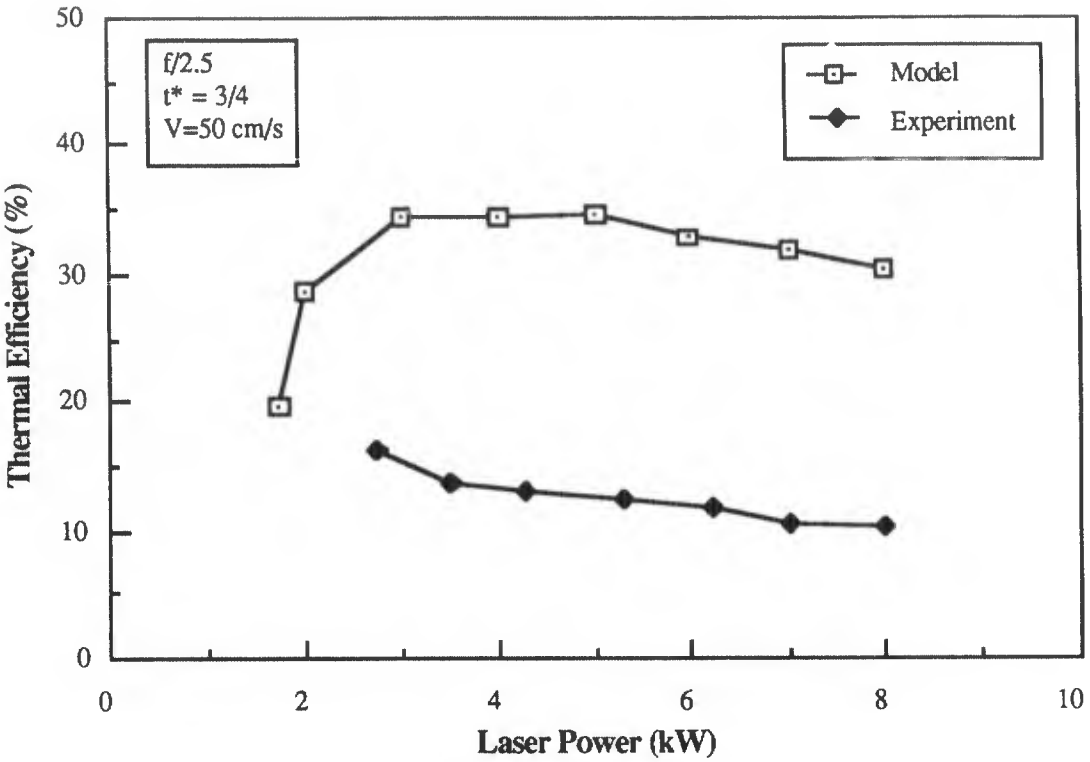

Figure 47 Normalized single plasma experimental efficiencies vs model predictions [4,5] at a constant velocity and varying input laser power.

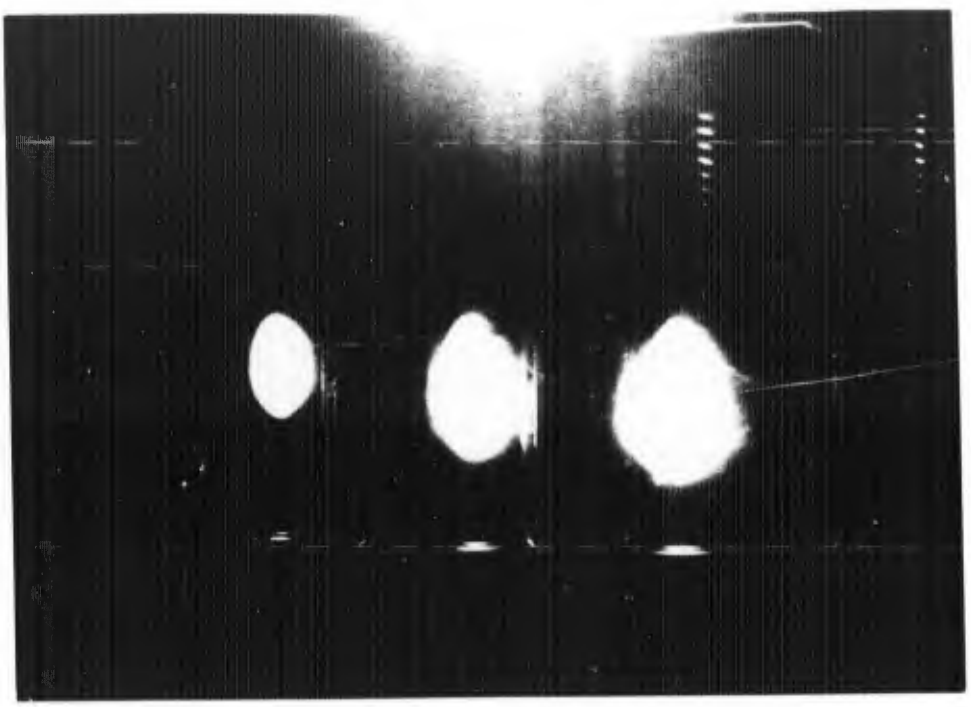

Figure 48: Photographs of argon laser-sustained plasmas at a constant chamber velocity of 45 cm/s for laser powers of 2.5, 5 and 7 kW. Note the plasma size increases with increasing power.

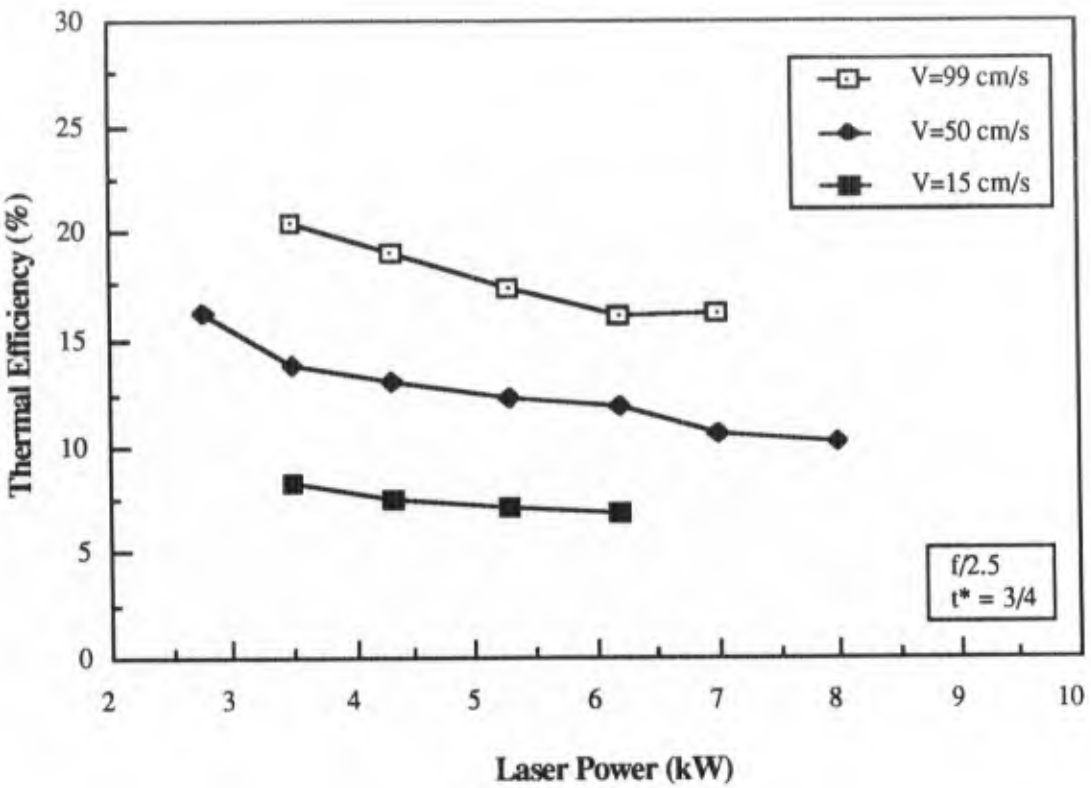

Figure 49 Normalized experimental efficiencies as a function of input laser power at three constant but different velocities.

5.2.5 Twin Plasma Data

As discussed in Section 1.3, model results indicate for a given chamber flow velocity and input power, several relatively low power plasmas may be more thermally efficient than one high power plasma. To verify this finding, the optical system of this facility has been revised (see Section 2.3) permitting the study of two distinct, adjacent plasmas of nearly equal power supported by one laser source. For this facility, the total input power available after losses is approximately 8 kW and therefore allows the study of twin plasmas with respective powers of up to 4 kW each.

The model prediction of improved thermal efficiencies with multiple plasmas can be investigated to a limited extent with this facility. For example, data from Figure 9 indicates that, at f/2.5, two (2 kW) plasmas operate more efficiently than one (5 kW) plasma for chamber velocities of 10-40 cm/s, and beyond 40 cm/s this is longer true. Although model results are not complete for operating conditions available with the current experimental facility, preliminary experimental results confirm twin plasmas are more efficient for some operating conditions.

Figure 50 shows an experimental comparison of single and twin plasma (separation distance, d=12 mm) efficiencies as a function of power at constant velocities. At 15 cm/s, the twin plasma is slightly more efficient for total powers between 3.75 and 6.0 kW. For the higher velocity case, the twin plasma is significantly more efficient than the single plasma near 4 kW, but the improvement in efficiency becomes less pronounced as the power increases. This may indicate the point of diminishing returns, that is the limit of this operating regime where twin plasmas are no loger more efficient than a single plasma with the same total input power. It should be noted here that the data

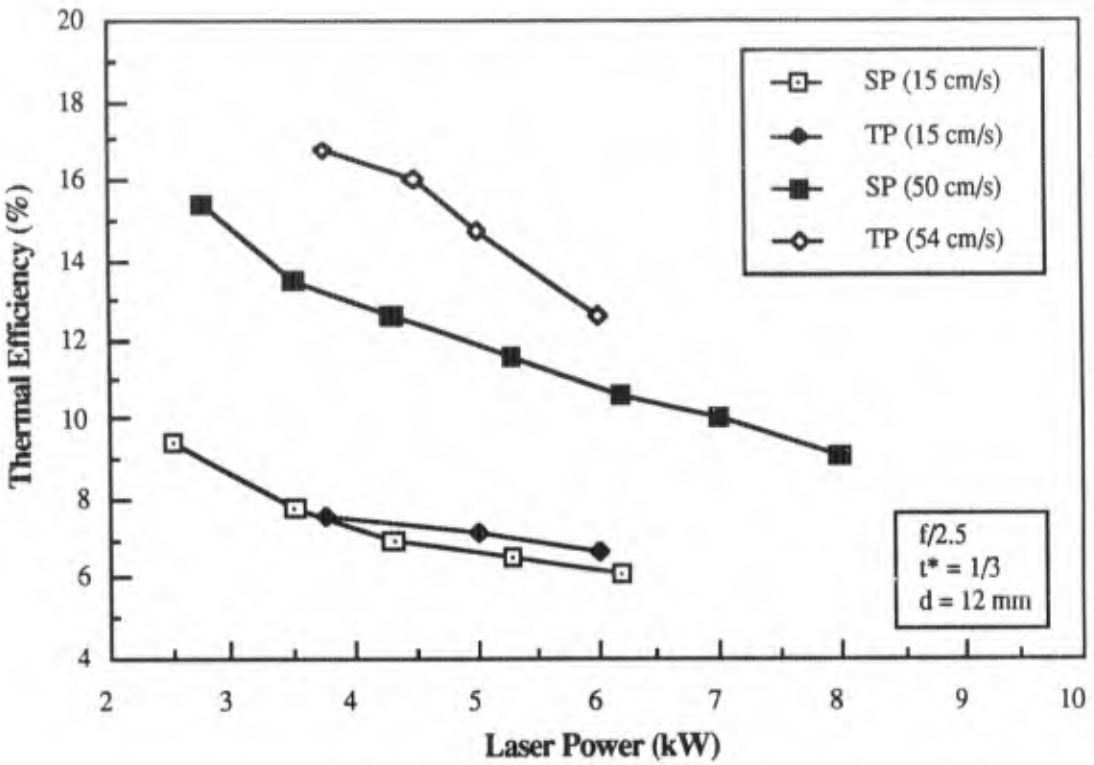

Figure 50 Normalized experimental single (SP) and twin (TP) plasma efficiency comparison as a function of total laser input power at constant velocities. The focal point separation distance, d, was 12 mm.

is presented here at $t^* = 1/3$ because the twin plasma runs to date have been somewhat shorter than the earlier single plasma runs.

A key parameter for multiple plasmas may be the separation distance. It is likely that for a given laser power, there is one optimum separation which maximizes the laser-to-gas energy conversion. We plan to extend this work to better define this phenomena in the operating regime available with this facility. Here again we plan to carry out tests, for longer duration, in an effort to find the optimum values of the efficiencies for these conditions. In addition, we plan to vary plasma separation distance to determine if it influences the twin plasma efficiencies because of either radiative view factor or convective effects.

5.3 Aspirated Thermocouple Probe

As discussed above, accurate thermocouple measurements are difficult to achieve inside the absorption chamber because of the adverse conditions the probes are subjected to. The new shielding technique discussed earlier has led to a significant improvement in these measurements but difficulties still remain. In general, these measurements are complicated by the relative magnitudes of the radiative and convective heat transfer between the thermocouples and their environment. Specifically, the carriage thermocouples are simultaneously exposed to a highly radiative plasma, a low velocity gas flow at lower temperatures, and a cooler chamber wall. These conditions alone make it practically impossible to estimate the error in these temperature measurements [41]. In addition, the plasma and the partially transmitted laser beam can also indirectly lead to thermocouple errors. Experiments have indicated the carriage thermocouple shields can, in some cases, become hotter than the

flowing gas, because they absorb some incident transmitted laser irradiation as well as direct plasma irradiation. In these cases, for any given thermocouple, the shields radiatively heat the ceramic sheath, which in turn, conductively heats the thermocouple leads to a temperature higher than the bead. The thermocouple leads then conductively heat the bead which leads to a gas temperature measurement that is artificially high. Although we believe the profile shapes are correct, these carriage thermocouple errors make the absolute magnitude of the measured radial temperatures uncertain. In an effort to improve these measurements further, a simple aspirated thermocouple has been designed and built.

The basic principle of a simple aspirated thermocouple is to completely isolate the thermocouple from radiative sources and sinks by placing it inside a thin-walled metal tube and drawing the sample gas into the tube by means of an ejector or suction pump. Ideally, the gas is aspirated through the tube at a velocity high enough to insure the tube wall temperature is very close to the gas sample temperature, thus minimizing the thermocouple-environment radiation error. In addition, conduction errors along the thermocouple leads are virtually eliminated because the leads are immersed within an isothermal gas flow.

The design of our probe is shown in Figure 51. The probe assembly consists of a ribbon thermocouple positioned coaxially within a copper plated stainless steel tube, with the temperature sensing ribbon located just beyond the throat of a converging-diverging nozzle. The nozzle serves to accelerate the low velocity sample gas and improve convective heat transfer to the thermocouple ribbon. In addition, the ribbon thermocouple provides a faster response time than a conventional beaded thermocouple because of the increased surface area to volume ratio of a ribbon compared to a bead.

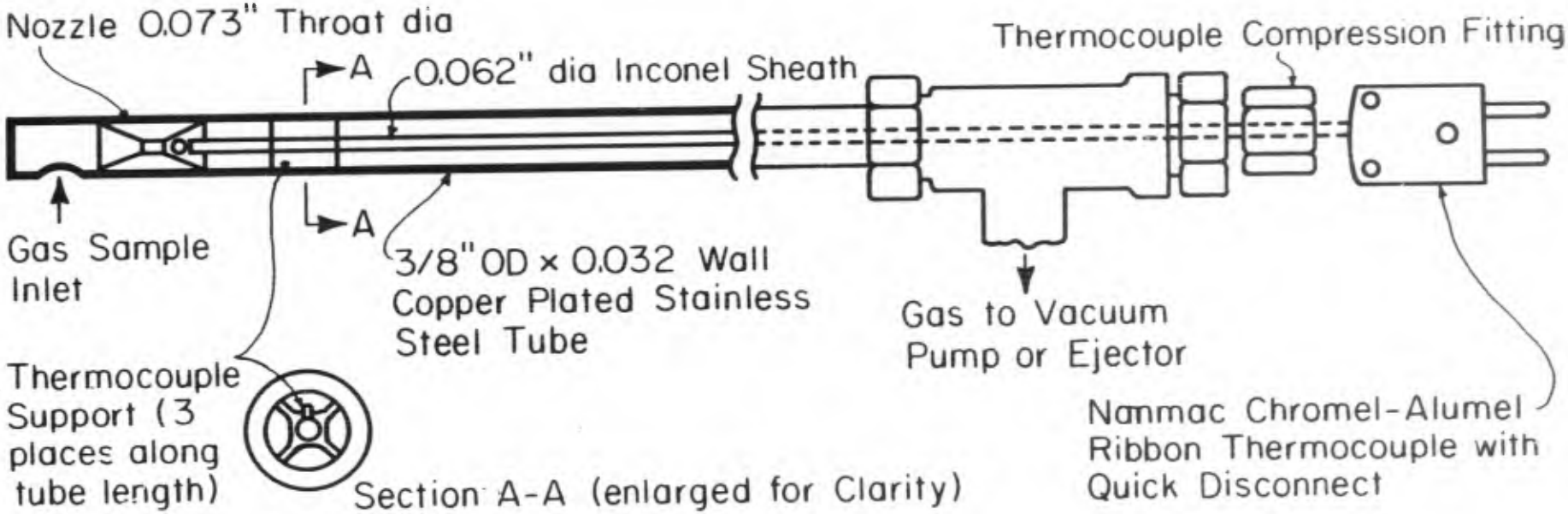

Figure 51: Schematic of the aspirated thermocouple probe with various components labelled. The gas sample inlet port is 1/4 inch in diameter. The nozzle and end cap were oven brazed to the pyrometer tube. The removable thermocouple supports are fixed to the inconel sheath by means of a set screw shown in Section A-A.

In operation, the sampling end of the probe is inserted radially into the chamber and the other end is connected to a suction pump. The gas drawn through the probe is controlled and monitored by a flow meter in an effort to sample the chamber flow isokinetically, assuming the chamber mass flow distribution is uniform. The probe is incrementally traversed across the chamber cross-section to measure the radial temperature profile of the downstream gas within the chamber. The portion of the probe between the gas inlet port and the chamber wall is shielded from plasma and transmitted laser radiation, to ensure the tube wall temperature remains close to the sample gas temperature. The copper plating on the tube ensures any area which is not shielded reflects most of the laser irradiation rather than absorbing it. While located outside the transmitted beam profile, the probe inlet port is positioned so it faces the incoming gas flow, i.e., at the forward stagnation point. For measurements taken within the beam profile, the probe inlet port is positioned in the wake of the probe, i.e., at the rearward stagnation point. In this case, positioning the inlet port at the rear stagnation point prevents any transmitted laser radiation from entering the pyrometer tube and reaching the thermocouple by internal reflections. Chedaille and Braud [44] have indicated this probe orientation does not introduce any significant error in the temperature measurements.

Temperature measurements obtained with an aspirated thermocouple are superior to the carriage thermocouple array for several reasons. First of all, in this technique probe induced flow disturbances are reduced because a single probe is radially traversed across the chamber cross-section, rather than inserting several fixed shielded thermocouples. In addition, the thermocouple within the pyrometer tube is completely shielded from the plasma and

transmitted laser radiation, while the convective heat transfer to the thermocouple is significantly increased by the use of a ribbon thermocouple positioned just aft of the nozzle throat within the tube. The combined effect of these probe characterisitcs leads to a significantly reduced gas temperature measurement error.

At this point no aspirated thermocouple measurements have been made, but the probe has been designed and built. Testing and calibration are currently being undertaken. This probe will provide independent measurements of the radial temperature profile downstream of the plasma and give a more quantitative indication of the errors associated with the carriage thermocouple measurements.

SECTION 6: CONCLUSIONS/SUMMARY

6.1 General Summary

The research program that has been described is a continuing in-depth study of laser-sustained plasmas for use in laser propulsion. Experiments using a 10 kW CO_2 laser have shown that laser-sustained plasmas can be reliably initiated using metallic targets, and are highly stable phenomena which will adjust to variations in laser power or flow velocity. Reliable methods of plasma initiation have been developed.

Calorimetric studies have shown that the plasmas are capable of absorbing a large fraction of the incident laser energy in extremely short distances, typically a few centimeters. Absorption fractions as high as 80% have been demonstrated experimentally, and the dependence of absorption on power, pressure, optical geometry, and flow rate have been studied. In general, absorption is found to increase asymptotically with laser power, and decrease slightly with flow velocity. There is also an apparent increase in absorption at higher gas pressures.

The fraction of the incident laser power retained by the gas as thermal energy (thermal efficiency) has been measured under a range of conditions, but efficiencies only as high as 22% have been demonstrated. It has been found that operation at higher flow rates reduces radiative losses, causing the efficiency to increase until reaching a peak value. Operation at higher gas pressure appears to reduce the efficiency considerably due to increased radiative losses.

Overall plasma behavior has also been studied using visible, infrared, and spectroscopic imaging. Absorption fractions and efficiencies calculated

using the spectroscopic temperature fields are in good agreement with the other experimental measurements. Plasma minimum maintenance powers and blowout velocities have also been measured.

An accurate two-dimensional model of argon laser-sustained plasmas has also been developed. The model is unique in its use of a cylindrical geometry, focused laser optics, real gas properties, and accurate absorption and emission characteristics.

The predictions of the model have been shown to be in reasonable agreement with the experimental measurements, specifically in the areas of plasma size, shape, position, peak temperatures, absorption fractions, thermal efficiencies, flow rate and f/# dependence, minimum maintenance powers, and blowout velocities.

The model indicates that the thermal efficiency is maximized by operating at higher flow rates, a prediction which has been verified experimentally. The model also predicts that efficiencies as high as 75% can be achieved by using f/16 optics and still higher flow velocities; this prediction is now being explored experimentally using a system of NaCl lenses. The model has also been useful in providing a better understanding of laser-sustained plasma physics, and has led to the identification of new areas of operation which could increase the efficiency even further. These include the use of multiple plasmas, turbulent mixing, and flowing jet impingement.

The results of these studies have been used to make a preliminary assessment of the feasibility of laser propulsion using laser-sustained plasmas. It appears likely that efficiencies approaching 90-100% should be achievable when using regenerative cooling. In addition, by carefully selecting the chamber diameter and using multiple plasmas, high specific

impulses should be possible while operating at these efficiency levels. Thus, from an energy conversion standpoint, laser propulsion appears to be a feasible form of advanced rocket propulsion.

6.2 Work in Progress/Research Needed

Significant progress has already been made in gaining a fuller understanding of the physics and behavior of laser-sustained plasmas used for laser propulsion. In addition to the results discussed above, several new areas of investigation are also possible.

In the immediate future, several aspects of the experimental work will be extended to new areas. Most importantly, thermal efficiency measurements will be attempted using optical f numbers of 4, 8, and 16 using a system of salt lenses. These measurements will be used to verify the modeling predictions of thermal efficiencies approaching 80%.

Operation at high f numbers will require considerably greater flow velocities to reach the efficiency peaks. It may be necessary to design a completely new absorption chamber (with a reduced diameter) in order to achieve sufficient measurement accuracy at these high flow rates.

Such a new chamber can also be used to directly measure the fractional radiation loss to the chamber walls by carefully monitoring the wall temperature at a number of locations. Alternately, radiation losses may be measured by actively cooling the chamber with a water or gas flow, and monitoring the change in the temperature of the coolant. This latter approach can incorporate regenerative cooling of the chamber, in which the argon is used as the coolant. Regenerative cooling is expected to produce sizable increases in the thermal efficiency.

Another area requiring further study is the measurement of flow velocities and flow patterns within the chamber. Such flowfield measurements are also one goal of the LIF diagnostic system now being tested. This system will provide instantaneous temperature mappings of the downstream flowfield, and should provide significant information on flow patterns and velocity distributions within the chamber. The LIF work will initially rely on excitation of indium seedants embedded in the argon flow, but the feasibility of exciting LIF in argon or helium should also be explored. Also, a new high-speed, high-resolution CCD detection system will be in place by next year, providing much higher frame rates, improved sensitivity, and more sophisticated data manipulation.

In addition, the study of multiple plasmas will be continued. The use of multiple plasmas appears to be one way of operating at high specific impulses without sacrificing thermal efficiency. The most important question regarding multiple plasmas is how the closely spaced plasmas will interact, especially radiatively. This is now being tested experimentally by splitting the 10 kW beam into two halves and sustaining a plasma with each half, separated by a few centimeters.

Another important technique is the modification of chamber flow patterns to induce greater mixing for increased thermal efficiency. In order to maximize the efficiency, it is necessary to have very high plasma core temperatures (to maximize the global absorption), but also to reduce the temperatures just downstream from the focal volume, where much of the radiation loss occurs. This can be accomplished by injecting jets of cold gas into the downstream portions of the plasma. The same effect is produced by

improving the mixing in the downstream flowfield. This can be accomplished by increasing turbulence in the flow, possibly by inserting a bluff body just upstream from the plasma.

Another method for increasing the thermal efficiency involves intercepting the radiation emitted by the plasma before it reaches the chamber walls. One approach is to seed the argon with a material (possibly metal seedants) that will absorb the intense UV and visible radiation emerging from the plasma (which is optically thin at those wavelengths). It would probably be best to avoid passing the seeds through the plasma, and injecting them only in the outer portion of the argon flow that passes along the chamber walls.

A similar idea is the use of alkali seeds to reduce temperatures within the plasma core. These seeds release additional free electrons to boost the inverse bremsstrahlung absorption coefficient at low temperatures. However, it is thought that the increased electron number density leads to increased continuum radiation losses from the plasma, even though it is at a lower temperature. Neverthless, it is conceivable to select a seed that will greatly decrease the optical depth of the plasma to radiation loss. This would have the effect of holding in more of the emitted radiation. In effect, the plasma would be transformed from a volume radiator to a surface radiator, and total radiation losses should be reduced. Alkali seeds placed in argon gas are known to greatly increase the optical depth at infrared wavelengths, but it is not known if the same effect occurs at the more important visible and UV bands.

In another area, it would be very desirable to operate at still higher laser powers, such as 20 or 50 kW. From the beginning, the plasma chamber was designed for easy mobility, so that it could be temporarily moved to another

laboratory where a higher power laser is available. Tests at higher powers would be useful to verify the modeling prediction that the peak efficiency increases slightly with laser power.

At some point in the future, it will also be desirable to operate using hydrogen as the propellant gas. The elaborate safety systems required for hydrogen make this proposition both costly and time-consuming. Nevertheless, hydrogen is the next logical step in the verification of laser propulsion feasibility. Some thought should also be given to the use of helium. Although this gas is not molecular, helium's much higher specific heat gives it thermal characteristics that are much more similar to hydrogen than is argon.

Another new area of experimentation will be the exploration of new laser wavelengths. The two most interesting choices are the mid-infrared range (near one micron) which corresponds to the emission wavelength of chemical lasers, and wavelengths that may be generated by a tunable free-electron laser. It may be possible to tune this latter device to a specific energy level transition of hydrogen. This approach could lead to reduced absorption and increased radiation loss, but this needs to be explored experimentally. It is conceivable to avoid this problem by simultaneously pumping several different energy level transitions.

It may also be useful to attempt the initiation of LSP's using the excimer laser from the LIF system. The power output of this laser should be just high enough to sustain a plasma, but initiation could prove difficult. The reduced inverse bremsstrahlung absorption coefficient at this UV wavelength could also be a problem. If plasmas can indeed be sustained, it would be useful to explore the effects of the high repetition pulsed beam on plasma stability.

In the modeling area, the first task will be to improve upon certain aspects of the model that are not fully accurate. These aspects include argon property information, variable grid spacing, and a new method for calculating laser energy absorption. Following this, a decision needs to be made as to whether the model should be modified to include full two-dimensional flow effects. Such a change involves considerable work, and will probably result in an order of magnitude increase in computation time. Such a complete model could also be used to explore the effects of modified flow patterns to improve mixing.

The model should also be extended to new operating conditions, such as laser powers up to 10 MW and high gas pressures. The use of hydrogen should also be explored, especially if experimental studies are undertaken. It will also be useful to explore the effects of seed particles used to intercept radiation losses from the plasma. Finally, the model should be used in a more complete study of propulsion parameters, including the complex interplay between specific impulse, thrust and efficiency. Regenerative cooling should be included in these analyses.

6.3 Future Research (Scientific Emphasis)

In order to achieve a better scientific understanding of the laser induced plasma in various gases and its application in propulsion, the following problems should be addressed:

6.3.1 Refraction in Plasma and Threshold Energy for Plasma

We should determine the of threshold energy to sustain plasma depending on the calculated focal volume of the beam. However, the focal volume calculated on the basis of focusing optics alone would be erroneous due to the refraction of the laser beam through the plasma column. Refractive index of the plasma column is directly related to the electron density of the plasma. Therefore, when calculating focal volume and intensity at the focal volume, the index of refraction should be calculated from electron density data and the refraction data will provide the new propagation direction with the help of Snell's law [45]. This will provide the new focal volume. Calculation of the inverse Bremsstrahling absorption coefficient at each axial location will provide the global absorption data.

Initial work for Argon plasmas in the presence of Aluminum targets indicates an 8% increase in beam diameter and 20% absorption loss for a 5 kW beam [46]. This work should be extended for plasma columns for our beams and the new focal point data should be incorporated to calculate the threshold energy.

Electron density data is available from the spectroscopic measurement. A systematic study for elctron density variation with f/#, laser power, and flow velocity should be carried out.

6.3.2 Emission Spectroscopy for Multiple Plasma

Emission spectroscopy data for multiple plasmas is rather difficult to interpret for the temperature, since an axisymmetric assumption for Abel inversion is invalid in this case. Initial order of magnitude temperature estimation is being done using the axisymmetric assumption. However, this

will introduce considerable error at the center of the dual plasma column. On the other hand, this is one of the most interesting regions in the gas dynamics point of view. A new inversion code has to be developed for the dual plasma geometry. A TEM_{10} configuration would be a more realistic description for the dual plasma. This configuration can be mathematically described using Laguerre polynominals for circular symmetry. The inversion code should be modified accordingly, although this will involve considerable work.

6.3.3 Absorption Studies of Multiple Plasma

Another method for determining the spatial energy distribution in multiple plasmas will be to monitor the absorption using a second 10.6 μm source. A narrow collimated beam can be used as a probe beam (see Figure 52) and absorption can be measured which will provide experimental verification of the absorption data calculated from emission spectroscopy. It will also provide spatial distribution of the multiple plasma.

6.3.4 Electron Temperature vs. Heavy Particle Temperature

The temperature calculated from spectroscopy is the electron temperature which is a temperature which is often significantly different from the heavy particle temperature. On the other hand, the heavy particle (neutrals) temperature will represent the r re realistic temperature for the hot gas. A relationship between the electron temperature and heavy particle temperature can be made by using techniques such as thermal conductivity balance. It is rather a new scientific area but extremely necessary.

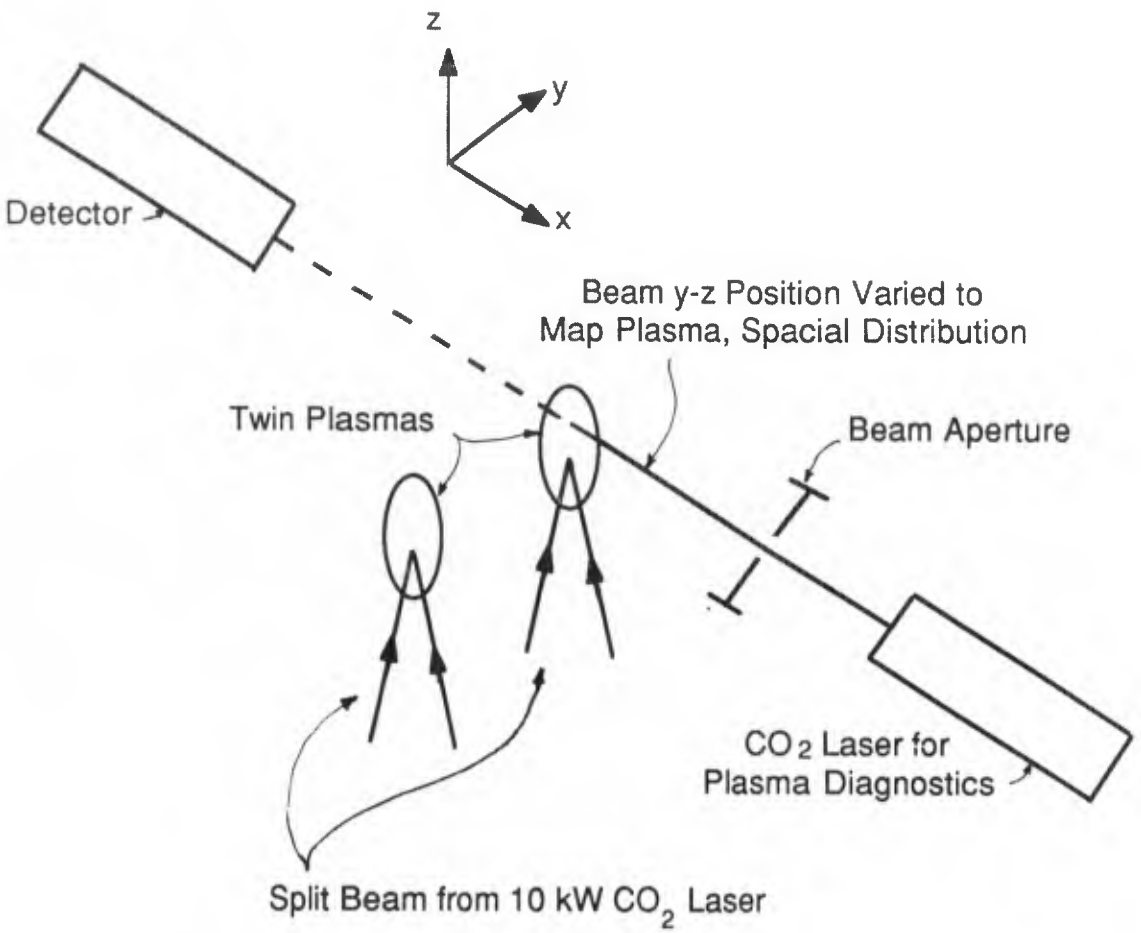

Figure 52: Schematic of proposed method for determining spatial distribution of twin plasmas.

REFERENCES

1. Glumb, R.J. and H. Krier, "Concepts and Status of Laser-Supported Rocket Propulsion," Journal of Spacecraft and Rockets, Vol. 21, pp. 70-79, January 1984.

2. Caveny, L.H., editor, Orbit-Raising and Manuevering Propulsion: Research Status and Needs, published by AIAA, Inc., New York, 1984.

3. Krier, H., Mazumder, J., Rockstroh, T.J., Bender, T.D. and Glumb, R.J., "Continuous Wave Laser Gas Heating by Sustained Plasmas in Flowing Argon," AIAA Journal, Vol. 24, No. 10, pp. 1656-1662, October 1986.

4. Glumb, R.J. and H. Krier, "Two-Dimensional Model of Laser-Sustained Plasmas in Axisymmetric Flowfields," AIAA Journal, Vol. 24, No. 8, pp. 1331-1336, August 1986.

5. Glumb, R.J., Ph.D. Thesis, Department of Mechanical and Industrial Engineering, University of Illinois at Urbana-Champaign, June 1986.

6. Rockstroh, T.J., Ph.D. Thesis, Department of Mechanical and Industrial Engineering, University of Illinis at Urbana-Champaign, October 1986.

7. Kantrowitz, A. "Propulsion to Orbit by Ground-Based Lasers," Astronautics and Aeronautics, Vol. 10, pp. 74-76, 1972.

8. Nebolsine, P. E., Pirri, A. N., Grola, J. S. and Simons, G. A., "Pulsed Laser Propulsion," AIAA Journal, Vol. 19, pp. 127-128, 1981.

9. Dyson, F. J. and F.W. Perkins, "JASON Laser Propulsion Study," SRI International, Arlington, VA, ARPA Order 2504, Summer 1977.

10. Van Zandt, D. M. and T.D. McCay, "Experimental Study of Laser Sparks in Hydrogen," AIAA Paper 83-1443, June 1983.

11. Keefer, D., Welle, R. and Peters, C., "Power Absorption in Laser-Sustained Argon Plasmas,' AIAA Journal, Vol. 24, pp. 1663-1669, 1986.

12. Jeng, S-M. and D.R. Keefer, "Numerical Study of Laser Sustained Argon Plasmas in a Forced Convection Flow," AIAA Paper 86-1078, May 1986.

13. Dresvin, S. V. (editor), Physics and Technology of Low-Temperature Plasmas, The Iowa State University Press, pp. 18-23, 1977.

14. Kramers, H. A., "On the Theory of X-ray Absorption and of the Continuous X-ray Spectrum," Philosophy Magazine, Vol. 46, pp. 836-859, 1923.

15. Wheeler, C. B. and S.J. Fielding, "Absorption of Sufrared Radiation as a General Technique for Determination of Plasma Temperature," Plasma Physics, Vol. 12, pp. 551-564, 1970.

16. Stallcop, J. R., "Absorption Coefficients of a Hydrogen Plasma for Laser Radiation," Journal of Plasma Physics, Vol. 11, pp. 111-129, 1974.

17. Griem, H. R., Plasma Spectroscopy, McGraw-Hill Book Company, Chapter 6, 1964.

18. Farmer, A. J. and B.H. Haddad, "Local Thermodynamic Equilibrium in Free Burning Arcs in Argon," Applied Physics Letters, Vol. 45, pp. 24-25, 1984.

19. Emmons, H. W., Physics of Fluids, Vol. 10, pp. 1125-1131, 1967.

20. Golden, D. E. and H.W. Bandel, Physical Review, Vol. 138, pp. A14-A16, 1965.

21. Cremers, C. J. and R.C. Birkeback, "Application of the Abel Integral Equation to Spectrographic Data," Applied Optics, Vol. 5, pp. 1057-1064, 1966.

22. Cheng, J. K. and L.W. Casperson, "Plasma Diagnostics by Laser Beam Scanning," Journal of Applied Physics, Vol. 46, pp. 1961-1965, 1975.

23. Rockstroh, T. J. and J. Mazumder, "Spectroscopic Studies of Plasma During CW Laser Materials Interaction," to be published Journal of Applied Physics, 1987.

24. Kozlov, G. I., Kuznetrov, V. A. and Masgukov, W. A., "Radiative Losses by Argon Plasma and the Emissive Model of a Continuous Optical Discharge," Soviet Physics JETP, Vol. 39, pp. 66-73, 1982.

25. Cattolica, R.J. and S.R. Vosen, "Two-Dimensional Fluorescence Imaging of a Flame-Vortex Interaction," AIAA Paper 84-1799, AIAA 19th Thermophysics Conference, June 1984.

26. Alden, M., et. al., "Single-Pulse Laser-Induced OH Fluorescence in an Atmospheric Pressure Flame," Applied Optics, Vol. 21, pp.1236-1240, April 1982.

27. Morley, C., "The Application of Laser Fluorescence to Detection of Species in Atmospheric Pressure Flames," Combustion and Flame, Vol. 47, pp.67-81, 1982.

28. Vanderhoff, J.A., Anderson, W.R., Kotlar, A.J. and Beyer, R.A., "Raman and Fluorescence Spectroscopy in a Methane-Nitrous Oxide Laminar Flame," Technical Report ARBRL-TR-02579, Aberdeen Proving Ground, Maryland, 1984.

29. Muller, K.G. and M. Stania, "Laser Fluorescence Spectroscopy of Three-Level Systems," Journal of Applied Physics, Vol. 49, pp.5801-5805, December 1978.

30. Kychakoff, G., Howe, R.D., Hanson, R.K. and J.C. McDaniel, "Quantitative Visualization of Combustion Species in a Plane," Applied Optics, Vol. 21, pp.3225-3227, September 1982.

31. Dyer, M.J. and D.R. Crosley, "Rapidly Sequenced Pair of Two-Dimensional Images of OH Laser-Induced Fluorescence in a Flame," Optics Letters, Vol. 9, pp.217-219, June 1984.

32. Rapagnani, N.L. and S.J. Davis, "Laser-Induced Iodine Fluorescence in a Chemical Laser Flowfield," AIAA Journal, Vol. 17, pp.1402-1404, December 1979.

33. Kychakoff, G., Knapp, K., Howe, R.D. and Hanson, R.K., "Flow Visualization in Combustion Gases Using Nitric Oxide Fluorescence," AIAA Journal, Vol. 22, pp.153-154, January 1984.

34. Cattolica, R.J., "OH Rotational Temperature From Two-Line Laser-Excited Fluorescence," Applied Optics, Vol. 20, pp.1156-1166, April 1981.

35. Gross, K.P. and R.L. McKenzie, "Optical Measurements of Fluctuating Temperatures in a Supersonic Turbulent Flow Using One and Two-Photon LIF," AIAA Paper 84-1536, AIAA 17th Plasma Dynamics Conference, June 1984.

36. Crosley, D.R. and G.P. Smith, "Rotational Energy Transfer and LIF Temperature Measurements," Combustion and Flame, Vol. 44, pp.27-34, 1982.

37. Zizak, G., Bradshaw, J.D. and J.D. Winefordner, "Thermal-Assisted Fluorescence: A New Technique for Local Flame Temperature Measurement," Applied Spectroscopy, Vol. 35, pp.59-66, January 1981.

38. Alden, M., Grafstrom, P., Lundberg, H. and Svanberg, S., "Spatially Resolved Temperature Measurements in a Flame Using Laser-Excited Two-Line Atomic Fluorescence and Diode-Array Detection," Optics Letters, Vol. 8, pp.241-243, May 1983.

39. Bradshaw, et. al., "Plasma Temperature Measurements by Laser-Induced Fluorescence," IEEE Journal of Quantum Electronics, Vol. 15, No. 9, pp.27D-28D.

40. Bradshaw, J.D., Omenetto, N., Zizak, G., Bower, J.N. and Winefordner, J.D., "Five Laser-Excited Fluorescence Methods for Measuring Spatial Flame Temperatures," Applied Optics, Vol. 19, pp.2709-2716, August 1980.

41. Moffatt, E.M., "Methods of Minimizing Errors in the Measurement of High Temperatures in Gases," Instruments, Vol. 22, No. 2, pp.122-132, February 1949.

42. Moffat, R.J., "Gas Temperature Measurement," Temperature - It's measurement and control in science and industry, Vol. III, Part 2, pp.553-571, Charles M. Herzfeld editor-in-chief, Reinhold Publishing Corporation, 1962.

43. Incropera, F.P. and D.P. DeWitt, Fundamentals of Heat Transfer, p.350, John Wiley & Sons, 1981.

44. Chedaille, J. and Y. Braud, Industrial Flames, edited by J.M. Beer and M.W. Thring, Vol. 1, pp.9-49, Crane, Russak & Company, 1972.

45. Cheng, J.K. and L.W. Casperson, Journal of Applied Physics, Vol. 56, p.1981, (1984).

46. Rockstroh, T.J. and J. Mazumder, Journal of Applied Physics, Vol. 61, p.917, (1987).